


DOTTORATO DI RICERCA IN RISCHIO E SOSTENIBILTA' NEI SISTEMI DELL'INGEGNERIA CIVILE, EDILE E AMBIENTALE
XVI Ciclo - Nuova Serie (2014-2017)
DIPARTIMENTO DI INGEGNERIA CIVILE, UNIVERSITÀ DEGLI STUDI DI SALERNO

PROPAGATION ANALYSIS OF FLOW LIKE-MASS MOVEMENTS TO EVALUATE THE EFFECTIVENESS OF PASSIVE CONTROL WORKS

Analisi della propagazione dei movimenti di massa tipo flusso per valutare l'efficacia degli interventi di tipo passivo

ING. ILARIA RENDINA

Supervisor:
PROF. ING. LEONARDO CASCINI

Coordinator
PROF. ING. FERNANDO FRATERNALI

Co-supervisors:
PROF. ING. SABATINO CUOMO
PROF. ING. MANUEL PASTOR
PROF. ING. GIACOMO VICCIONE

A.A. 2017/2018

In copertina: The Rainbow Mountain Vinicunca, Peru

PROPAGATION ANALYSIS OF FLOW LIKE-MASS MOVEMENTS TO EVALUATE THE EFFECTIVENESS OF PASSIVE CONTROL WORKS

Copyright © 2005 Università degli Studi di Salerno – via Ponte don Melillo, 1 – 84084 Fisciano (SA), Italy – web: www.unisa.it

Proprietà letteraria, tutti i diritti riservati. La struttura ed il contenuto del presente volume non possono essere riprodotti, neppure parzialmente, salvo espressa autorizzazione. Non ne è altresì consentita la memorizzazione su qualsiasi supporto (magnetico, magnetico-ottico, ottico, cartaceo, etc.).

Benché l'autore abbia curato con la massima attenzione la preparazione del presente volume, Egli declina ogni responsabilità per possibili errori ed omissioni, nonché per eventuali danni dall'uso delle informazione ivi contenute.

Finito di stampare il 01/03/2018

To my mother

INDEX

FIGURE INDEX

TABLE INDEX

ABSTRACT

Flow-like mass movements are catastrophic events occurring all over the world and may result in a great number of casualties and widespread damages. The analysis of the time-space evolution of the kinematic quantities is a useful tool to understand the propagation stage of these phenomena as well as for control works design.
The thesis deals with study of flow regime of Newtonian and non-Newtonian fluids and provides a contribution to this topic through the use of numerical procedures based on FV (finite volume) scheme and SPH (smoothed particle hydrodynamics) method. The FV model, developed by Rendina et al., 2017, is a single phase equivalent model, while the Geoflow-SPH, developed by Pastor et al.2009, considers the propagating mass with an average behavior of solid skeleton and pore water pressure.
The flow kinematics are analyzed through the Froude number, widely used in hydraulic engineering, discriminates two different kinematical features i.e. subcritical (slow) or supercritical (rapid) flows. The analysis concern a 1D/2D dam break of Newtonian (water flow) and non-Newtonian flows (in particular based on a viscoplastic and frictional laws).
The numerical results highlighted flows are supercritical even in areas far from trigger zones and Froude numbers of viscoplastic flows are higher than frictional flows.
Later, the Froude number is used as a quantitative descriptor of the control works response and, more generally, as an useful tool to estimate the efficiency of existing storage basins. The first case study regards Cancia, in the Dolomite Alps, where two storage basins dramatically failed on 2009 due to a short-time sequence of rainfall-induced debris flows and flash floods. The kinematic analysis highlighted that debris flow can be associated to a subcritical flow while flash flood is similar to a supercritical flow and for latter lower is the potential efficacy of control works.
The second case study regards Sarno, in the Campania region, where one of the most complex systems of passive control works was built after the 1998 events. The performance of the protection system is analyzed

referring to Froude number again which highlighted the importance of planning the emergency/ordinary maintenance of control works.
Finally, a new type of passive control work is described, i.e. the permeable rack that has the function of decrease the pore water pressures at the base and inside the propagating mass, thus causing the landslide body to brake and stop. The rack performance is tested as adaptation structure in existing protection systems also.

ACKNOWLEDGENTS

I would like to express my sincere gratitude to my supervisors, Leonardo Cascini, Sabatino Cuomo, Giacomo Viccione and Manuel Pastor for the guidance, encouragement and advice they have provided throughout my PhD studies and related research. It was a real privilege and an honour for me to share of their exceptional scientific knowledge but also of their extraordinary human qualities. I would like to thank you for allowing me to achieve this work.

Thanks to each member of Geotechnical Engineering Laboratory of Technical University of Madrid and a special thanks to Angel for our great friendship.

Thanks to each member of Geotechnical Engineering Laboratory of University of Salerno; I have been happy to share delights and worries with a friendly and cheerful group composed by Maria Rosaria, Maria Grazia, Mariagiovanna, Antonella, Antonio, Gaetano, Pooyan, Gianfranco and Luca.

A heartfelt thanks to Vittoria, I am extremely lucky to have a friend like her.

I must express my very profound gratitude to my parents for providing me with unfailing support and continuous encouragement throughout my years of study and throughout the process of researching and writing this thesis.

Last but not the least, I want to express my special thanks to Filippo, my better half, this accomplishment would not have been possible without you. Thank you.

ABOUT THE AUTHOR

Ilaria Rendina graduates in Environmental Engineering at the University of Salerno with 110/110 cum laude. During the PhD course she developed research topics about the propagation modeling of the flow-like mass movements with reference to the interaction of the flows with passive control works. She developed a 1D and single phase numerical model with the cooperation of a Hydraulic professor of University of Salerno (UniSa). She deepened the Geoflow-SPH model at the Technical University of Madrid (UPM). She attended several research meetings and workshops about flow-like phenomena, among which the international LARAM School on landslide risk assessment and mitigation (September 2016). In 2017 she presented part of current scientific research works at the Annual Meeting of Italian Geotechnical Researchers. She is co-author of scientific papers published in international journals, international and national conference.

Ilaria Rendina si laurea in Ingegneria per l'Ambiente ed il Territorio presso l'Università di Salerno con voto 110/110 e lode. Durante il corso di Dottorato si dedica a tematiche di ricerca connesse alla modellazione della fase di propagazione di frane tipo flusso con riferimento all'interazione di tali flussi con interventi di tipo passivo. Ha sviluppato un modello numerico monodimensionale e monofase in collaborazione con un professore di Idraulica dell'Università di Salerno (UniSa). Ha approfondito in modello Geoflow-SPH presso il Politecnico di Madrid (UPM). Partecipa a diversi incontri di ricerca e workshops riguardanti fenomeni franosi tipo flusso, tra cui la scuola internazionale LARAM sulla valutazione e la mitigazione del rischio da frana (Settembre 2016). Nel 2017 ha presentato lavori scientifici all'Incontro Annuale dei Ricercatori di Geotecnica. E' co-autrice di articoli scientifici pubblicati su riviste internazionali e in atti di convegno internazionali.

1 INTRODUCTION

Flow-like mass movements cause numerous victims and huge amounts of economic damage around the world. The typical features of these flow-like landslides are strictly related to the mechanical and rheological properties of the involved materials. Depending on solid fraction in the water-solid flowing mixture it is possible distinguish "debris flow" with high solid fraction (47-77%), "hyperconcentrated flow"(20-47%) and "flash flood" (<20%).

These flows are usually characterized by different magnitude (e.g. volume), runout distance (up to tens of kilometres) and velocity (in the order of metres/second).
The prediction of both runout distances and velocity through numerical modelling of the propagation stage can notably reduce losses inferred by these phenomena, as it provides a means for working out the information for the identification and design of appropriate mitigation measures (Pastor et al., 2009).

The PhD thesis focuses on understanding the flows kinematic features during the propagation phase and evaluating the effectiveness of passive control works such as check dams, storage basins and "permeable" racks. This work provides a contribution on this topic through the Froude number (*Fr*) expressing the ratio of inertial and gravitational forces. The *Fr* discriminates two different kinematical features of flow i.e. subcritical or slow ($Fr < 1$) and supercritical or rapid flow ($Fr > 1$) and becomes a quantitative descriptor of the control works efficiency.

Particularly, Chapter 2 proposes a literature review with reference to the main classifications of flow-like mass movements, the main stages and approaches available for propagation modeling. Finally, the main rheological models associated with each type of flow like phenomena are introduced to describe the behavior of involved material during the propagation stage.

Chapter 3 concerns the description of different types of passive control works, the main characteristics and design criteria, paying specific attention to "permeable" racks.

Chapter 4 summarizes the literature about Froude number focusing on experimental, analytical and numerical models analyzing the regime of flow-like mass movements.

Chapter 5 describes a 1D single phase equivalent model proposed by Rendina et al., 2017, to estimate the regime of Newtonian and non-Newtonian fluids flowing in an open channel. In particular, the kinematic of viscoplastic fluids, such as hyperconcentrated flows or flash flood, is studied.

In Chapter 6 the SPH-FDM model (proposed by Pastor et al., 2015) is used to simulate well-documented flume tests performed in USA. The validated model is later used to estimate the regime of the non-Newtonian flows in an open channel. In particular, the kinematic of frictional flows, such as debris flows or granular flows, is studied.

Chapter 7 deals with the case study of Cancia (North Italy) where some storage basins dramatically failed on 2009 due to a short-time sequence of rainfall-induced debris flows and flash floods. This issue is tackled using SPH model and implementing the Froude number to estimate the kinematical characteristics of different flows and the efficiency of control works.

Chapter 8 deals with a second case study in Sarno town (South Italy) where, after the catastrophic events of '98, some passive control works were built. Considering that no event occurred after the control works construction, the magnitude of future events was estimated on the basis of the available data. The numerical analysis are performed through SPH model implementing the Froude number to analyze the kinematic characteristics of the flows that interact with the control works.

In Chapter 9 the SPH-FDM model is used to simulate well-documented flume tests performed in Japan, equipped with a basal rack located at the end of the channel.

Once tested the reliability of the SPH-FDM model to describe the behavior of a debris flow on a permeable bottom boundary, the same model was used to simulate the potential upgrading of existing passive control works in the mountain basin described in Chapter 8 through the "permeable" rack.

Finally, Chapter 10 provides a general discussion and concluding remarks based on the results obtained for each section.

2 FLOW-LIKE MASS MOVEMENTS

Landslides are widespread catastrophic events around the world posing high risk to life and properties. Among natural disasters causing human life losses in the world, the floods and landslides are ranked as fourth and sixth place respectively, after earthquake, tsunami and extreme temperature (Fig. 2.1). Regarding to estimated economic losses caused by landslides and floods, a total of US $ 21.3 billion damages were reported in 29 countries out of 82 onc having experienced such disasters in 2015 (EM-DAT, 2016).

The events number, victims and economic damages are different in each continent, as testified by the global statistics on major events that have occurred in 2015 (Fig. 2.2). In terms of events number, Asia had the greatest percentage (45.1%), followed by the America, Africa, Europe and Oceania. The maximum number of deaths was recorded in Asia (86.9%), whereas this percentage was very low in the case of four other continents. Finally, in 2015 the reported damages were mainly widespread in three continents: Asia, America and Europe.

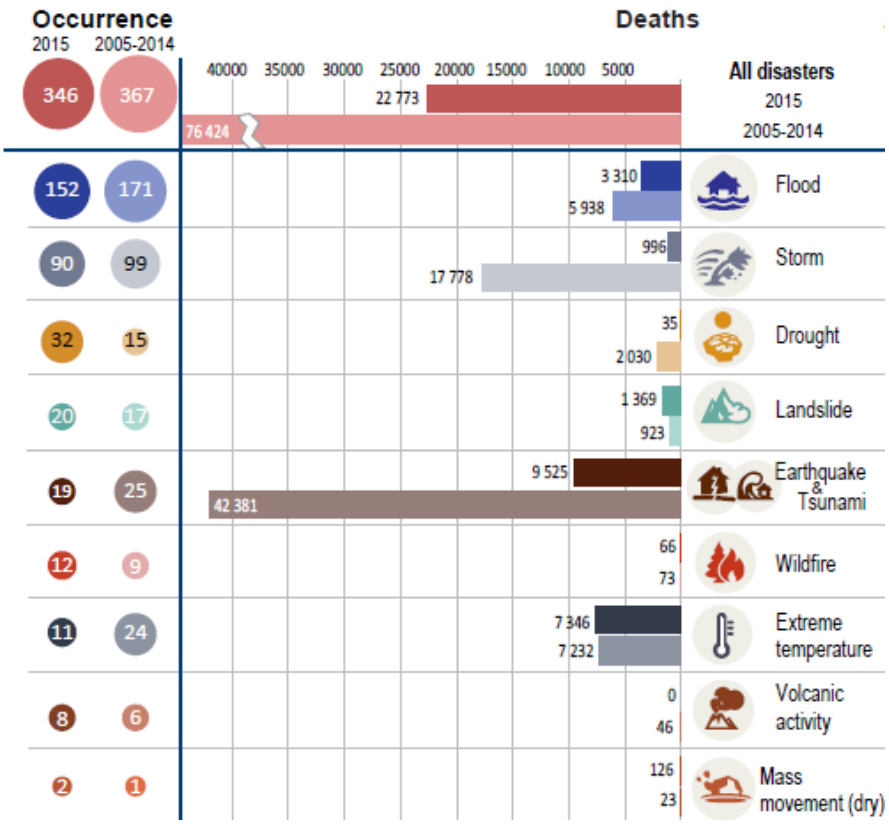

Figure 2.1 Human life losses for different type of disaster (2015 versus average 2005-2014) (source EM-DAT www.emdat.be).

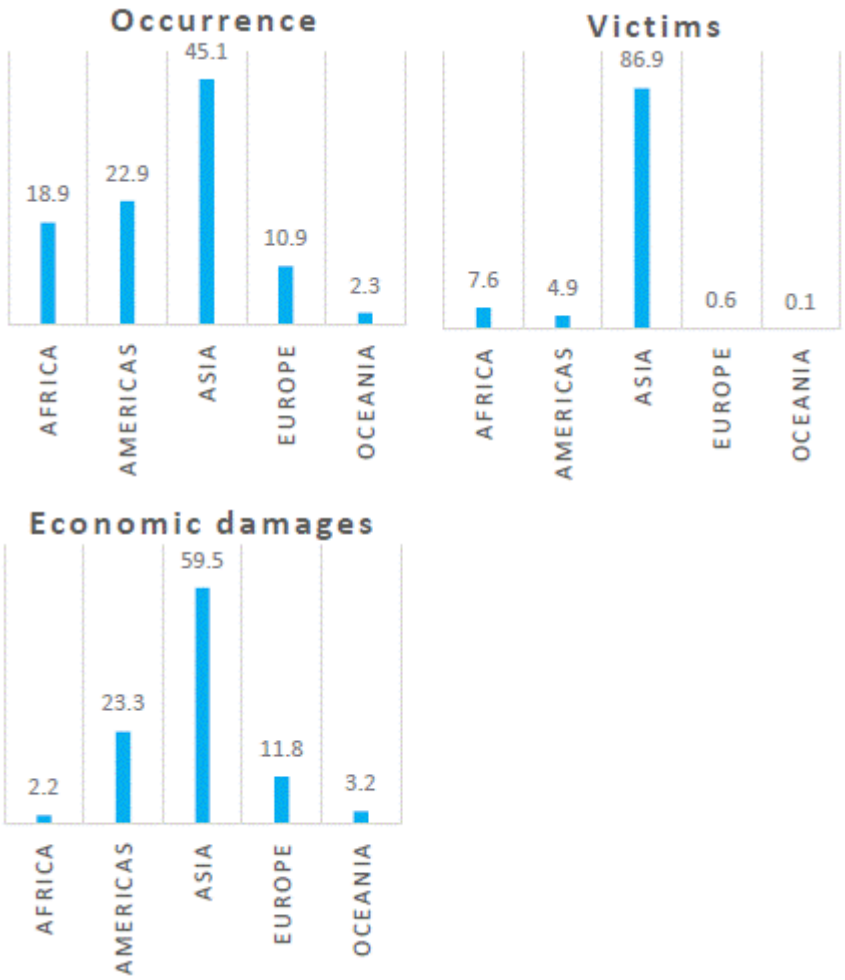

Figure 2.2 Percentage of reported events, victims and economic damages in different continents for landslides and floods events in 2015 (source EM-DAT www.emdat.be).

Of particular interest are flow-like mass movements systematically producing huge amounts of damage and numerous victims because of their high velocities and large run-out distances. Such phenomena involve different type of soil and, among these, pyroclastic soils originated in Campania region (Southern Italy) from the explosive phases

of the Somma Vesuvius volcano (Cascini et al., 2003) or granular materials in the Italian Dolomite Alps (Northern Italy).

In the following, the main features of flow-like mass movements are analyzed with referencing to to: i) classifications proposed by literature, ii) different stages, iii) rheological characteristics and approaches for proper modeling.

2.1 CLASSIFICATION

The flow type mass-movements are composed of mixtures of air, steam, water and solid fractions of various nature: such as fractured rocks, sands, silts including loess and volcanic ashes, sensitive and stiff fissured clays and organic soils (Hungr et al., 2001).

In order to frame the fundamental characteristics of flow-like movements, in the following the main scientific classifications are described.

The Varnes (1978) classification distinguishes different types of landslides on the basis of the movement typology and involved material (Fig. 2.3). As regards the involved material, Varnes (1978) separates rock and soil; the latter is divided into earth and debris: earth describes material in which 80% or more of the particles are smaller than 2 mm; debris contains a significant proportion of coarse material that is from 20% to 80 % of the particles are larger than 2 mm and the remainder are less than 2 mm. With reference to the typology of movement, the author distinguishes between falls, topples, slides, spread and flows. In particular for the flows the instability does not occur as a movement on one or more sliding surfaces, but rather as a viscous fluid in which the involved material are not able to resist the tangential stress variation produced by distortional deformations.

TYPE OF MOVEMENT		TYPE OF MATERIAL		
		BEDROCK	ENGINEERING SOILS	
			Predominantly coarse	Predominantly fine
FALLS		Rock fall	Debris fall	Earth fall
TOPPLES		Rock topple	Debris topple	Earth topple
SLIDES	*ROTATIONAL*	Rock slide	Debris slide	Earth slide
	TRASLATIONAL			
LATERAL SPREAD		Rock spread	Debris spread	Earth spread
FLOWS		Rock flow	Debris flow	Earth flow
		(deep creep)	(soil creep)	
COMPLEX		Combination of two or more principal types of movement		

Figure 2.3 Slope movement type and processes (Varnes, 1978).

The Cruden and Varnes (1996) classification considers the velocity reached by the landslide during the propagation stage (Fig. 2.4). The flow-like mass movements are included in the classes 5, 6 and 7 in Figure 2.4.

Landslide velocity class	Description	Velocity
7	Extremely rapid	>5m/s
6	Very rapid	3m/min - 5m/s
5	Rapid	1.8m/h - 3m/min
4	Moderate	13m/month- 1.8m/h
3	Slow	1.6m/year - 13m/month
2	Very slow	16mm/year - 1.6m/year
1	Extremely slow	<16mm/year

Figure 2.4 Landslide velocity scale (Cruden and Varnes, 1996).

The Hutchinson (1988) classification focuses on flow-like phenomena identifying: mudslides (non periglacial), periglacial mudslides (gelifluction of clays), flowslides, debris flows and sturzstroms. These phenomena differ in terms of mechanisms: In the mudslides phenomena, the shear failure process prevails over flow process; in flow slides and debris flow phenomena the two processes coexist whereas in sturzstroms just the flow processes exclusively occur (Fig. 2.5). Furthermore, among flow-like phenomena, Hutchinson (1988) distinguishes the mass transport

phenomena and mass movement phenomena. This distinction is based on the water content value, the unit weight of the mixture and sediment concentration (Fig. 2.6). In 2003, Hutchinson proposed a review of flow-like mass movements and identified two main groups: flow-type landslides in granular materials (debris flows, flow slide and rock avalanche) and flow-type landslides in fine-grained material or cohesive material (mudslides).

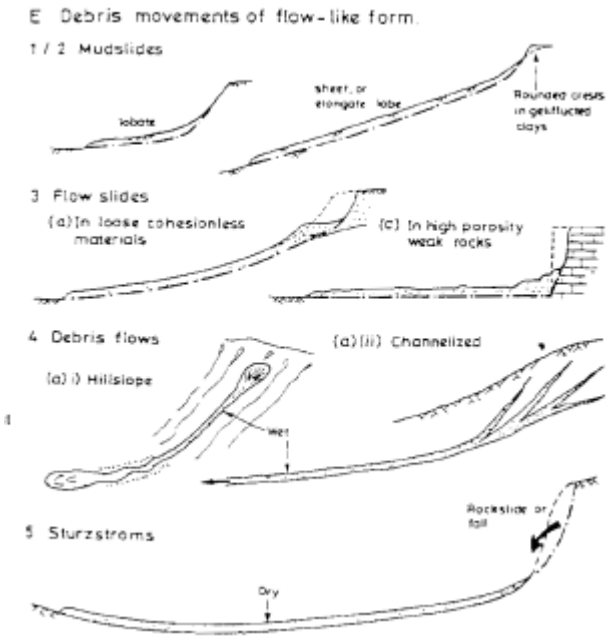

Figure 2.5 Main type of flow-like phenomena (Hutchinson, 1988).

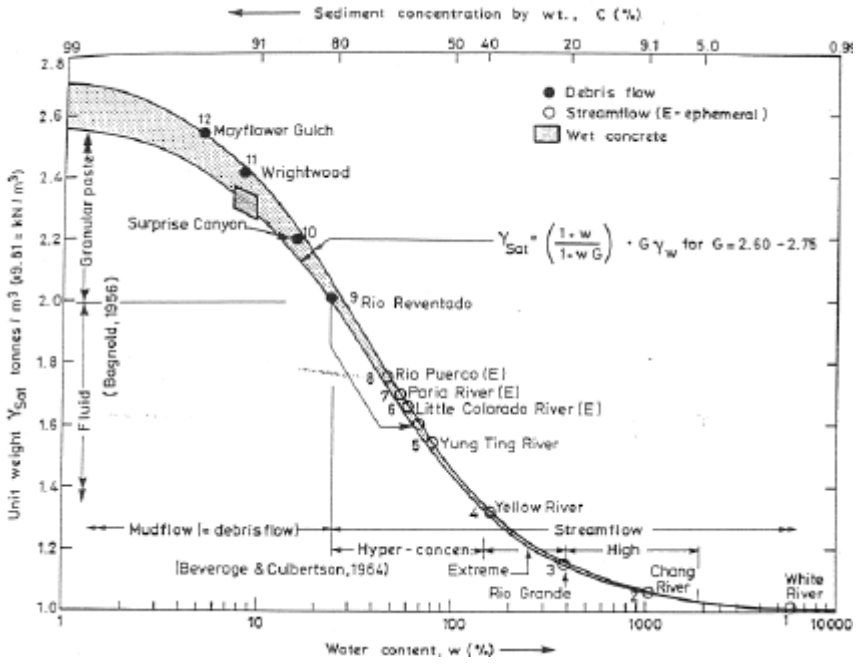

Figure 2.6 Continuous spectrum of sediment concentration. (Hutchinson, 1988).

Costa (1988) classification distinguishes three types of flow: Water Flood (WF), Hyperconcentrated Flow (HF) and Debris Flow (DF) as function of sediment concentration, bulk density, shear strength and flow type (Fig. 2.7).

Flow	Sediment concentration	Bulk Density [g/cm³]	Shear Strength [dyne/cm²]	Fluid Type
Water flood	1– 40 % by wt. 0.4 –20 % by vol.	1.01 – 1.33	0 - 100	Newtonian
Hyperconcentrated flow	40 – 70 % by wt. 20 – 47 % by vol.	1.33 – 1.80	100 - 400	Non-Newtonian (?)
Debris flow	70 – 90 % by wt. 47 – 77 % by vol.	1.80 – 2.30	>400	Viscoplastic (?)

Figure 2.7 General Rheologic Classification of Water and Sediment Flows in Channels (Costa, 1988).

Coussot and Meunier (1996) propose a classification of flow-like phenomena as a function of solid fraction and material type (Fig. 2.8). Furthermore the authors distinguish the one-phase flow or two-phase flow, respectively if the relative velocity of water and solid is small so that it can be considered as a viscous fluid or if the mean velocity of the coarsest solid particles, which are on the bed (bed-load), significantly differ from that of the water-solid suspension which flows around it.

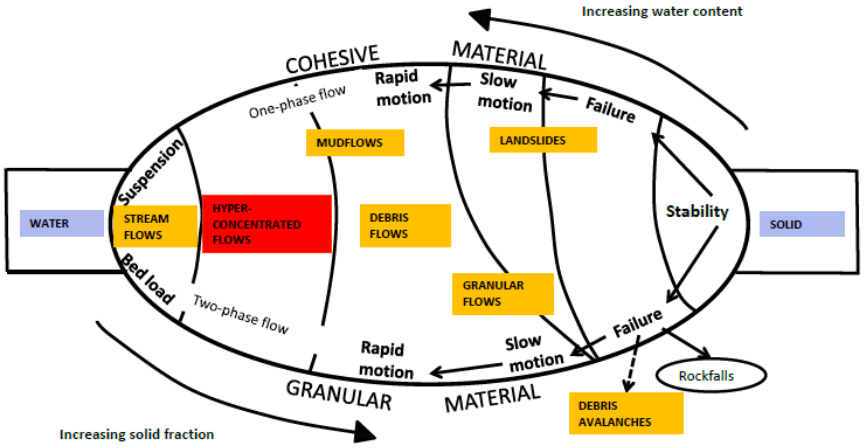

Figure 2.8 Classification of flow-like phenomena as a function of solid fraction and material type (Coussot and Meunier, 1996).

Hungr et al. (2001 and 2012) proposed a complete classification on the basis of: material type; water content; presence of excess pore-pressure or liquefaction potential at the source of the landslide, presence of a defined recurrent path (channel) and deposition area (fan); velocity and peak discharge of the event (Fig. 2.9).

Material	Water Content[1]	Special Condition	Velocity	Name
Silt, Sand, Gravel, Debris (talus)	dry, moist or saturated	- no excess pore pressure - limited volume	various	Non-liquified sand (silt, gravel, debris) flow
Silt, Sand, Debris, Weak rock[2]	saturated at rupture surface content	- liquefied material[3] - constant water	Ex. Rapid	Sand (silt, debris, rock) flow slide
Sensitive clay	at or above liquid limit	- liquefaction in situ[3] - constant water content[4]	Ex. Rapid	Clay flow slide
Peat	saturated	- excess pore-pressure	Slow to very rapid	Peat flow
Clay or Earth	near plastic limit	- slow movement - plug flow (sliding)	<Rapid	Earth flow
Debris	saturated	- established channel[5] - increased water content[4]	Ex. Rapid	Debris flow
Mud	at or above liquid limit	- fine grained debris flow	>Very Rapid	Mud flow
Debris	free water present	- flood[6]	Ex. Rapid	Debris flood
Debris	partly or fully saturated	- no established channel[5] - relatively shallow, steep source	Ex. Rapid	Debris avalanche
Fragmented Rock	Various, mainly dry	- intact rock at source - large volume[7]	Ex. Rapid	Rock avalanche

[1] Water content of material in the vicinity of the rupture surface of failure.

[2] Highly porous, weak rock (example weak Chalk, weathered tuff, pumice).

[3] The presence of full or partial in situ liquefaction of the source material of the flow slide may be observed.

[4] Relative to in situ source material

[5] Presence or absence of a defined channel over a large part of path, and an established deposition landform (fan). Debris flow is a recurrent phenomenon within its path, while debris avalanche is not.

[6] Peak discharge of the same order as that of major flood or an accidental flood. Significant tractive forces of free flowing water. Presence of floating debris.

[7] Volume greater 10,000 m^3 approximately. Mass flow, contrastino with fragmental rock fall.

Figure 2.9 Classification of flow-like phenomena (Hungr et al., 2001).

2.2 STAGES

In flow-like phenomena it is possible to recognize three main stages: the triggering, the propagation and the deposition stages (Hungr et al., 2001). Flow-like mass movements induced by rainfall have different features whether originated by infiltration or runoff along slopes. The first process occurs in the flows where the water prevails in the water-solid flowing mixture that, depending on solid percentage, affects "hyperconcentrated flows" (HF) (Coussout and Meunier 1996), "water floods" (WF) (Costa, 1988) and also "flash floods" (FF) (Gaume et al., 2009). This triggering mechanism involves different stages: detachment of soil particles, transportation of sediment due to soil erosion induced by intense rainfall and deposition when the transport capacity of the flow is reduced below that required for the existing suspended load (Kavvas and Govindaraju, 1992).

The "debris flows" (DF) are originated from a variety of triggering mechanisms and they are mainly related to the reduction of soil shear strength caused by the increase in the pore water pressure as a result of several factors like (Cascini et al., 2005): surface runoff processes (Van Dine, 1985; Takahashi, 1991, van Ash et al., 2009; Berti et al., 1999); increase of the water table (Leroueil, 2004; Dietrich and Montgomery, 1998); groundwater supplies provided by artesian conditions or hidden springs (Mathewson et al., 1990; Onda et al., 2004; Lacerda, 2004); groundwater flow patterns caused by the stratigraphic setting and/or anthropogenic structures and roads (Wolle and Hachich, 1989; Ng and Shi, 1998; Crosta et al., 2003); increase of saturation degree in unsaturated soils (Futai et al., 2004); variations of hydraulic boundary conditions due to the formation of deep rills as a result of erosion processes related to intense rainfall (Deere and Patton, 1972); undrained loading as a result of first time slides triggered by rainfall, that impact on in-place soils (Hutchinson and Bhandari,1971) and soil liquefaction phenomena (Sassa, 1985; Hungr et al., 2001).

The propagation stage includes the movement of the unstable masses from the source area toward the deposition. During this phase it is possible to observe erosion processes in HF, WF and FF; while fluidization phenomena along the path in DF. The erosion can be extremely important since the result of this process is an increase of the

landslide volume (Costa and Williams, 1984; Jibson, 1989; Sassa et al., 1997; Wieczorek et al., 2000; Cascini, 2004). On the other hand, the fluidization can occur along the sliding surface or within the sliding zone during the rise in pore-water pressure and affects both the run-out distances and the kinematic characteristics of the propagating masses (Iverson and LaHusen, 1989; Iverson and Denlinger, 2001; Iverson et al., 2010; Iverson et al., 2011; Cascini et al., 2016).

The four types of flows (DF, HF, WF, FF) are usually characterized by different magnitude (e.g. volume), runout distance and maximum velocity at piedmont areas where urban centres are usually settled. The high discharge of debris flows, up to 40 times greater than those of extreme floods, (Hungr et al., 2001) is responsible for greater flow depth (up to 20 m), higher velocity (up to 30 m/s) and higher impact loads respect to hyperconcentrated flows.

When the flows reach the apex of the depositional fan, it is possible to recognize different deposit structures: in the HF, WF and FF the coarsest solid fraction generally deposits first whereas the fine suspension flows away as wash load before being deposited during flow; in the DF the concentration of big boulders is higher close to the surge front (Coussot and Meunier, 1996).

2.3 APPROACHES FOR MODELING

The features of flow-like mass movements provide serious difficulties towards their complete modelling and several models are used to interpret separately the different stages.

Focusing on the propagation stage, it is usually deepened through empirical and analytical methods, small or large-scale laboratory tests and finally through numerical methods.

Empirical methods (e.g. Corominas, 1996) are usually based on extensive amounts of field observations and on the analysis of the relationships between the run-out distance and different landslide mechanisms, their morphometric parameters, the volume of the landslide mass and the physical and mechanicals characteristics of soils (Quan Luna, 2012). These methods are based on very simplified conditions and it is possible to use them only for conditions similar to those on which their development is based.

Analytical methods (e.g. Takahashi, 1991) include different formulations based on lumped mass approaches in which the mass is assumed as a single point (Quan Luna, 2012). These methods have an obvious limitations in being unable to account for internal deformation and the motion of the flow front; but they may provide reasonable approximations to the movement of the center of gravity of the landslide (Evans et al., 1994).

Small or large scale laboratory tests (e.g. Iverson et al., 2010) are used to measure the kinematic characteristics of the flows in order to understand the flow- like mass movements behavior. These tests provide a dataset in order to test the numerical models used to interpret and predict landslides.

Numerical methods (e.g. Pastor et al., 2009) have been developed either for distinct element or for continuum based models. Continuum fluid mechanics models, the most common approach, are based on the mass, momentum and energy conservation equations that describe the dynamic motion of flow and a rheological model to describe the landslide behavior (Quan Luna, 2012).

The numerical methods can be classified in three groups: model based on the solution dimension in 1D or 2D; models based on the solution reference frame and models based on the basal rheology.

Models based on the solution dimension in 1D or 2D: 1D models analyze the movement considering the topography as a cross-section of a single predefined width while 2D models make the analysis considering the topography in plan and cross-section (De Chiara, 2014);

Models based on the solution reference frame: the equation of motion can be formulated in two difference frames of reference: Eulerian or Lagrangian. An Eulerian reference frame is fixed in space, analogous to an observer standing still as a landslide passes, and require the solution of a governing equation using a dense, fixed computational grid. A Lagrangian reference frame moves with the local velocity, analogous to an observer riding on top of landslide (De Chiara, 2014);

Models based on the basal rheology: the rheology is defined as the study of the flow behavior (Irgens, 2014) and is expressed as resistance forces (τ_b) that interacts at the interface between the flow and the bed path (Quan Luna, 2012). The most common rheological models used to describe landslides behavior are: "Newtonian resistance", "frictional or Coulomb resistance", "frictional-turbulent or Voellmy resistance", "visco-plastic or Bingham or Herschel-Bulkey resistance" and "Quadratic resistance" (Luna, 2012) (Table 2.1). The flow resistance term may be broadly separated into: one-phase models which describe the flow resistance behavior of either the slurry of water and fine material or the entire fluid-solid mixture and two-phase models which consider both a fluid phase and a solid phase (Naef et al., 2006). An overview of several numerical models as a function of rheology, solution approach and reference frame is represented in Table 2.2.

Table 2.1 Most common rheological models used to describe landslides behavior (modified from Quan Luna, 2012).

Reology	Description	Flow resistance term (τ_b)
Chezy-Manning (Newtonian-turbulent)	Resistance that is a function of flow depth, velocity and turbulent coefficient (Manning coefficient) (m) (Pastor et al., 2009).	$\tau_b = \frac{\rho g m'^2 u^2}{h^{\frac{7}{3}}}$ (2.1) With: ρ the flow density; g the gravitational acceleration; m' the Manning coefficient that takes into account the turbulent and dispersive components of flow; u the flow velocity and h the flow height.
Frictional (Coulomb)	Resistance based on the relation of the effective bed and normal stress at the base and the pore fluide pressure (Pastor et al., 2009)	$\tau_b = ((1-n)(\rho_s - \rho_w) g\, h - p_w^b) tg\phi_b$ and $tg\phi_b = (1 - r_u) tg\phi$ and $\tau_b = ((1-n)(\rho_s - \rho_w) g\, h - p_w^b) tg\phi_b$ (2.2) With: ϕ_b the basal friction angle; ϕ the dynamic frictional angle and r_u the pore-pressure ratio.
Voellmy	Resistance that features a velocity squared resistance term (turbulent coefficient ξ) similar to the square value of the Chezy resistance for turbulent water flow in open channels and a Coulomb-like friction (apparent friction coefficient ε). (Voellmy, 1955).	$\tau_b = \varepsilon + \frac{u^2}{\xi h}$ (2.3) With: ε equal to Frictional resistance (2.2); u the flow velocity; ξ is the turbulent coefficient and h the flow height.
Bingham	Resistance that is a function of flow depth, velocity, constant yield strength (τ_y) and dynamic viscosity (μ) (Coussot, 1997).	$\tau_b = \frac{1}{\rho g h}\left(\frac{3}{2}\tau_y + \frac{3\mu}{h} u\right)$ (2.4) With: ρ the flow density; g the gravitational acceleration; h flow height; τ_y the constant yield strength due to cohesion; μ dynamic viscosity and u flow velocity.

Quadratic	Resistance that incorporates a turbulent contribution to the yield and the viscous term already defined in the Bingham equation (O'Brien et al., 1993).	$\tau_b = \frac{\tau_y}{\rho g k} + \frac{K \mu}{8 \rho g k^2} u + \frac{m'^2 u^2}{k^{\frac{4}{3}}}$ (2.5) With: τ_y the constant yield strength due to cohesion; ρ the flow density; g the gravitational acceleration; h flow height; K the resistance parameter that equals for laminar flow in smooth, wide, rectangular channels, but increases with roughness and irregular cross sections; μ dynamic viscosity; u flow velocity and m' Manning coefficient.	

Table 2.2 Most common numerical models (Quan Luna, 2012).

Model	Rheology	Solution approach	Reference frame	Variation of rheology
MADFLOW (Chen and Lee, 2007)	Frictional, Voellmy and Bingham	Continuum Integrated	Lagrangian with mesh	No
TOCHNOG (Crosta et al., 2003)	Frictional (elastoplastic model)	Continuum Integrated	Differential (adaptive mesh)	Yes
RAMMS (Christen et al., 2010)	Voellmy	Continuum Integrated	Eulerian	Yes
DAN3D (Hungr and McDougall, 2009)	Frictional, Voellmy and Bingham	Continuum Integrated	Lagrangian	Yes
FLATMODEL (Medina et al., 2008)	Frictional and Voellmy	Continuum Integrated	Eulerian	No
SCIDDICA S3-hex (D'Ambrosio et al., 2003)	Energy based	Cellular Automata	Eulerian	No
3dDMM (Kwan and Sun, 2006)	Frictional and Voellmy	Continuum Integrated	Eulerian	Yes
SPH (Pastor et al., 2009)	Frictional, Voellmy and	Continuum Integrated	Lagrangian meshless	Yes

	Bingham			
MassMov2D (Begueria et al., 2009)	Voellmy and Bingham	Continuum Integrated	Eulerian	Yes
RASH 3D (Pirulli and Mangeney, 2008)	Frictional, Voellmy, Quadratic	Continuum Integrated	Eulerian	No
FLO-2D (O' Brien et al., 1993)	Quadratic	Continuum Integrated	Eulerian	No
TITAN2D (Pitman and Le, 2005)	Frictional	Continuum Integrated	Lagrangian with mesh	No
PFC (Poisel and Preh, 2007)	Inter-particle and particle wall interaction	Solution of motion of particles	Distinct element method	No
VolcFlow (Kelfoun and Druitt, 2005)	Frictional and Voellmy	Continuum Integrated	Eulerian	No

2.4 DISCUSSION

The proposed classifications in the literature introduce a framework for i) type of movement and type of material; ii) velocity class; iii) solid fraction and water content and iv) genesis mechanisms and evolution. However, different limits can be recognized in the classifications, mainly due to: i) different terminology used to identify the phenomenon; ii) difficulty to make distinction between different phenomena iii) not exhaustive description of triggering and evolution mechanisms.

An open issue for propagation modeling is the selection of suitable rheological model for each type of flow-like mass movements. The difficulties arise from variability of landslides composition (solid fraction and water content) that changes within the wave and along the flow

path. Another major difficulty is distinguishing between appropriate flow regimes, which may also change during the propagation phase.

In order to choose the most appropriate rheological model it is important to understand if the fine or coarser particles dominate the flow behavior. According to Coussot and Meunier Classification, the "mudflows" (MF) and "landslides or earthflows" (EF) belong to the first group; while "debris flows" (DF) and "granular flows" (GF) to the second group. For both groups, during the propagation stage, solid particles and water move at the same velocity as a single visco-plastic body (one-phase flow) in a laminar flow, undergoing large homogeneous deformations without significant changes to its mechanical properties (Coussot and Meunier, 1996). Therefore, these flows exhibit a behavior well described by a visco-plastic rheological models such as the Bingham model or the Herschel-Bulkley model (Eq. 2.4).

Actually, in the case of high velocities of the flow, the DF and GF may show turbulent behavior, suggesting that laminar flow resistance relations may be inappropriate; indeed for these flows the grain collisions dominate the flow behavior. So, they may be described by Newtonian resistance (Eq. 2.1), frictional or Coulomb resistance (Eq.2.2) and frictional-turbulent or Voellmy resistance (Eq. 2.3).

The HF may be generalized as a turbulent, solid–liquid two-phase flow, gravity-driven flows of water and sediment in which the mean velocity of the coarsest solid particles, which are pushed and rolled on the bed (bed-load), significantly differ from that of the water-solid suspension which flows around it (Coussot and Meunier, 1996).

The WF and FF with low concentration of sediment, high percentages of fine material and low strain rates follow a Newtonian behaviour (Costa, 1988); since the increament of the sediment concentrations (HF) the flow mechanism begins to change: viscosity and shear strength as well as increasing particle collisions so that the flows exhibit a behaviour could be well described by a viscous-plastic rheological models such as

the Bingham model (Eq. 2.4) or a collisional-viscous-plastic rheological model like the quadratic shear stress model (Eq. 2.5). In the Table 2.3 or Figure 2.10 the main rheologies associated with each type of flow like phenomena are shown; the proposed rheological models are used in all modeling of the flow-like mass movements analyzed in this PhD thesis.

Table 2.3 The proposed rheological models for each type of flow like mass-movements.

Type of flow like phenomena	Rheology	One-phase	Two-phase
FF	Newtonian	×	
WF	Newtonian	×	
HF	Newtonian Bingham Quadratic	×	×
MF	Bingham	×	
EF	Bingham	×	
DF	Newtonian Frictional Voellmy	×	×
GF	Newtonian Frictional Voellmy	×	×

MF: mudflows; EF: earthflows; FF: flash floods; WF: water flows; HF: hyper-concentrated flows; DF: debris flows and GF: granular flows.

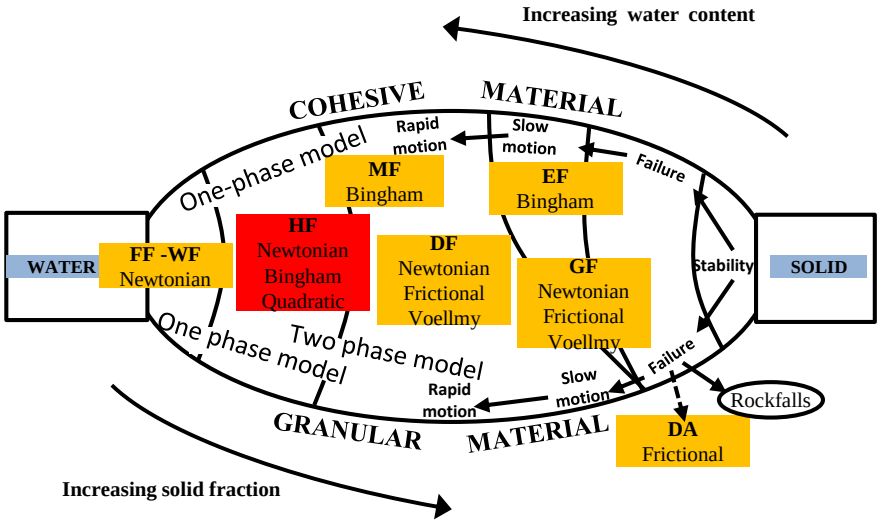

Figure 2.10 The proposed rheological models for each type of flow like mass-movements. MF: mudflows; EF: earthflows; FF: flash floods; WF: water flows; HF: hyper-concentrated flows; DF: debris flows; GF: granular flows and DA: debris avalanches.

3 PASSIVE CONTROL WORKS

Flow-like mass movements consequence can be reduced through landslide risk mitigation measures, which include non-structural and structural measures. Non-structural measures are based on early-warning and alarm systems or civil protection plans, both able to increase the awareness and the preparedness of the persons at risk. Structural measures include drainage, erosion protection, channelling, vegetation, ground improvement, barriers such as earth ramparts, walls, artificial elevated land, anchoring systems and retaining structures; buildings designed and/or placed in locations to withstand the impact forces of landslides and to provide safe dwellings for people, and escape routes (Vaciago, 2013). All these measures, Figure 3.1, can be broadly divided into two groups: active and passive control works. Their function is to avoid the landslide triggering or to stop/diverge the flows or to diminish their impact to the exposed structures.

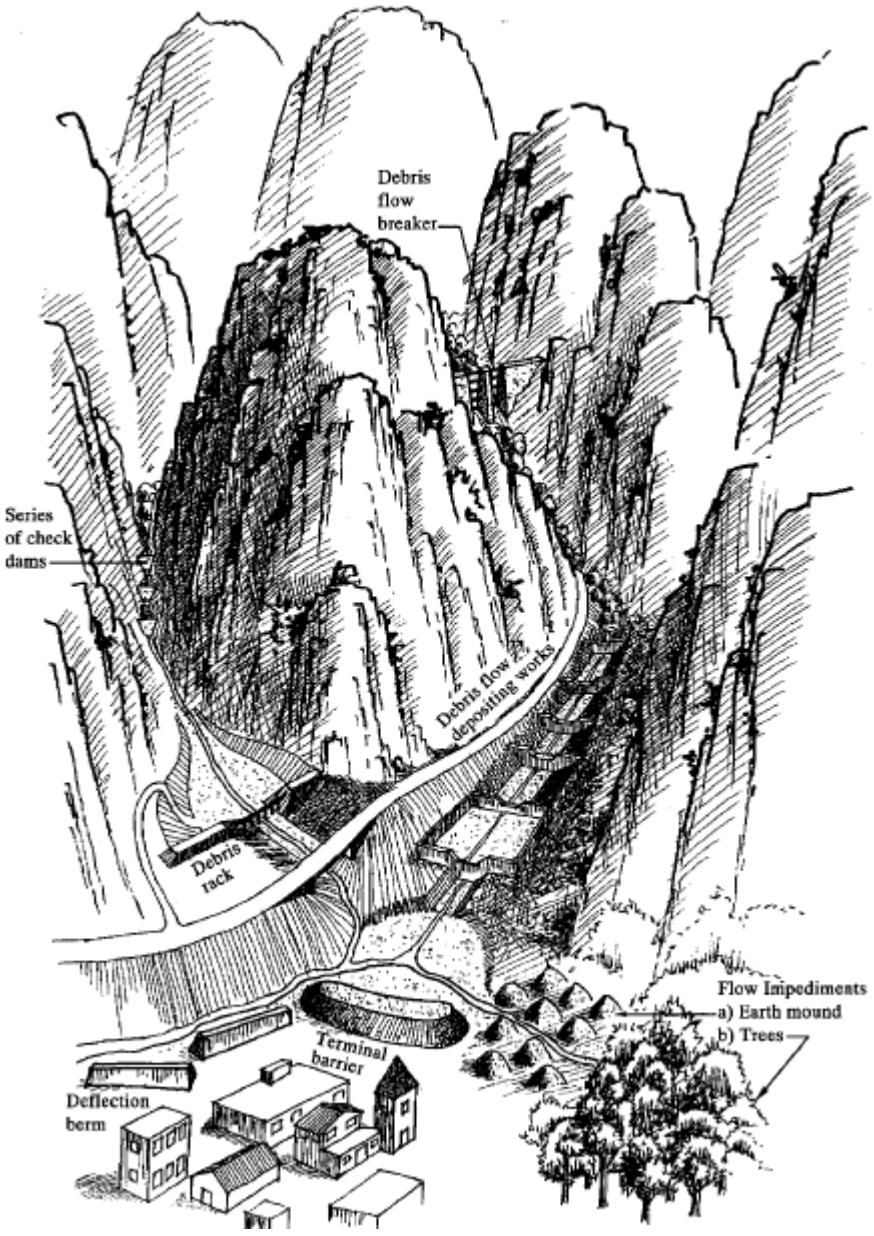

Figure 3.1 Schematic diagram showing some passive control works (Lo, 2000).

The selection of the most appropriate mitigation measures depends on several aspects: the physical characteristics of the geosystem, including the stratigraphy and the mechanical characteristics of the materials, the hydrological (surface water) and the hydrogeological (groundwater) regime; the morphology of the area; the actual or potential causative processes affecting the geosystem, which can determine the occurrence of movement or landslides; the presence and vulnerability of elements at risk, either in the potentially unstable area or in areas which may be affected by the run-out; the phase and rate of movement at the time of implementation; the morphology of the area in relation to accessibility and safety of workers and the public; environmental constraints, such as the impact on the archeological, hystorical and visual/landscape value of the locale; preexisting structures and infrastructure that may be affected, directly or indirectly and capital and operating cost, including maintenance (Vaciago, 2003).

In the following the attention is focused on typologies and design criteria of passive control works.

3.1 TYPE OF PASSIVE CONTROL WORKS

These control works can be divided into three basic types: open, closed and sediment control structures.

Open control works are designed to "constrain" the flow while closed control works are designed to "contain" the flow; finally, the sediment control structures to control the movement of fine-grained material across a debris fan or alluvial fan, thereby minimizing the amount of fine-grained sediment entering a neighbouring body of water (VanDine, 1996).

The open control works include: i) unconfined deposition areas, ii) impediments to flow (baffles), iii) check dams, iv) lateral walls (berms), v) deflection walls (berms) and vi) terminal walls, berms, or barriers.

The unconfined deposition area (Fig. 3.2 a) are designed to slow down and prepare the flow to the deposition phase through low slopes and extended cross-sections. This type of control works can be associated with impediment to flow or baffles to deflect the flow (Fig. 3.2 b). The check dams are usually built in series in the transportation/amplification zone of a flow like phenomenon or immediately upstream of a storage basin. In the first case are used to reduce the channel slope locally and the erosion process along the bottom and sides of the channel (Fig. 3.2 c); in the latter case, the dams are intended to be inlet control structures. The lateral walls and deflection walls are designed to constrain the lateral movement of flow and to protect buildings along the path of flow like phenomena (Fig. 3.2 d); while the terminal wall to encourage deposition by presenting obstruction to flow (Fig. 3.2 e).

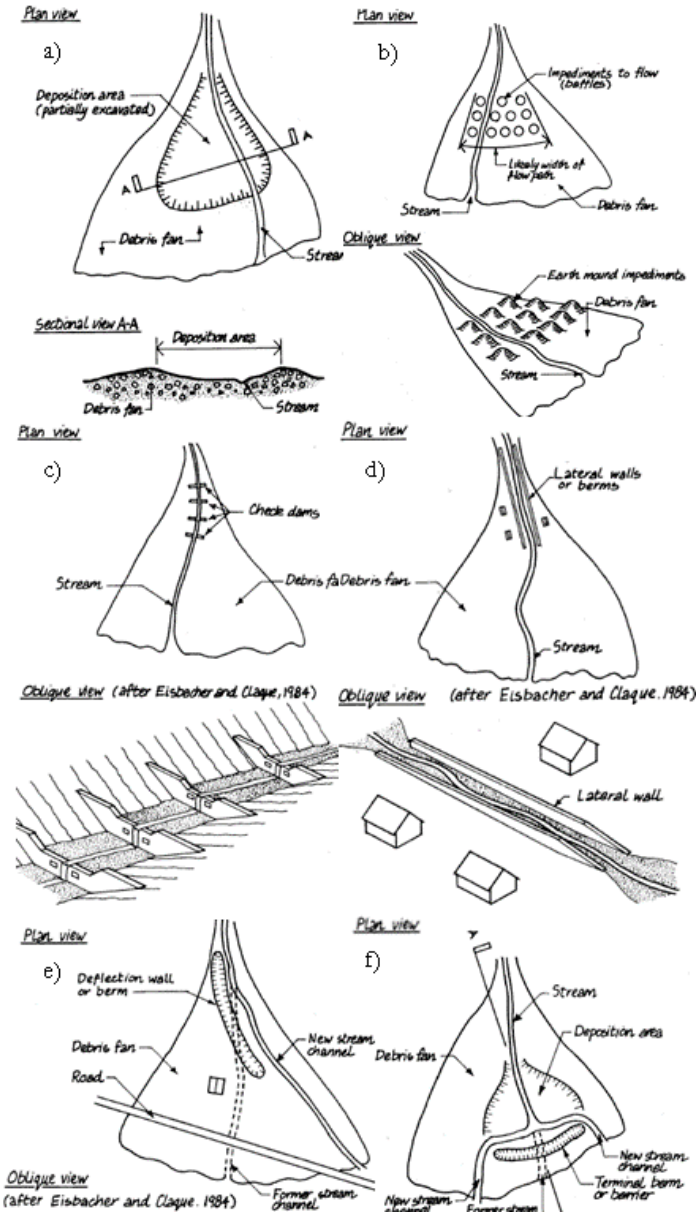

Figure 3.2 An overview of open control works: a) unconfined deposition areas; b) baffles; c) check dams; d) lateral walls; e) deflection walls and f) terminal wall (VanDine, 1996).

The closed control works include: debris racks, grizzlies, or some other form of debris-straining structure located in the channel; and debris barriers (or open dams) and storage basins (VanDine, 1996).

The debris racks and debris barriers are used to separate fine and coarser particles from water flows, (Figs. 3.3 a, b), while the storage basins are similar to terminal berm or barrier, in that both are located across the debris flow path and designed to encourage deposition (Fig. 3.3 b).

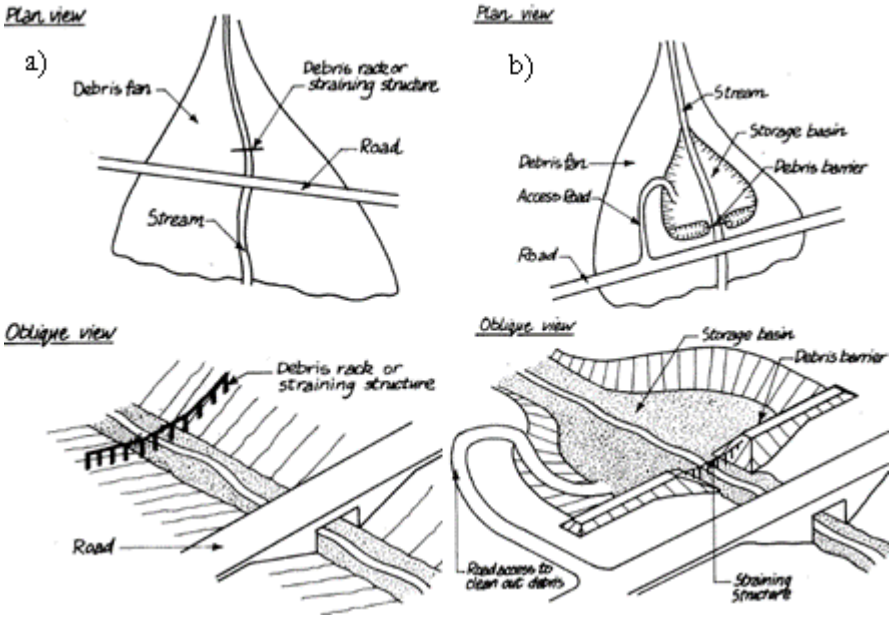

Figure 3.3 An overview of closed control works: a) debris racks and debris barriers (or open dams) and storage basins (VanDine, 1996).

The sediment control structures are designed to remove water from debris flow and thus to reduce flow energy. In the following, a particular sediment control work is described in detail considering that its use is analyzed in the following as a relevant measure to upgrade existing control works.

3.1.1 The permeable rack

The permeable rack or debris-flow brake is an old-new sediment control structure based on the dissipation of pore water pressures during the propagation of a debris flow. This control work can be located along the path of the landslide and is a unique sediment-control facility designed to reduce the run-out distance of debris flows. It consists of a "screen" which is a flat drain-like deck placed horizontally over the river channel (Fig. 3.4); when a debris flow crosses the drainage, the velocity of the debris flow decreases rapidly and then it stops (Cascini et al., 2016). The basic idea of this control work was proposed by Hashimoto and other Japanese scholars in the fifties (Kiyono et al., 1986). Debris-flow brakes were tested in three pilot projects in Japan to collect data and technical know-how regarding their construction and maintenance; then, a real-size experiment carried out in the Kamikamihori Valley, Mt. Yakedake, Nagano Prefecture, Japan (Gonda, 2009; ICHARM,2008). A permeable rack was installed in 1985 on a 4° slope parallel to the original stream channel slope. The board consisted of 25 prismatic steel pipes, each 20 m long with rectangular cross-sections of 0.2 × 0.2 m. The pipes were laid parallel to each other with 0.2-m spaces between them to drain off the watery slurry when subjected to debris flows (Fig. 3.5) (Suwa et al., 2009).

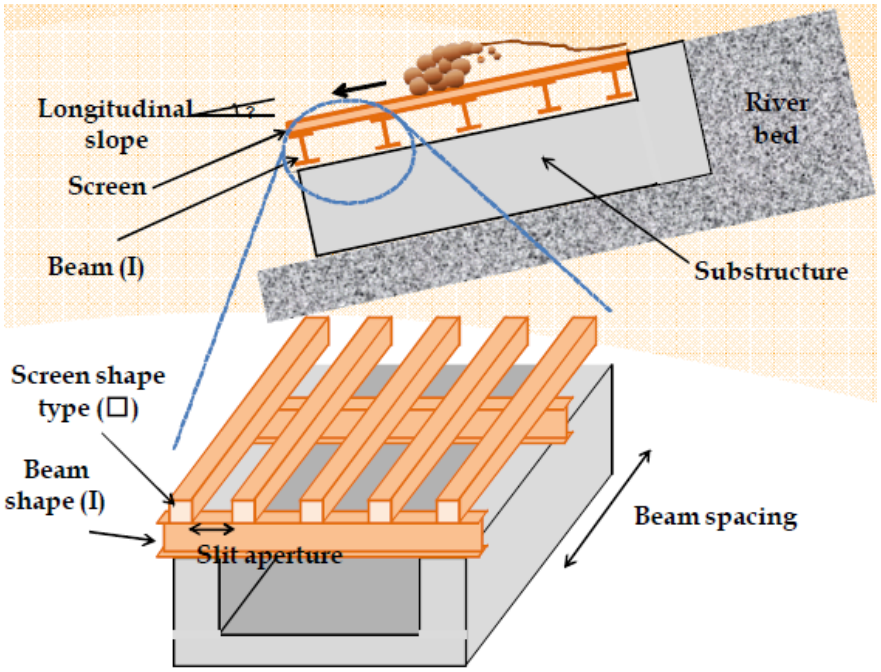

Figure 3.4 Structure of a permeable rack (ICHARM, 2008).

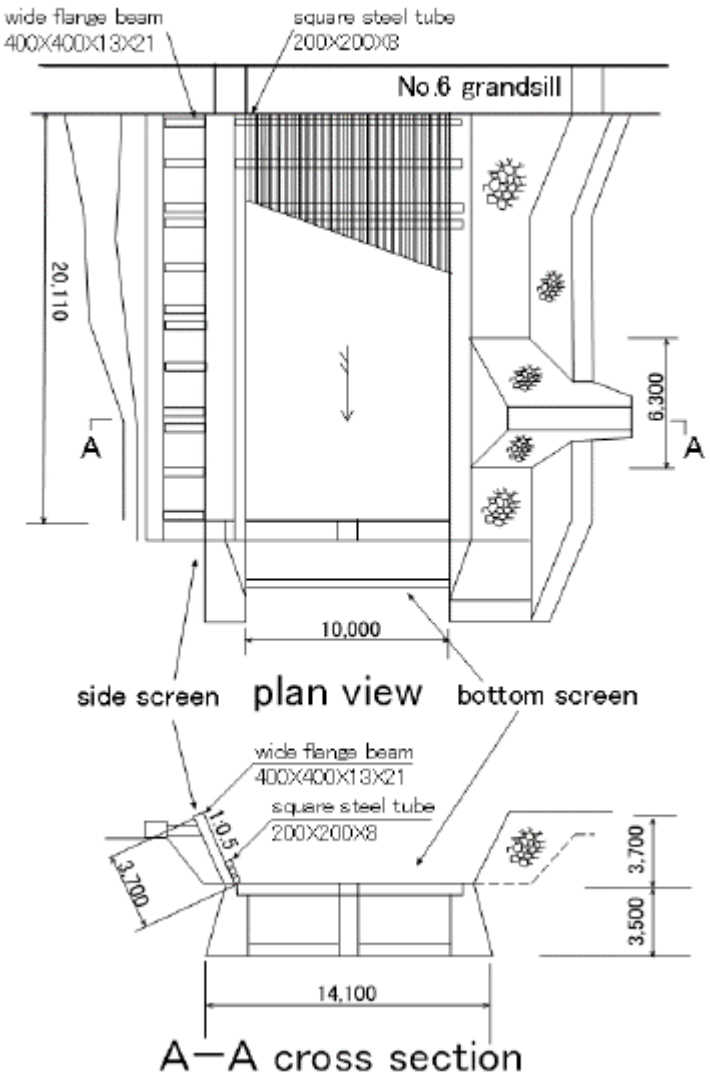

Figure 3.5 Structure of the rack in Kamikamihori Valley, Mt. Yakedake, Nagano Prefecture, Japana (Kiyono et al., 1986).

Six days after the completion of the rack construction (July 21, 1985), a debris flow event occurred. The Figure 3.6 shows the characteristics of the event while the Figure 3.7 shows two screenshots before and after

the occurrence of the event. Only 5% of the total volume of 5500 m^3 stopped, however the peak of the flow rate must have been effectively reduced and the flow converted to a less-harmful level because of the reduced size of the front grain (Suwa et al., 2009).

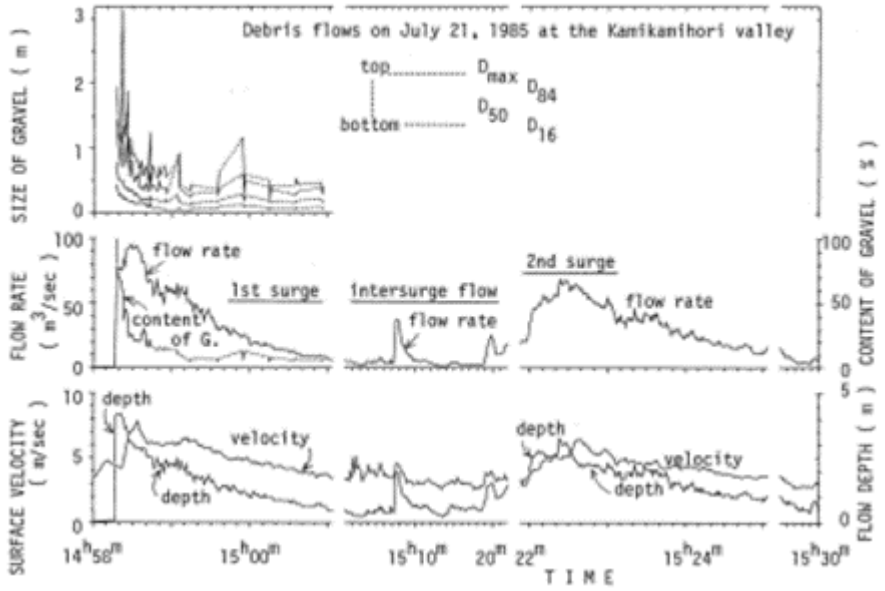

Figure 3.6 Hydrograph of the July 21, 1985 debris flow showing the gravel content and size parameters (Suwa et al., 2009).

Figure 3.7 Pictures of a permeable rack, before and after the occurrence of a debris flow in the Kamikamihori Valley, Mt. Yakedake, Nagano Prefecture, Japan (Cascini et al., 2016).

Since few years the efficacy and the efficiency of permeable racks have been experimentally tested by Gonda, 2009; Kim et al., 2012 a, b and Brunkal, 2015, through small channels with downstream racks.
Gonda, 2009 performed flume tests in a small channel equipped with a (permeable) rack; the experiments were performed varying the inclination of the channel, the material and the sizes of the openings of the rack. The experimental results showed the variation of the debris

flow run-out distance on the rack with changes in the size of openings of the rack under various material conditions. The run-out distance of the debris flow on the rack decreases as the size of the openings increases. When the size of the openings exceeds a certain value, the run-out remains constant independent of the opening size (Fig. 3.8). The threshold opening size increases with the diameter of the material. These tests will be largely described in Chapter 8, in which also numerical modeling has been performed.

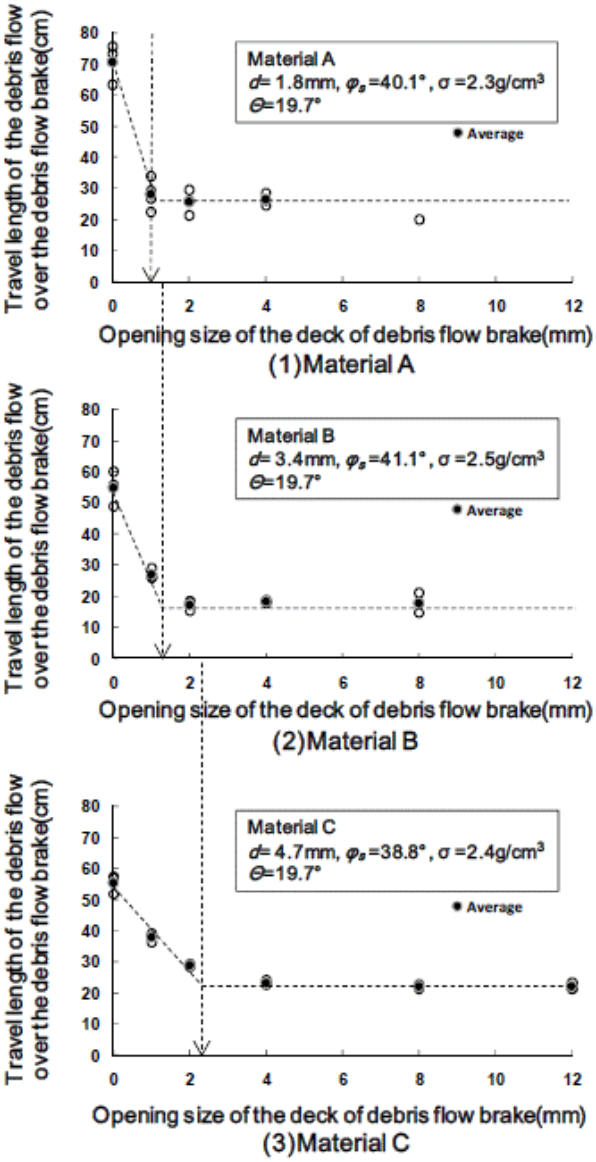

Figure 3.8 The debris flow run-out distance on the rack versus the size of openings of the rack under various material conditions (*d* is the median diameter size, σ is the density, φ_s is the friction angle) (Gonda, 2009).

Also Kim et al., 2012 observe that the variation of run-out distance depend on opening size of the rack and experimental results demonstrate a reduction from minimum 34% to maximum 65% (Fig. 3.9).

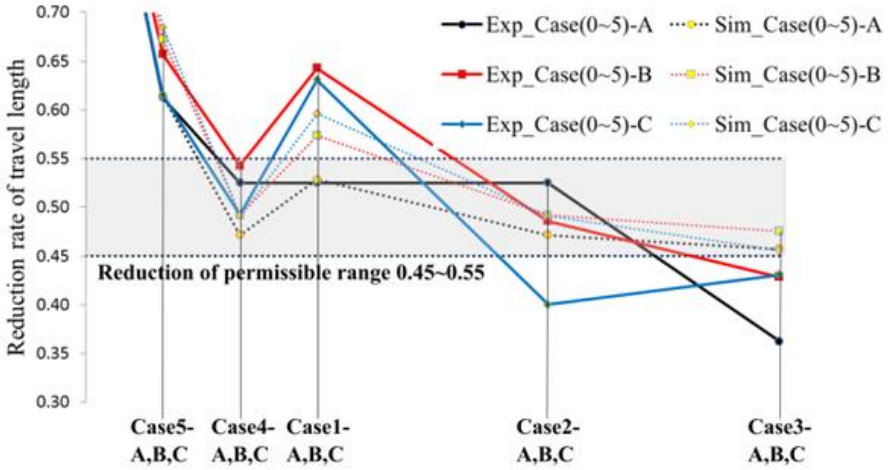

Figure 3.9 Reduction rate of run-out distance. The Cases (0-5) refer to different opening size of rack and A, B and C are the examined materials (Kim et al., 2012a).

Brunkal, 2015 carried out flume tests varying the rack geometry (lengths, opening size). The percentage of the debris flow arrested on and behind the rack ranged from 52% to 96% with an average value of 82% and placing two racks in series the percentage reached more than 90%. This result in essence contradicted the original research hypothesis that the debris flow brake would only stop the largest, most destructive particles of the debris flow. The well-graded character of the debris-flow material promotes the bridging across the gaps in the rack and therefore arrests a larger proportion of the overall mass (Fig. 3.10) (Brunkal, 2015).
Despite many studies have been developed on the debris flow brakes and they are cost-efficient, simply designed and easily repaired and maintained, this type of structure is rarely constructed because the residents tend to be distrustful of the structure's efficacy, preferring

instead wall-type concrete check dams because they appear stronger and more able to trap debris flow (ICHARM, 2008).

Figure 3.10 Photos of representative flume test results (Brunkal, 2015).

3.2 DESIGN CRITERIA

The design of control works is a crucial step to reduce landslide risk. An important issue is to identify and calculate the proper input data such as channel characteristics (slope, length and width); local topography and main landslides characteristics. Considering the relevance of this issue, the next section summarizes the main suggestions provided by the literature.

3.2.1 Input data

An accurate knowledge of the landslide characteristics along the path and on the fan is essential for the design. These characteristics include: i)

the frequency, ii) design magnitude or volume, iii) maximum discharge and flow velocity, iv) size of debris, v) likely flow paths, vi) potential runout distance, vii) potential impact forces and viii) probable storage angle (VanDine, 1996; Lo, 2000).

The considerations on the occurrence of the landslides depend on historic assessment with a view toward any changing conditions throughout watershed (Hungr et al., 2005).

Several formulations exist to estimate the volume of landslides; Hungr et al., 1984 and VanDine, 1996 correlated the event magnitude with the size of catchment area (Fig. 3.11) while Hungr et al., 1984 with the length of the channel and the erodibility coefficient. Volume estimates for past debris flows can be derived from detailed surface mapping of previous deposits and from subsurface evidence from test pits and trenches in fan deposits. Volumes of deposits can also be estimated with the use of photogrammetry or by ground based survey techniques, including pace or tape measurements, electronic distance metering, ground penetrating radar, or seismic methods (Jakob, 2005).

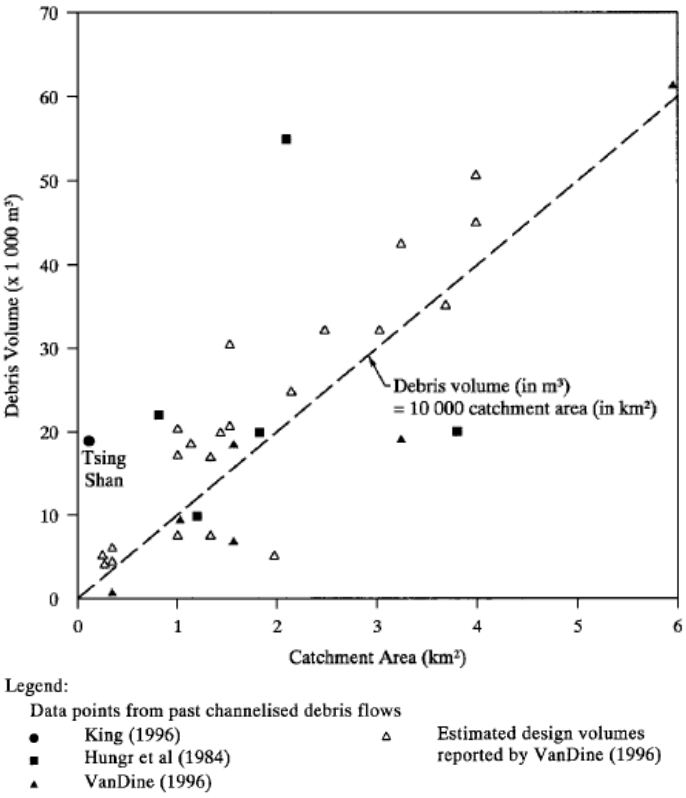

Figure 3.11 Estimated and recorded design volumes versus Catchment area in British Columbia (Lo, 2000).

The maximum discharge of landslide depends on the channel geometry and flow velocity. Hungr et al., 1984, PWRI, 1988 and Mizuyama et al., 1992 formulated an empirical correlation between peak of discharge and total debris volume based on field measurement and laboratory flume tests (Fig. 3.12).

Several equations are proposed to estimate the maximum (mean cross-sectional) velocity of the frontal part of debris flows and they depend on the chosen rheology to describe the landslide behavior (See Section 2.3, Table 2.1).

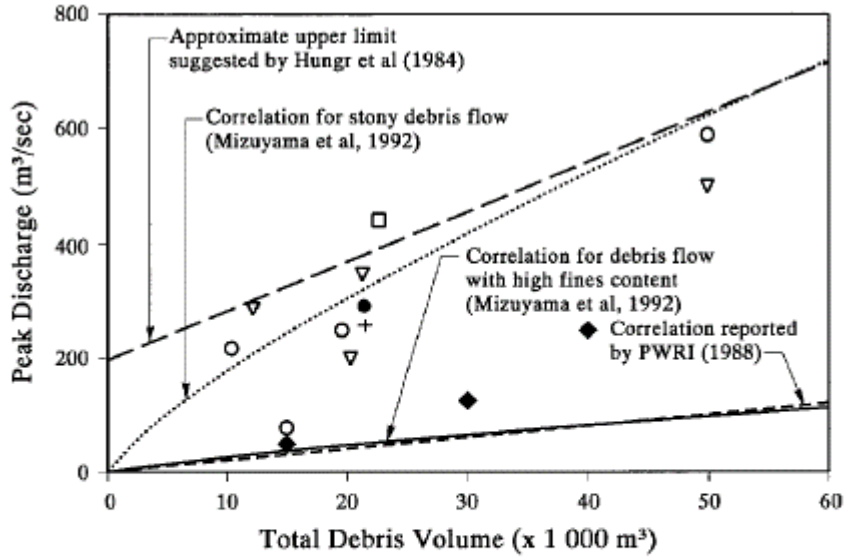

Legend:

Methods of estimating peak discharge for debris flow events in British Columbia:

- ● Eyewitness records
- ◆ Flood discharge
- ▽ Super-elevation data
- \+ Weir formula
- □ Model tests
- ○ Velocity equation

Figure 3.12 Peak discharge versus total debris flow (Lo, 2000).

The estimate of debris size can be derived from observations of channel bed and sides and debris fan; while very difficult is the estimate of flow path because depends on morphology, landslide characteristics and the presence of natural or artificial obstacles.

The potential run-out distance is evaluated through empirical and analytical methods, small or large-scale laboratory tests and numerical methods (see Section 2.3).

The design of many types of debris control works should consider the potential impact forces, both dynamic thrust and point impact forces, at various locations on the debris fan (VanDine, 1996). Hungr et al. (1984) summarized the calculation of dynamic impact force as a function of density of debris, cross-sectional area of flow, velocity of flow, and the

angle between the flow direction and face of the structure. Recently, Calvetti et al. 2017 proposed a new formula for the impact force in which the front inclination, flow height and others mechanical behavior and properties of the impacting material (stiffness and density) are considered.

Finally, VanDine 1996 define the relationship between the probable storage angle and the storage basin capacity (Fig. 3.13).

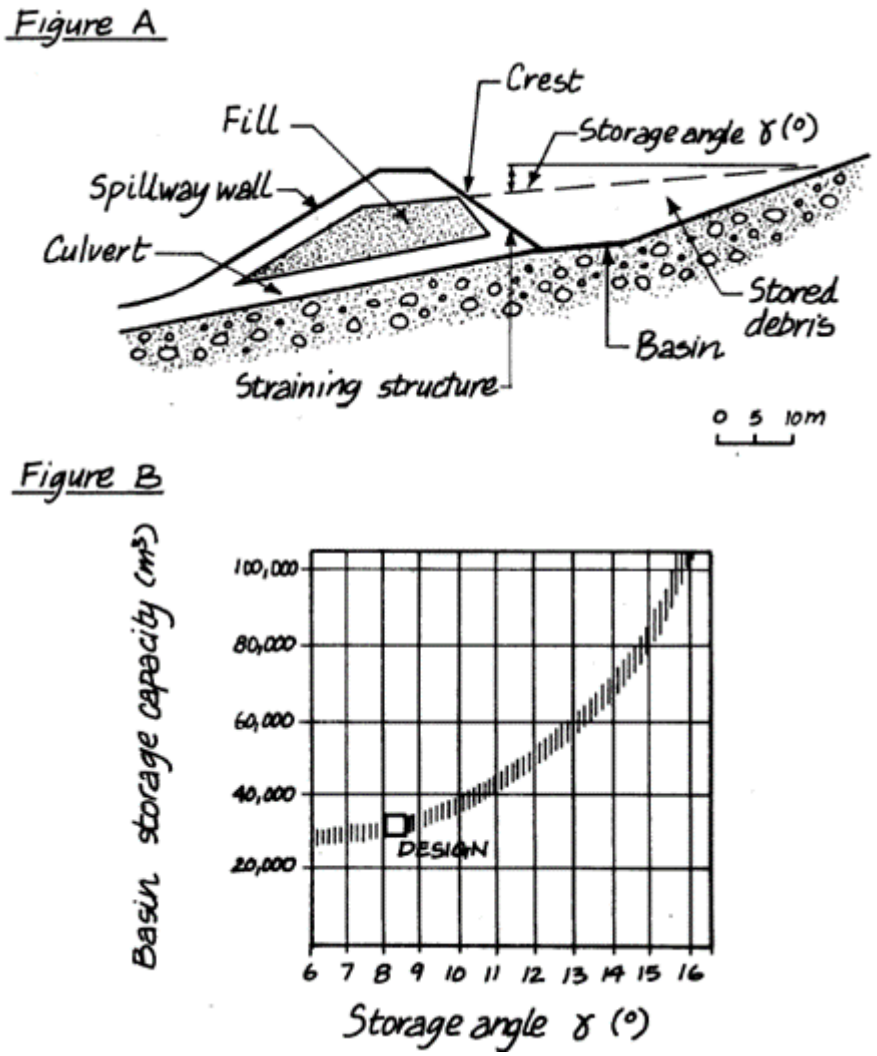

Figure 3.13 Storage angle definition (A) and the relationship with storage basin capacity (B) (VanDine, 1996).

The Table 3.1 summarizes the needed landslide characteristics for the design of all passive control works examined in Section 3.2.

Table 3.1 Design input data for passive control works.

Type of control works	Landslides characteristics						
	Volume	Maximum discharge	Debris Size	Flow paths	Runout distance	Impact forces	Storage angle
Deposition areas	×			×	×		×
Baffles	×			×	×	×	
Check dams		×		×		×	
Lateral walls		×				×	
Deflection walls							
Terminal wall	×			×	×	×	×
debris racks and debris barriers	×		×	×		×	×
Storage basins	×		×		×	×	×
Rack	×	×	×	×	×		

3.2.2 Considerations

The main design considerations concern the location, the geometric characteristics and maintenance of passive control works. As it concerns the location; the deposition areas, baffles, terminal wall, storage basin and racks are located downstream; lateral and deflection walls along the channel and the check dams according to their functions can be placed along the channel or downstream. In the first case, they have to slow down, intercept or diverge the flows to downstream; in the second case they have to limit the erosion process of the flow.

The storage basins due to their cross sections, low slope and presence of obstacles (e.g. baffles), encourage flow expansion and decrease the velocity. The basin slope is 1/2 or 2/3 of the natural initial slope of the flow before the entrance in the control works (Piton and Recking,

2015). The basin shapes are mainly determined by local topographic constraints to limit the leveling costs and the number of retaining walls to build (Piton and Pecking, 2015); the shape regularly adopted is that of a pear (Zollinger 1983). A large inlet side with a narrow outlet side tends to maximize sedimentation; on the contrary, a narrow outlet side with a large outlet side promotes self-cleaning (Zollinger 1985) (Fig. 3.14).

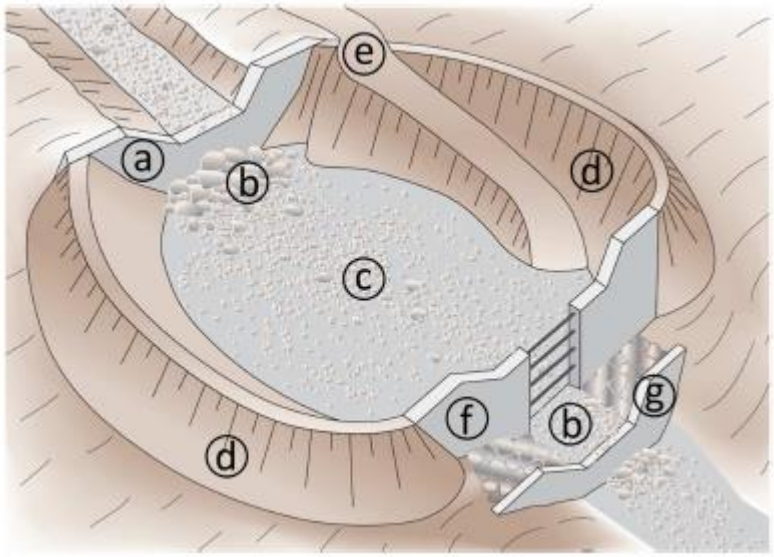

Figure 3.14 Components of a storage basin with an open check dam: (a) inlet structure: solid body dam; (b) scour protection; (c) basin; (d) lateral dikes; (e) maintenance access; (f) open check dam; (g) counter dam (Zollinger 1983, Piton and Pecking, 2015).

For the design of storage basins it is important the correct entrance of the flow and the separation of fine and coarser particles from water flows through the debris rack or check dams upstream or downstream (Versace et al., 2008) (Fig. 3.15).

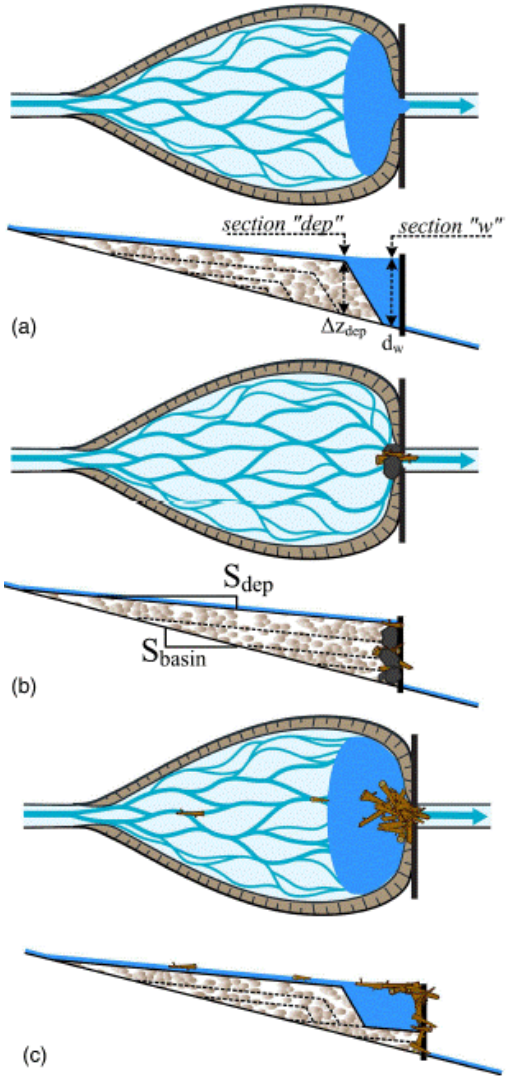

Figure 3.15 Plan and longitudinal sections of a storage basin with check dam downstream: (a) hydraulic control of the deposits: this condition is induced by an obstacle to the flow (narrower dam openings when compared to the natural channel section) (b) mechanical control of the deposits: boulders and driftwood jamming leading to open check dam clogging; (c) mixed controlled deposits: hydraulic control and mechanical control (Lange and Bezzola 2006, Piton and Pecking, 2015).

As it concerns the check dams, it is possible to distinguish between solid body dams and open check dams; open dams characterized by a variety of apertures (slits, grids, screens and nets) have been installed and studied in countries including Japan (Okubo et al. 1997, Watanabe et al. 2008, Ikeya 1989), Austria (Hübl et al. 2005; Jaeggi and Pellandini, 1997), Taiwan (Lien, 2003), Switzerland (Wendeler et al. 2008) and Canada (Hungr et al. 1984). These studies analyzed the width and spacing of the openings in the dam, the upstream storage area required behind the dam, impact forces that can be expected on the dam, the height of the vertical components and the factors that influence spacing of check dams (VanDine, 1996) (Fig. 3.16).

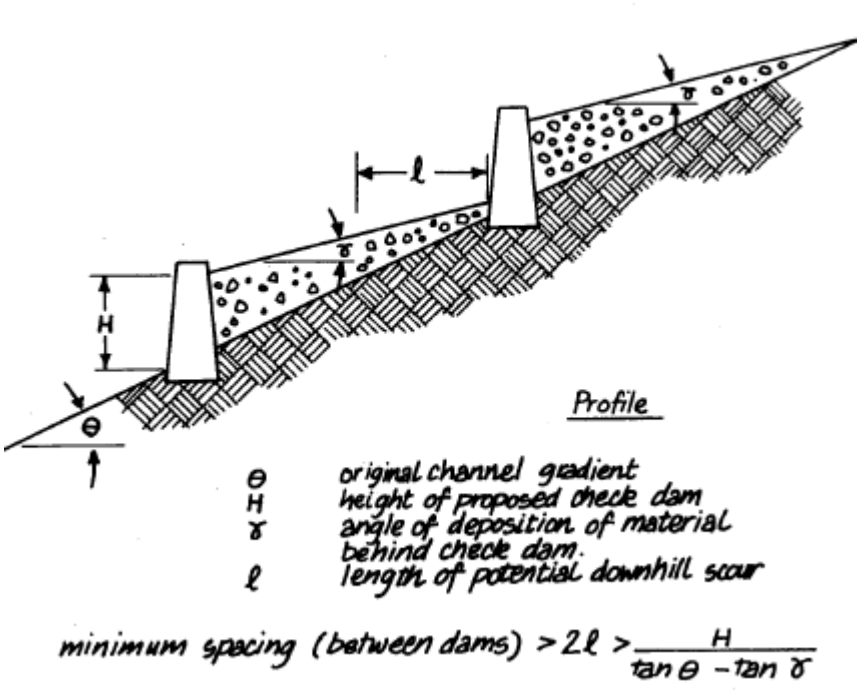

Figure 3.16 Determination of minimum spacing between dams (VanDine, 1996).

The racks geometry depends on the local topography; Brunkal, 2015 demonstrates that higher is the rack length, higher is the intercepted volume. An important issue is the determination of screen slope and opening size or slit aperture of the rack. Watanabe et al. (2008) included

a table (reproduced as Fig. 3.17) with values for six screen and beam designs at Japanese sites (Brunkal, 2015), while an example of a rack design in Colorado is shown by Brunkal, 2015.

		Mt. Fuji			Mt. Yakedake	Mt. Sakurajima	Mt. Tokachidake
Screen	Longitudinal slope	1/10	1/40	1/40	1/14	Horizontal	Horizontal
	Shape type	I	△	△	□	▽	▽
	Size	200*150*9*16 mm	200*200*25 mm	200*200*25 mm	200*200*8mm	255*270*205*9mm	255*270*205 9mm
	Slit aperture	10-15 cm	15 cm	15.60 com	20 cm	40 cm	40 cm
	Transmissivity	50%	35%	56%	50%	66.70%	66.70%
Beam	Shape type	H	H	H	H	H	H
	Size	300*300*10*15mm	400*400*13*21mm	400*400*13*21mm	400*400*13*21mm	900*300*16*18 mm	800*300*14*26 mm
	Spacing	2.925m	2.29m	2.29m	2.5m	3.0m	2.5-3.5m

Figure 3.17 Characteristics of six racks installed in Japan (Brunkal, 2015). For the components of rack, see Figure 3.4.

The maintenance must be planned during design phase, the emptying methods for partially or totally filled control works (Versace et al., 2008).

3.3 DISCUSSION

The control works are designed to contain, stop or diverge the landslides. Several type of control works have been described, with special attention to the permeable racks, analyzed through pilot project and flume tests. Some considerations have been made on design input data and other factors e.g. location, geometry and maintenance of control works. However, few literature studies analyzed the kinematic characteristics of the flow or the flow regime (supercritical, critical or subcritical) for design purposes. There are not studies that evaluate the

efficacy and efficiency of control works for different flow like phenomena.

Indeed, several question can arise during the design stage and among these the most relevant are: is it right to design a permeable rack for mudflows? Or a storage basin for flash floods, water floods or hyperconcentrated flows?

Answering to some of these relevant questions is the main purpose of this PhD thesis.

4 EVALUATING THE KINEMATIC CHARACTERISTICS OF FLOWS THROUGH FROUDE NUMBER

The flow-like mass movements are characterized by different kinematic quantities: velocity, height and path of the flowing mass. These quantities consist of spatial and temporal dependent variables and their study is usually carried out through field observations, flume tests and numerical modeling. Since none of these fundamental kinematical features can be disregarded to fully understand the behavior of a flow, a new landslides descriptor, including all of them, was proposed in the nineties. The so-called Froude number (Fr) is a dimensionless number widely used in Hydraulic engineering, able to identify the flow regime. Fr is expressed as the ratio of inertial and gravitational forces $Fr=U/(gL)^{1/2}$, being U a characteristic flow velocity, g the gravitational acceleration, L a characteristic length. For shallow water waves traveling over channels of low inclination, the Froude number simplify to $Fr=u/(gh)^{1/2}$, being u the flow velocity, averaged over the cross-section perpendicular to the flow direction and h the flow height. In the case of rectangular channels, when the velocity u is larger than the propagation rate of small disturbances $(gh)^{1/2}$ at a given cross section, the fluid is classified as locally supercritical and it is presented as shallow and fast, in the opposite case the fluid is subcritical, deep and slow (Campbell et al., 1985).
Several authors investigated the Froude number through flume tests and numerical modeling. In the following the main observations are described.

4.1 EXPERIMENTAL AND ANALYTICAL EVIDENCES

The first experimental tests aimed at identifying the kinematic characteristics of non-Newtonian fluids were made by Campbell et al. (1985). They carried out flume tests with granular material, taking into account different sizes of glass beads in order to investigate the dependence of the flow regime from the channel geometry (length, width and channel slope), the grains size and the gate opening. Campbell showed that supercritical flows are completely controlled by the gate opening (upstream boundary conditions), while subcritical flows depend on the material and channel features (downstream boundary conditions). The Figure 4.1 reveals that for subcritical flows the depth downstream of the channel for different gate opening (h_g in the picture) converges in a single point; while for the same flows there are large variations of the Froude number by varying the channel length to width ratio (L/B), the channel slope (α) and the material type (BT6 and BT4) (Fig. 4.2).

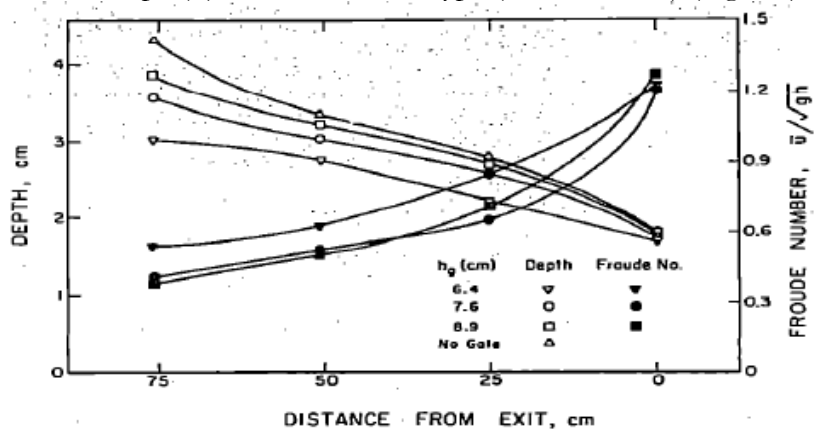

Figure 4.1 Subcritical flow depths and Froude numbers near the channel exit (Campbell, 1985).

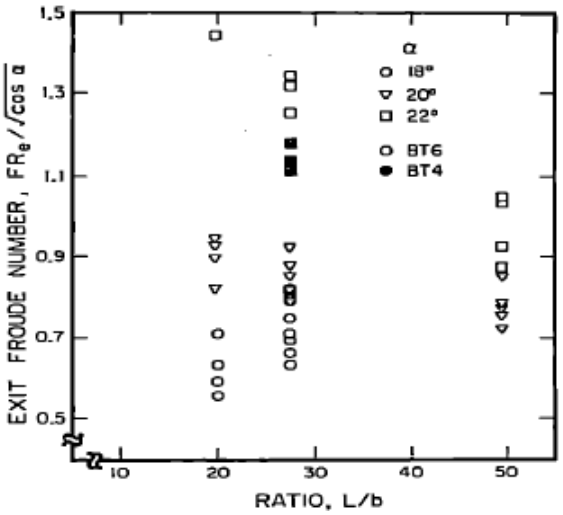

Figure 4.2 Froude numbers close to the channel exit as a function of channel geometry and material type (Campbell, 1985).

Pouliquen (1999) carried out experiments on the rapid flows of glass beads down rough inclined surfaces and the experimental observation showed the independence on the flow kinematic of the channel slope and roughness condition of the channel. Indeed, the curves obtained for different channel slope or rough surface (System 1, 2, 3 and 4 in the picture) collapse onto a straight line (Figs 4.3 a, b). The function h_{stop} represents the depth when the flow is about to stop.

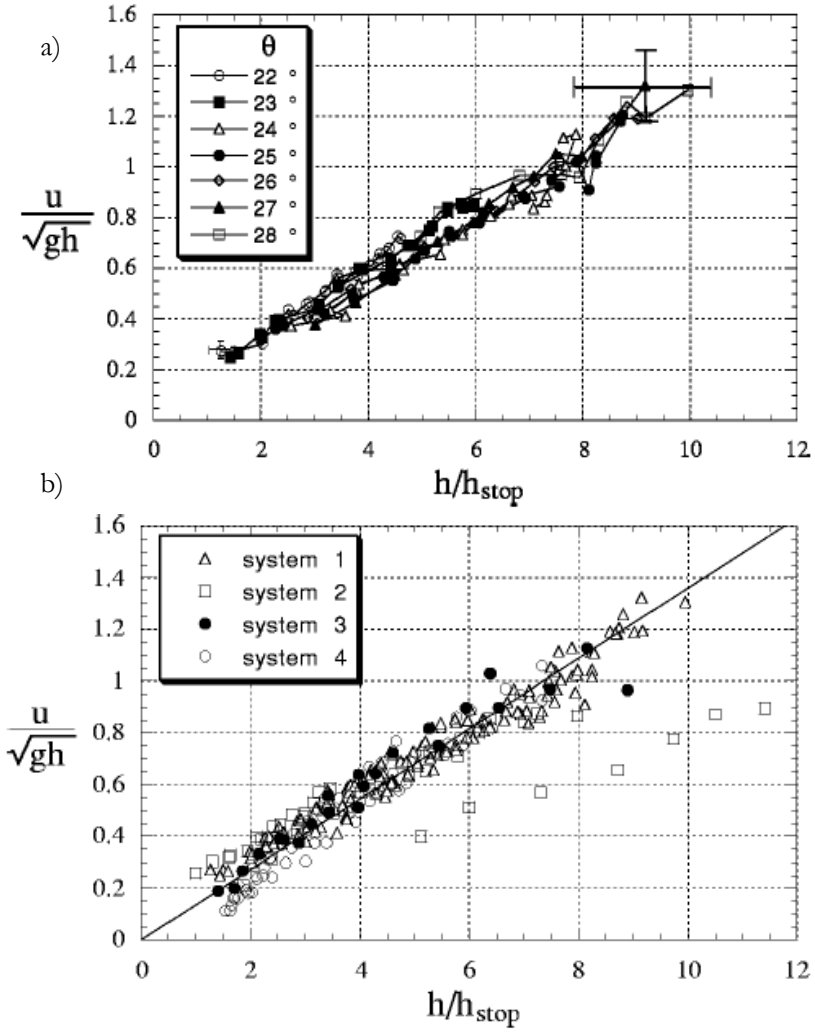

Figure 4.3 Froude numbers as a function of h/h_{stop} a) for different channel slope "θ" and b) for ascending rough surfaces "system 1-4" (Pouliquen, 1999).

Choi et al., 2015 evaluated on a small scale flume the *Fr* behavior of uniform dry sand and water flows, taking into account the influence of channel slope, initial volume and energy-dissipation mechanisms on kinematic characteristics. The main conclusions are listed below:

- Fr depends on energy-dissipation mechanisms; dry sand dissipates energy from a combination of boundary shear, deformation of the granular mass, and internal friction between grains; while the water relies predominantly on boundary shearing (Choi et al.,2015);

- larger initial volumes and shallower channel inclinations for both granular and water flows determine lower Froude number (Choi et al, 2015);
- the influence of the initial volume has a more substantial effect on reaching lower Fr numbers compared to adopting shallower inclinations (Choi et al., 2015);
- there is a huge difference between granular flows and water in the triggering stage; indeed the release of frictional materials is restricted by its internal shear strength, whereas for water is an instantaneous process (Choi et al., 2015).

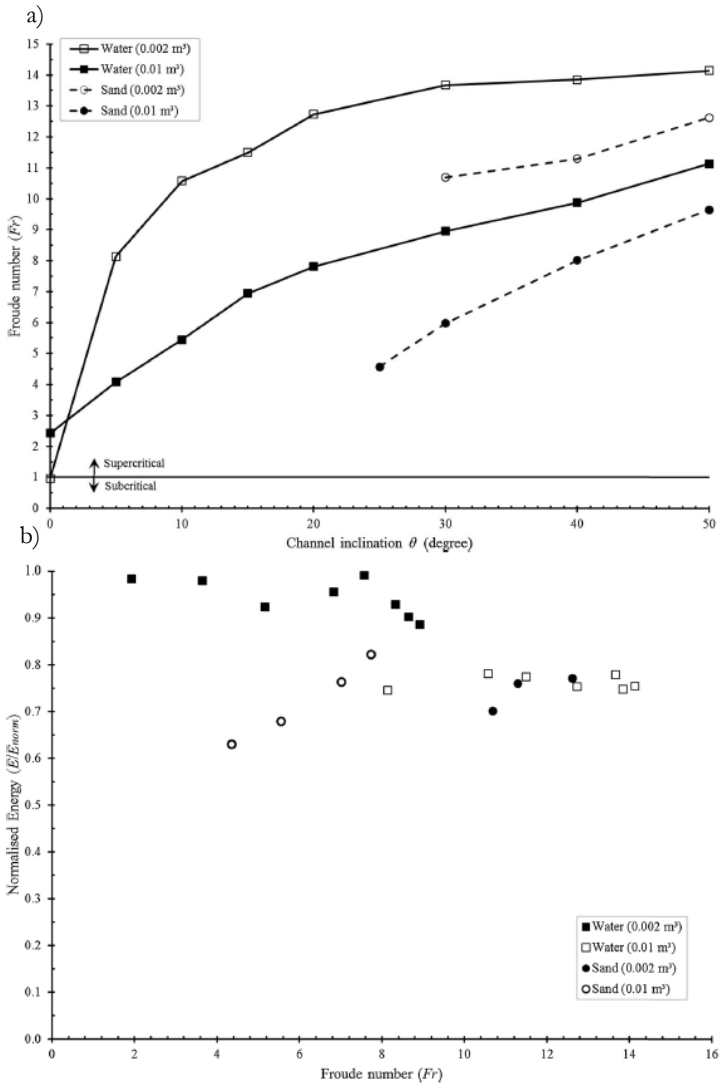

Figure 4.4 a) Froude numbers as a function of channel slope and b) normalized energy (Choi et al., 2015).

Later, it was analyzed experimentally and analytically the transitional behavior of dry granular materials and viscoplastic fluids from a supercritical to subcritical state (hydraulic jump) in open channel (Pudasaini et al., 2007; Ugarelli and Di Federico, 2007; Coussot, 2012).

Pudasaini et al., 2007 performed laboratory experiments of dry granular flows impinging an obstructing wall in a channel. The impact leads to a

sudden change in the flow regime from a fast moving supercritical thin layer to a stagnant thick heap with variable thickness and a surface dictated by the angle of repose typical of the material. The Figure 4.5 shows a graphical interpretation of critical height that is the height that represents the transition of the flow from the supercritical to the subcritical state. In the jumper is possible to recognize two slope: the front slope and deposition slope; drawing the two tangents "T1" and "T2" respectively, and taking the interception of the tangents, the critical height is taken to be the distance of this interception from the sliding base of the channel (red line).

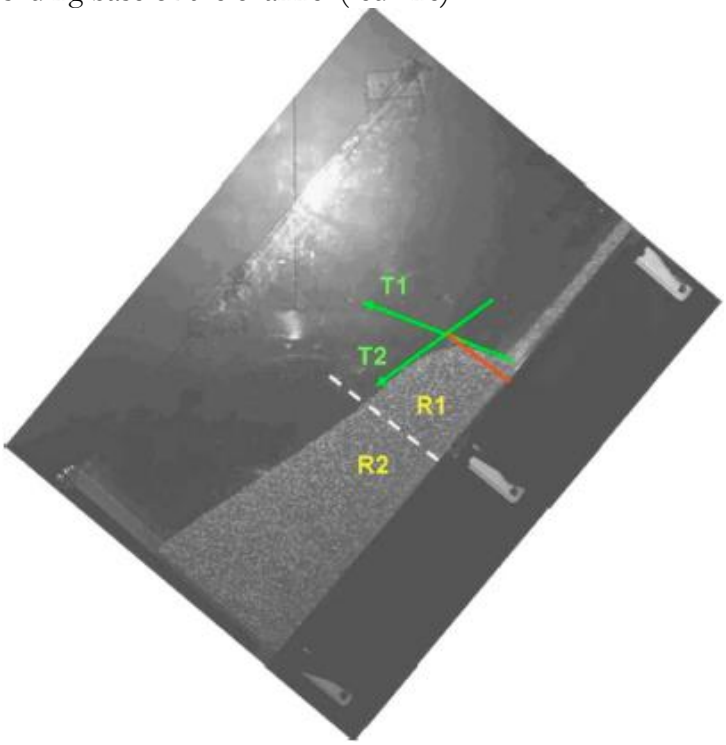

Figure 4.5 Graphical interpretation to identify the critical height (red line) (Pudasaini et al., 2007).

An analytic expression for critical height is provided by Ugarelli and Di Federico, 2007 for Herschel-Bulkley fluids. The critical height increases monotonically with the behavior index and exhibits a relative maximum respect to the bottom shear stress (Fig. 4.6).

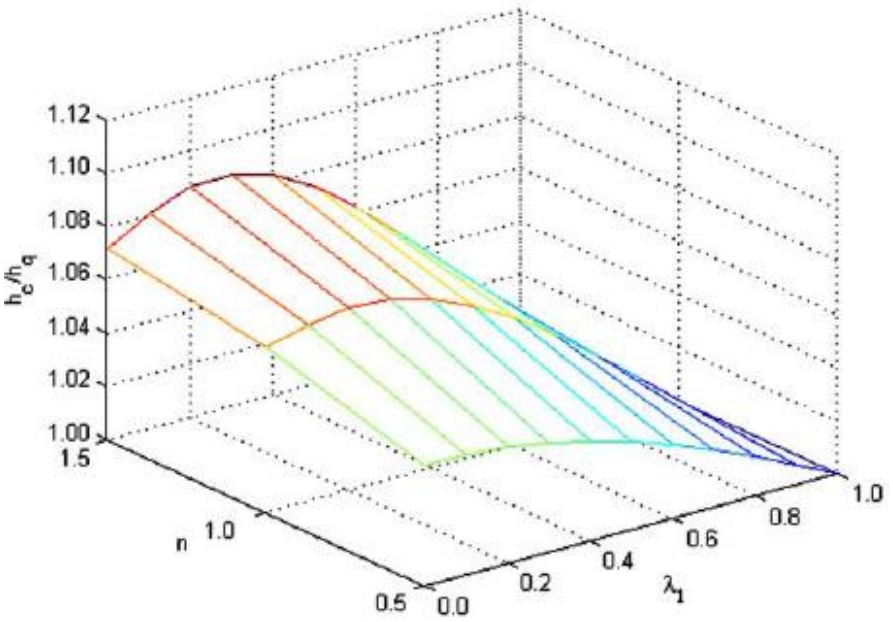

Figure 4.6 Critical depth (h_c) versus λ_1 (shear stress) and behavior index (n).

Coussot, 2012 obtained a less precise but more practical expression of the critical height assuming that in each cross-section the velocity distribution is approximated by the velocity distribution of an uniform flow. In these conditions the critical height is a function of the flow height in a section in the proximity of the jump and the Froude number in the same section.

Haldenwang et al., 2010 eased the delineation of the role of the Froude number in the nature of flows through flume tests with rheologically different kinds of fluid. In particular, they identified laminar, transitional and turbolent flow regimes through such dimensionless number. Under specific operating conditions, when the flow is non-Newtonian and becomes more viscous, it is much more probable that laminar flow will be encountered; unlike the case of water mainly turbulent flow (Haldenwang et al.,2010).

4.2 NUMERICAL MODELS INSIGHTS

Triggering and propagation mechanisms in small-scaled flume tests are carried with limited amount of volumes to be loaded upstream; this initial condition leads to scaled flow depths, flow velocity and Froude number which are transferred to the reality by applying a model of similarity, an operation not always smooth because performed under some restrictions e.g. yielding the Froude or the Reynolds models. Another aspect is due to frictional materials that are not conducive to achieving lower or even subcritical numbers for small scale modeling. Indeed the mass to flow needs has to overcome its shear strength and interface friction angle along the channel bed, for this reason higher channel inclinations are necessary to accelerate the flowing mass. For all these reason more recently, Domnik and Pudasaini 2012 and later Domnik et al., 2013 investigated, through the numerical modeling, the generalised Froude number for non-depth averaged flows. A dense granular flow or viscoplastic granular flow down an inclined channel was studied numerically with the finite-volume method (Fig. 4.7). An innovative rheological model was used; the internal deformation was modelled as a viscoplastic material while the interaction of the flow with the solid boundary was described by the pressure and rate-dependent Coulomb-viscoplastic sliding law (Domnik and Pudasaini 2012). Generally, for depth averaged flows the pressure is the overburden pressure (material normal load), i.e., the hydrostatic pressure, which is independent of the flow dynamics; Domnik and Pudasaini, 2012 link the normal pressure to the shear-stress on the wall and so generating a slip velocity on the channel bottom. They analyzed three different basal boundary conditions: no-slip, free-slip (pressure-independent), and the Coulomb-type slip (pressure-dependent) at the base (Fig. 4.8) and concluded that the dynamic pressure differs considerably from the hydrostatic pressure; e.g. in extensional flow regimes the hydrostatic pressure largely overestimates the full dynamic pressure, whereas in strong compressional flows, e.g., in the vicinity of flow obstacle interaction, an underestimation may be observed. Later, they introduced the extended Froude number (Eq. 4.1), which includes both the pressure potential and gravity potential energies:

$$Fr = \sqrt{\frac{u^2+w^2}{g\left((L-x)\sin\varsigma + z\cos\varsigma\right)+\frac{p}{\rho}}} \tag{4.1}$$

where: u^2+w^2 is related to the kinetic energy; $g(L-x)\sin\varsigma$ is the potential energy caused by the downslope gravitational acceleration; $g\,z\cos\varsigma$ is the potential energy caused by the gravitational acceleration along the flow depth and p/ρ is the pressure potential energy.

In the case of granular flow on inclined channel, the Froude number increases downstream as the kinetic energy increases and the potential energy decreases; while it generally decreases from the free surface to the bottom of the flow because of the monotonically increasing of the frictional resistance towards the base of channel (Fig. 4.9).

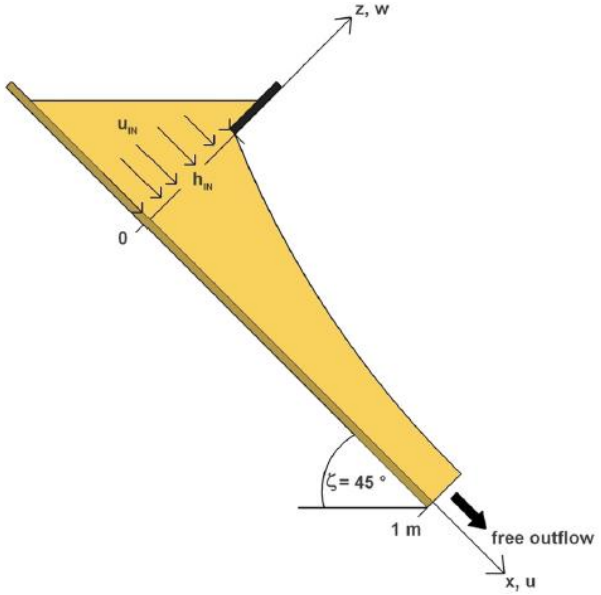

Figure 4.7 Inclined channel used for the numerical modeling of granular material. The material enters into the channel at x = 0 with an inlet height equal to 15 cm and an average inlet velocity of 0.9 m/s (Domnik and Pudasaini 2012).

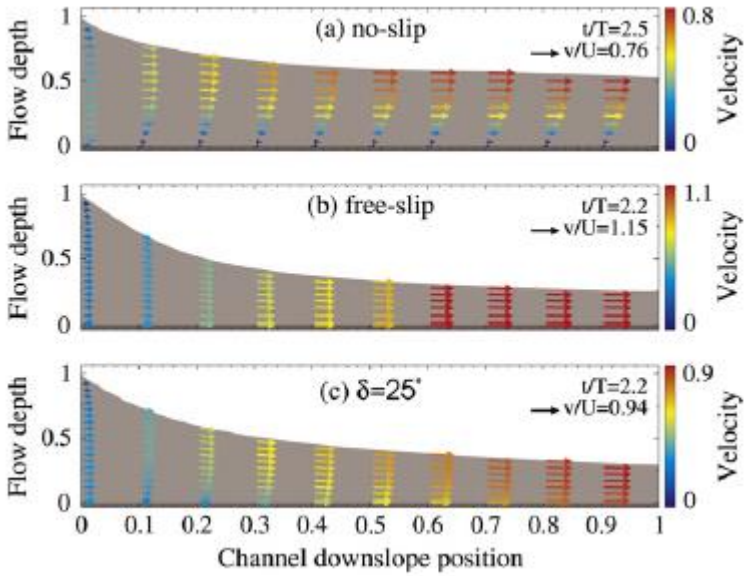

Figure 4.8 Flow depth and velocity for three different basal boundary conditions: a) no-slip; b) free-slip and c) Coulomb friction law with friction angle equal to 25° (Domnik and Pudasaini 2012).

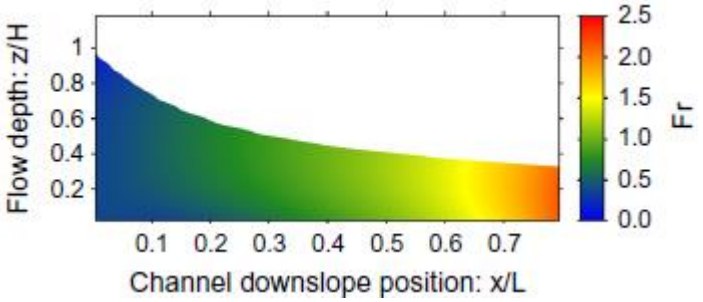

Figure 4.9 Generalized Froude number for Coulomb friction law with friction angle equal to 25°(Domnik and Pudasaini 2012).

The analysis of the Froude number showed that granular flows on inclined surfaces are characteristically rapid supercritical flows (Domnik and Pudasaini, 2012). Later, Domnik at al., 2013 presented a new mixed model: depth-averaged model (DAM) in regions with smooth changes of flow variables and non-depth-averaged model (N-DAM) in the initiation

and deposition regions particularly, when the flow hits an obstacle or a control work (Fig. 4.10).

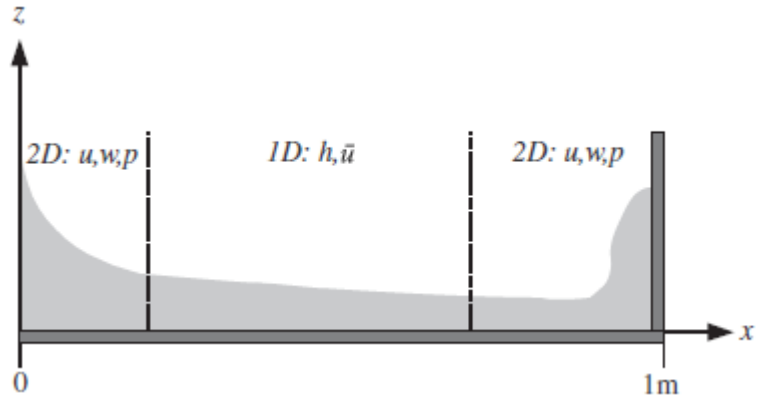

Figure 4.10 A possible domain decomposition: the 2D model supplies the velocities *u*, *w*, and the pressure *p*; the 1D model provides the flow depth *h* and the depth-averaged downslope velocity *ū* (Domnik et al., 2013).

The authors introduce the shallowness parameter as a function of Froude number that indicate that close to the silo inlet the *w* velocity component is of the same order as the *u* velocity component. At some distance from the inlet, the *w* component becomes negligible. So, in regions with high momentum transfer in the flow depth direction, depth-averaging is not valid and the full two-dimensional model must be used (Domnik at al., 2013) (Fig. 4.11).

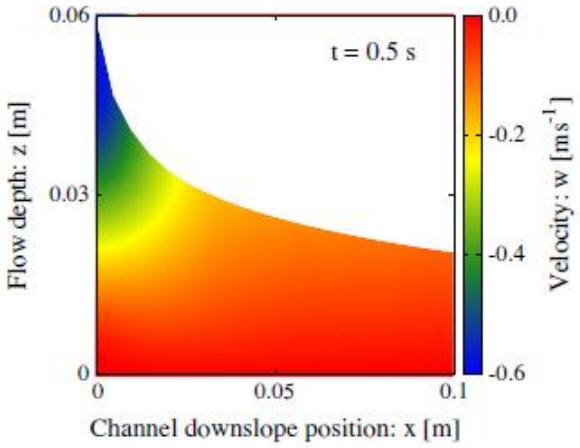

(a) The w velocity in flow depth direction.

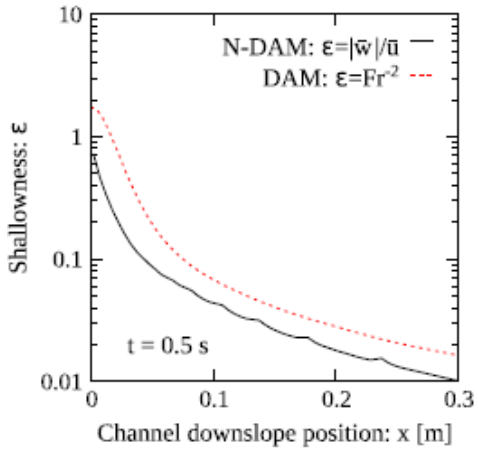

(b) Shallowness parameter.

Figure 4.11 Simulation of the velocity component in the flow depth direction (*w*) and shallowness parameter, in the vicinity of the silo inlet (located at x = 0) (Domnik et al., 2013).

Pokhrel, 2014 reworks the model described above with a special focus on the two-phase debris flows and introduces the solid-only, and fluid-only Froude numbers depending on fluid contribution to flow height; solid contribution to flow height; the lateral hydraulic pressure

parameters for solid and fluid. The solid lateral pressure is negligible if the distribution of solid can be approximated to be uniform along the down-slope direction; while the fluid lateral pressure is negligible if locally some part of the debris is solid dominated. According to Iverson et al., 2010 the solid pressure is very high in the "head" of debris flow and the fluid pressure in the "tail"(Fig. 4.12).

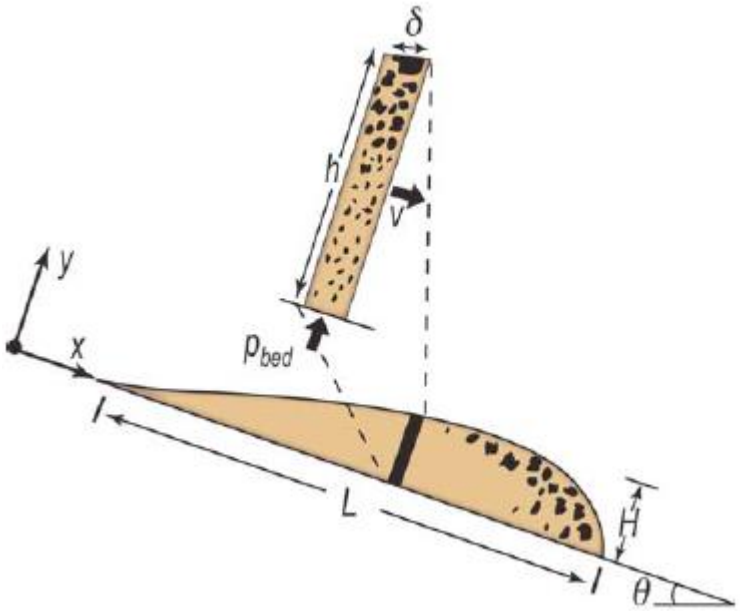

Figure 4.12 Schematic vertical cross section of a debris flow (Iverson et al., 2010).

The equations (4.2) and (4.3) of solid and fluid phase Froude number are following:

$$Fr_s = \frac{u_s}{\sqrt{0.5\,\beta_s\,(h_s+h_f)}} \tag{4.2}$$

$$Fr_f = \frac{u_f}{\sqrt{0.5\,\beta_f\,(h_s+h_f)}} \tag{4.3}$$

Where: u_s and u_f are solid and fluid contribution to flow velocity; h_s and h_f solid and contribution to flow height; β_s and β_f lateral hydraulic pressure parameters for solid and fluid.

4.3 DISCUSSION AND PROPOSED APPROACH

The kinematic characteristics, the transition from supercritical to subcritical flow, the evaluation of critical height and the different formulations of the Froude number were described for the non-Newtonian flow regime (subcritical, critical or supercritical and laminar, transitional or turbulent) through experimental, analytical and numerical evidences.

Moreover, many studies evaluate the impact mechanisms trough the Froude number on the structures highlighting that supercritical and subcritical impact can lead to entirely different mechanisms. Armanini et al. (2011) and Choi et al. (2015) reported that supercritical water flows impacting a rigid barrier resulted in a vertical jet mechanism, whereas subcritical water flows resulted in a mild reflective wave mechanism. Calvetti et al. 2017 proposed a formula for the impacting force of non-Newtonian fluid. Only recently, Pokhrel, 2014 introduced the *Fr* as the useful descriptor of the flow behavior for control works design.

The main goal of this PhD thesis is to analyze the use of the Froude number as a quantitative descriptor of the flows behavior and the control works response and, more generally, as an useful tool to estimate the efficiency of exiting control works as well as to proper design the new ones. The Froude number discriminates two different kinematical features: subcritical or slow and supercritical or rapid. The latter, behaving like a "blind" flow, is not influenced by down slope boundary conditions such as the presence of obstacles and other flows. So, for the first flow types the downstream control works (e.g. storage basins) could be efficient; while for the supercritical flows they could be inefficient unless these control works are associated to other structures capable of producing the transition from supercritical to subcritical flow before the impact.

The kinematic characteristics of the flowing mass and the related Froude number are studied through the numerical modeling in the following

chapters, by considering before simplified geometry of channel and mass and then real case studies.

5 KINEMATIC CHARACTERISTICS OF NEWTONIAN AND VISCOPLASTIC FLOWS THROUGH FV MODEL

The scientific literature quotes few studies concerning the regime of hyperconcentrated flows and mudflows, that is deepened in this Chapter to clarify kinematic behavior of viscoplastic fluids, starting from well-known kinematic characteristics of water flows. To this aim, a 1D numerical scheme developed by Rendina et al., 2017 and a commercial CFD package (Flow-3D model) to estimate the regime of Newtonian and non-Newtonian fluids flowing in an open channel was used. 1D De Saint Venant equations in the former case and full Navier-Stokes equations in the latter case were solved (Rendina et al., 2017).

Lots of schemes are available to solve the non-linear partial differential equations ruling fluid motion, most of these are based on structured and unstructured grids, respectively finite differences, finite elements and volumes and finally meshless method like the smoothed particle hydrodynamics (SPH) method (Pastor et al., 2009b; Pugliese Carratelli et al., 2016 and Cornelius and Bernt, 2014). The latter method will be used in the next Chapter, while in this work a finite volume (FV) approach is used being suitable for the present investigation. The numerical results show a good agreement with known solutions from the literature and reveal viscoplastic flows mainly supercritical (Rendina et al., 2017).

5.1 GOVERNING EQUATIONS

-1D mathematical model

A one-dimensional, incompressible and unsteady flow over an inclined surface of an homogeneous medium, with initial height h_{in} and length L_m,

having an indefinite length and being inclined of an angle θ respect to the horizontal were considered. The evolution of the system is described with reference to the coordinate system $\{x, y\}$ shown in Figure 5.1. It was assumed: i) the physical quantities depth-averaged, since many fast mass flow movements have small depths with low gradients in comparison with their length or width; ii) the flow is unconfined, so the flow resistance is only offered at the channel bottom. (Rendina et al., 2017). Flow motion is described by the following set of non-linear partial differential equations (PDEs), i.e. the De Saint Venant equations:

$$\frac{\partial h}{\partial t} + \frac{\partial (hu)}{\partial x} = 0 \qquad (5.1a)$$

$$\frac{\partial (hu)}{\partial t} + \frac{\partial \left(0.5\, g \cos\theta\, h^2 + hu^2\right)}{\partial x} = ghsin\theta - ghS_f \ \frac{u}{|u|} \qquad (5.1b)$$

The Equations (5.1a) and (5.1b) are based on mass and momentum conservation principles respectively; the meaning of symbols follow: h the flow height, u the depth-averaged flow velocity, g the gravitational acceleration, t the physical time and S_f the resistance at the bottom. The closure of the problem is provided by specifying the relation between stress and strain (rheological characterization of the mixture), and appropriate boundary conditions (Martino and Papa, 2008).
In this work, the flow resistance term S_f appearing in Equation (5.1.b) refers to one-phase fluid which describe the flow behavior of a mixture of water and fine material (Naef et al., 2006).
The mixture of water and sediments representing a mudflow or hyperconcentrated flow may be described as a Newtonian or a Bingham fluid, respectively yielding for resistance term to the equations:

$$S_f = \frac{u^2}{\chi^2 R_i} \text{ with } \chi = \frac{87}{1+\frac{m}{\sqrt{R_i}}} \qquad (5.2a)$$

$$S_f = \frac{\mu_{eff}\dot{\gamma}_u}{\rho g h} + \frac{n_m^2 u^2}{h^{4/3}} \text{ with } \mu_{eff} = \mu\frac{10^B + K_B\dot{\gamma}_u}{1+K_B\dot{\gamma}_u}; \mu_{eff} = \mu\frac{10^B + K_B\dot{\gamma}_u}{1+K_B\dot{\gamma}_u};$$

$$K_B = \frac{10^B \mu}{\tau_y} \qquad (5.2b)$$

The Equation (5.2a) corresponds to the Chézy formula in which χ is the roughness coefficient; m is the roughness index and R_i the hydraulic

radius, equal to the flow height h in an infinitely wide channel. The equation (5.2b) represents the Quadratic formulation combined with the rheological model of Bingham (Shao and Lo, 2003). The first term in RHS of equation (5.2b) is linked with the Bingham model while the latter is related to the turbulent and dispersive components, being n_m the Manning roughness coefficient.
The Cross formulation is commonly used to model non-Newtonian flows and can be represented as (Shao and Lo, 2003):

$$\frac{\mu_0-\mu_{eff}}{\mu_{eff}-\mu_\infty} = (K_B\dot{\gamma}_u)^n \tag{5.3}$$

where μ_0 and μ_∞ are viscosity at very low and very high shear rates, respectively; μ_{eff} is the effective viscosity of the fluid; $\dot{\gamma}_u$ the shear rate; K_B and n constant parameters (in this case n=1) .
Since this model presents four rheological parameters it was possible refer to Bingham fluid parameters, characterized by an effective viscosity that can be represented as:

$$\mu_{eff} = \mu + \frac{\tau_y}{\dot{\gamma}_u} \tag{5.4}$$

where τ_y and μ are the Bingham yield stress and the dynamic viscosity of the mixture, respectively.
Under the condition of $K_B \cdot \dot{\gamma}_u >> 1$, K_B and μ_∞ are expressed as (Shao and Lo, 2003):

$$K_B = \frac{\mu_0}{\tau_y} \quad and \quad \mu_\infty = \mu \tag{5.5}$$

In the Bingham model μ_{eff} reaches an infinite value when the shear rate tends to be infinitesimal, so to avoid numerical indivergences Hammad and Vradis, 1994 proposed $\mu_0=10^3\mu_\infty$ (Hammad and Vradis, 1994). Finally, C_v is the volume sediment concentration with a and β derived from field assessments and empirical data (Martinez et al., 2011 and Lanzini 2012).

-2D mathematical model

2-dimensional and unsteady Newtonian/non-Newtonian flows were simulated by the Flow-3D solver (Flow-3D user manual v. 9.4). In this case, variables are not depth averaged. Therefore, ruling equations of mass (Eq. 5.6a) and momentum (Eqs. 5.6b-c) conservation are expressed as:

$$\frac{\Omega}{\rho c^2}\frac{\partial p}{\partial t} + \frac{\partial}{\partial x}(u\Sigma_x) + \frac{\partial}{\partial y}(v\Sigma_y) = 0 \qquad (5.6a)$$

$$\frac{\partial u}{\partial t} + \frac{1}{\Omega}\left(u\Sigma_x\frac{\partial u}{\partial x} + v\Sigma_y\frac{\partial u}{\partial y}\right) = -\frac{1}{\rho}\frac{\partial p}{\partial x} + F_x - V_x \qquad (5.6b)$$

$$\frac{\partial v}{\partial t} + \frac{1}{\Omega}\left(u\Sigma_x\frac{\partial v}{\partial x} + v\Sigma_y\frac{\partial v}{\partial y}\right) = -\frac{1}{\rho}\frac{\partial p}{\partial y} + F_y - V_y \qquad (5.6c)$$

The meaning of symbols is as follows: Ω and (Σ_x,Σ_y) are the volume fraction and the area fractions, hence dimensionless, open to flow in the *x*, and *y* directions respectively, ρ is the density, *c* is the sound speed, (u,v) are the components of the velocity vector *v, t* is the physical time as before, (F_x,F_y) are the external forces per unit mass (i.e., the acceleration of gravity components), *p* is the pressure, (V_x,V_y) are the viscous accelerations, next expressed in the general form:

$$V_x = -\frac{1}{\rho\Omega}\left[\frac{\partial(1-\Sigma_y)\tau_{w,xy}}{\partial y} + \frac{\partial(\Sigma_x\sigma_x)}{\partial x} + \frac{\partial(\Sigma_y\tau_{xy})}{\partial y}\right] \qquad (5.7a)$$

$$V_y = -\frac{1}{\rho\Omega}\left[\frac{\partial(1-\Sigma_x)\tau_{w,xy}}{\partial x} + \frac{\partial(\Sigma_x\tau_{xy})}{\partial x} + \frac{\partial(\Sigma_y\sigma_y)}{\partial y}\right] \qquad (5.7b)$$

The terms $\tau_{w,ij}$, i≠j, are the wall shear stresses which vanish when Σ_i=1. They are explicitly computed on the basis of the local velocity field, assuming a zero velocity value at the wall (non slip condition). The generic stress term τ_{ij} is explicated in the next section.
The mathematical model expressed by Eqs. 5.6a-5.6c was tested for three-dimensional fluid motion problems, see Fiorentino et al., 2017 for further details.

In this case, the relationship between stresses and strains is next expressed for Newtonian fluids:

$$\sigma_x = -2\mu\frac{\partial u}{\partial x} - \frac{1}{3}\underline{\nabla}\cdot\underline{v} \tag{5.8a}$$

$$\sigma_y = -2\mu\frac{\partial v}{\partial y} - \frac{1}{3}\underline{\nabla}\cdot\underline{v} \tag{5.8b}$$

$$\sigma_z = -2\mu\frac{\partial w}{\partial z} - \frac{1}{3}\underline{\nabla}\cdot\underline{v} \tag{5.8c}$$

$$\tau_{xy} = -\mu\left(\frac{\partial v}{\partial x} + \frac{\partial u}{\partial y}\right) \tag{5.8d}$$

$$\tau_{xz} = -\mu\left(\frac{\partial w}{\partial x} + \frac{\partial u}{\partial z}\right) \tag{5.8e}$$

$$\tau_{yz} = -\mu\left(\frac{\partial v}{\partial z} + \frac{\partial w}{\partial z}\right) \tag{5.8f}$$

while for non-Newtonians, the generalized Carreau (Pritchard et al., 2015) model is adopted.

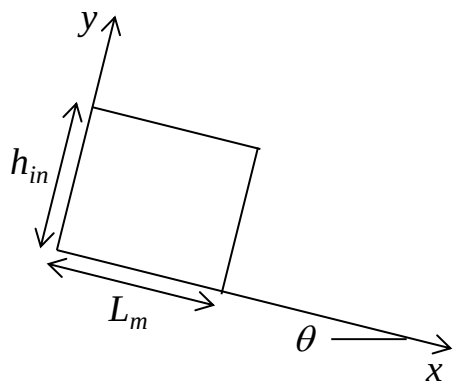

Figure 5.1 Channel and initial mass geometry (Rendina et al., 2017).

5.1.1. The numerical solvers

The equations (5.1a) and (5.1b) are hyperbolic partial differential equations and their solution calls for the application of a numerical method. A finite volume method was analyzed, in particular the Lax-Friedrichs scheme that is a central of the first-order (Friedrichs and Lax, 1971).
The considered domain ranges from *0* to *L* along *x* and from *0* to t_{end} along *t*, is discretized with a grid of points (i,j) spaced of Δx along *x* and Δt along *t* (Fig. 5.2). Being the scheme of Lax-Friedrichs explicit, the system state at the subsequent time depends solely on the system state at the current time.

The equations (5.1a) and (5.1b) can be rewritten as follow:

$$\frac{h_i^{j+1}u_i^{j+1}-0.5\left(h_{i+1}^j u_{i+1}^j+h_{i-1}^j u_{i-1}^j\right)}{\Delta t}+\frac{0.5g\cos\theta\left(h_{i+1}^j\right)^2+h_{i+1}^j\left(u_{i+1}^j\right)^2}{2\Delta x}+$$
$$-\frac{0.5g\cos\theta\left(h_{i-1}^j\right)^2+h_{i-1}^j\left(u_{i-1}^j\right)^2}{2\Delta x}=gh_i^j\sin\theta-gh_i^j S_{fi}^j\frac{u_i^j}{\left|u_i^j\right|} \quad (5.9a)$$

$$\frac{h_i^{j+1}-0.5\left(h_{i+1}^j+h_{i-1}^j\right)}{\Delta t}+\frac{h_{i+1}^j u_{i+1}^j-h_{i-1}^j u_{i-1}^j}{2\Delta x}=0 \quad (5.9b)$$

To make the system of equation stable the Courant Friedrichs-Lewy or CFL condition was imposed (Courant et al., 1928):

$$c\,\frac{\Delta t}{\Delta x}\leq 1 \quad (5.10)$$

being *c* the local wave velocity.

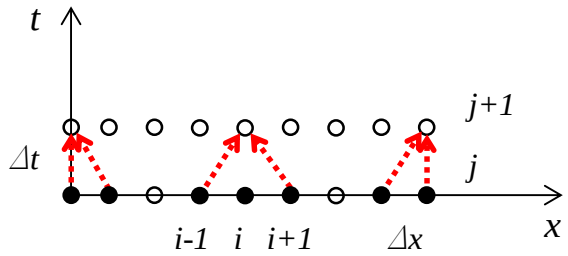

Figure 5.2 Lax-Friedrichs scheme (Rendina et al., 2017).

-2D mathematical model

Navier Stokes Eqs. (5.6a)-(5.6c) are solved in a Eulerian framework with a Finite Volume Method (FVM) in conjunction with the Volume of Fluid (VoF) method. VoF is a free-surface numerical technique for tracking and locating free surfaces. It belongs to the class of Eulerian methods which are characterized by a computing mesh either stationary or integral to the moving domain to accommodate the evolving shape of the interfaces. Velocity and pressure fields are coupled by using the time-advanced velocities in the continuity equations and time-advanced pressures in the momentum equations. The 2D model has been widely validated over the years particularly in connection with wave propagation, see for instance Viccione 2016.

5.2 TEST CASES

For numerical analysis the channel geometry with L=1 km, Δx=0.1 m and θ = 0, 10, 20, 30 and 40°; the mass geometry with L_m=10 m and h_{in} = 1, 5 or 10 m were considered.
The initial conditions are $u(x,0)=0$, $h_{in}(x,0)=1$, 5 or 10 m and $S_f(x,0)=0$ for $0 \leq x \leq L_m$.

Temporal evolution of $h(x,t)$, $u(x,t)$ and $S_f(x,t)$ are obtained by solving the system of equations (5.1a), (5.1b) and (5.2a) for Newtonian analysis and (5.1a), (5.1b) and (5.2b) for Cross-Bingham analysis (Rendina et al., 2017).

5.2.1 Newtonian flow analysis

A 1D dam break problem of water flowing over an horizontal bottom with h_{in}=10 m was simulated with the FV model and the Flow-3D model. Results were compared with the analytical solution of Stoker, see Stoker (1957) and Guinot (2003). The Figures 5.3 and 5.4 show the height, the velocity and the Froude number for t^*=0.03 and 0.05, where t^* is the dimensionless time defined as $t/\sqrt{g h_{in}}$. It is possible to observe a good agreement between the FV model, Flow-3D and the analytical solution (Rendina et al., 2017).

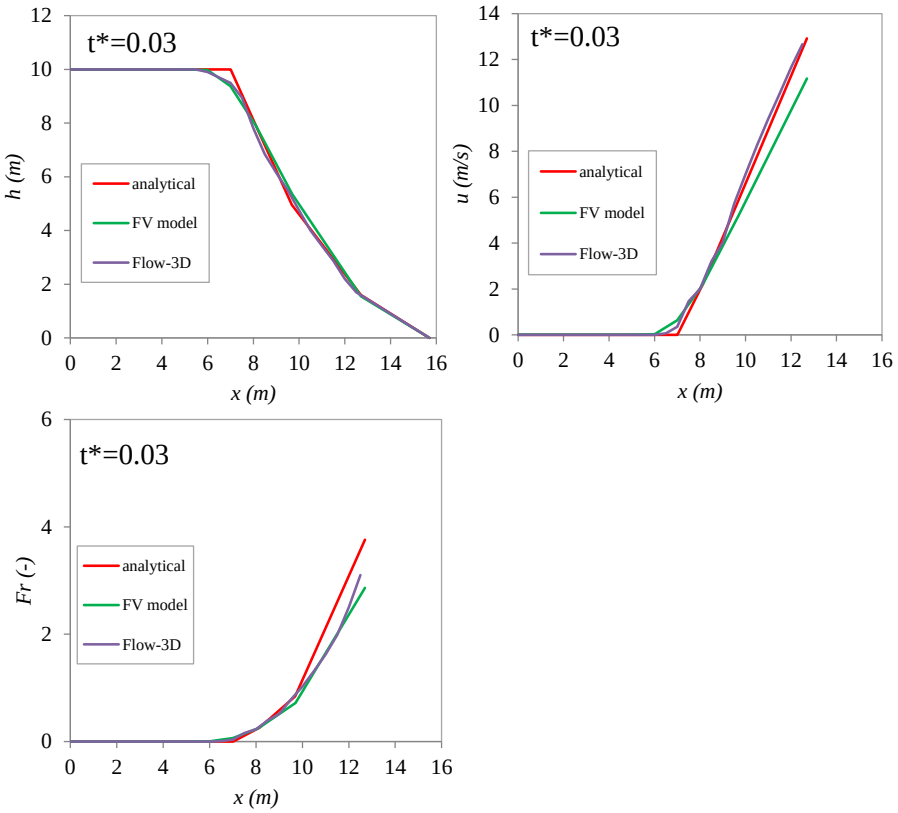

Figure 5.3 Height, velocity and Froude number of a water flow at *t=0.03 (Rendina et al., 2017).**

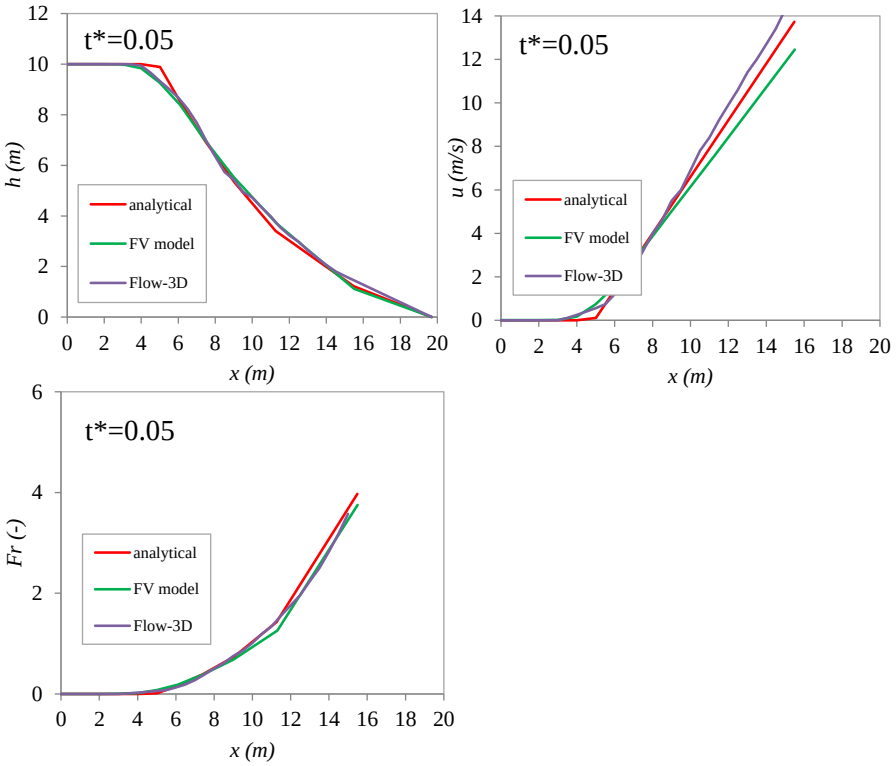

Figure 5.4 Height, velocity and Froude number of a water flow at *t=0.05 (Rendina et al., 2017).**

The Newtonian rheological model was used and a large number of numerical simulations was performed with the FV model, changing the mass and channel geometry (see section 5.2) and the dimensionless roughness index *m'* evaluated as m/m_{max}, with $0.5 \le m \le m_{max}=1.5$ $m^{1/2}$. The Froude number of the flow front at the dimensionless axial coordinate *x'* defined as $(x-L_m)/L$ was evaluated and the results show a subcritical flow only for the horizontal channel and h_{in} equal to 1m (Fig. 5.5) (Rendina et al., 2017).

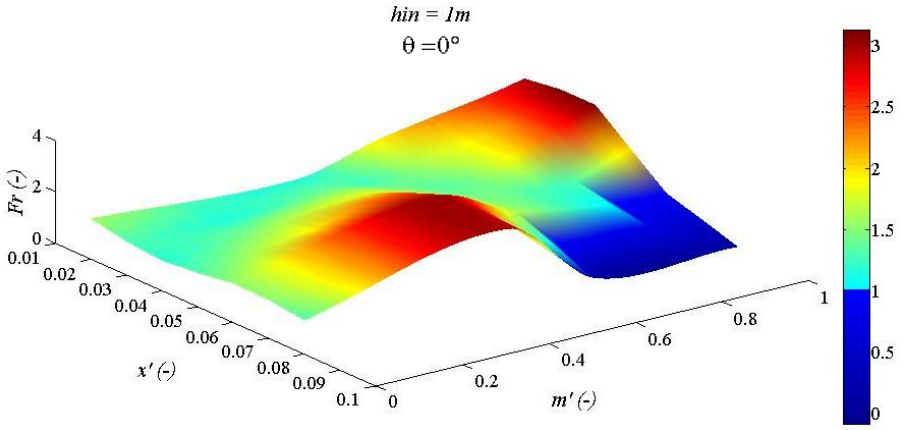

Figure 5.5 Froude numbers computed by FV model of a water flow on an horizontal channel with h_{in}=1m for different dimensionless roughness index of the flow (Rendina et al., 2017).

5.2.2 Cross-Bingham flow analysis

The Cross-Bingham rheological law, previously validated by Lanzini, 2012, was implemented to simulate 1D non-Newtonian flows. The rheological parameters were taken from Lanzini 2012, while the dynamic viscosity "μ" has been changed from 0.1 to 500 Pa s referring to Pastor et al., 2007. Particularly, according to Lanzini, 2012 it was assumed: i) ρ=1300 kg m^{-3} ii) C_v = 0.7; iii) a =1 and β =1 and iv) n_m=0.05 s m$^{-1/3}$. The Froude number of the flow front was evaluated with FV model and the results are listed in Tables 5.1, 5.2, and 5.3 and are shown in Figures 5.6, 5.7 and 5.8 for h_{in}=10m, h_{in}=5m and h_{in}=1m respectively. The dynamic viscosity is expressed in terms of the dimensionless parameter μ', defined as μ/μ_0, where μ_0 is the water viscosity. In particular, the dimensionless viscosities sequence μ_1'=100, μ_2'=500, μ_3'=10^4, μ_4'=10^5 and μ_5'=5×10^5 has been considered. The Figures 5.6 and 5.7 reveal mainly supercritical flows for channel slope θ >0°. This evidence does not occur in the cases with initial height h_{in}=1m, where the flows are subcritical for the channel slope up to 40° (Fig. 5.8).

At a given dynamic viscosity defined as the dimensionless parameter μ', the Froude number along the dimensionless axial coordinate x', increases

with increasing of the channel slope; but for a given inclination angle it decreases as the initial heights of the flow decrease.
Keeping x' fixed, it is possible to observe for lower dimensionless viscosities that the Froude number sharply increases with the increase of the dynamic viscosity then a decreasing occurs: a relative maximum then appears.
Figure 5.9 shows the relative relevance of the numerator and the denominator appearing in the Froude number the higher is the discrepancy between the corresponding lines the higher is the Froude number. As can be observed, subcritical condition only for the case of horizontal channel and initial height h_{in}=1m exists. Considering only the first term in RHS of equation (5.2b) and the rheological parameters used in previous numerical analysis, the Froude number was computed by Flow-3D. The comparison of the Froude numbers computed by the FV and the Flow-3D models for following cases: h_{in}=10, 5 and 1 m; θ=0° and 40°; μ'_1=100 and μ'_5=5×105; are shown in Figure 5.10. The Froude numbers are compared at the axial coordinates x'=0.10, 0.20, 0.30 and 0.40 for h_{in}=10m; x'=0.10, 0.20 for h_{in}=5m and x'=0.01 and 0.03 for h_{in}=1m. For all analyzed cases, the points are located close to the 1:1 line in the plots of Figure 5.10 and the linear regressions are characterized by correlation coefficients (R^2) equal to 0.9890 and 0.9919 (Rendina et al., 2017).

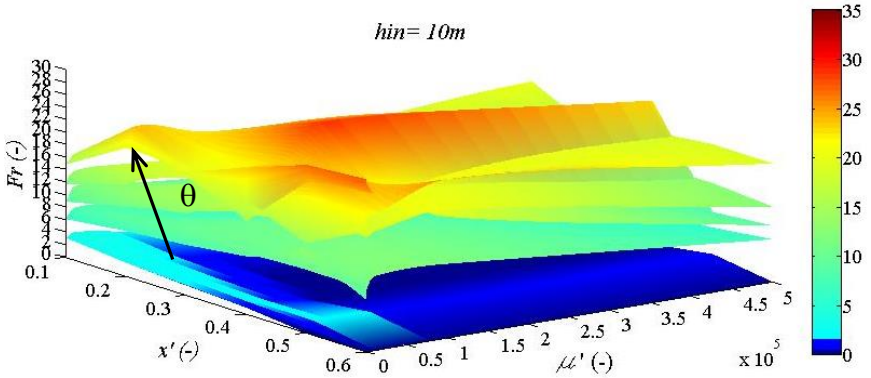

Figure 5.6 Froude numbers of the flows computed by FV model with h_{in}=10m for different channel slope and dimensionless dynamic viscosity of the flow (Rendina et al., 2017).

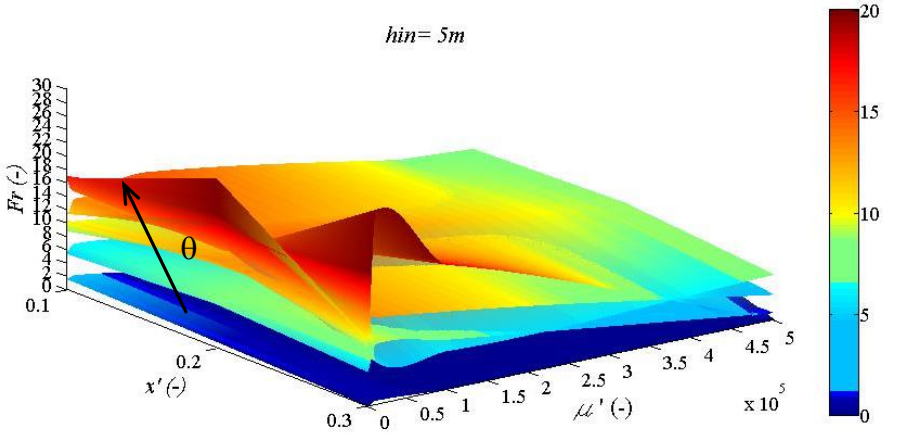

Figure 5.7 Froude numbers of the flows computed by FV model with h_{in}=5m for different channel slope and dimensionless dynamic viscosity of the flow (Rendina et al., 2017).

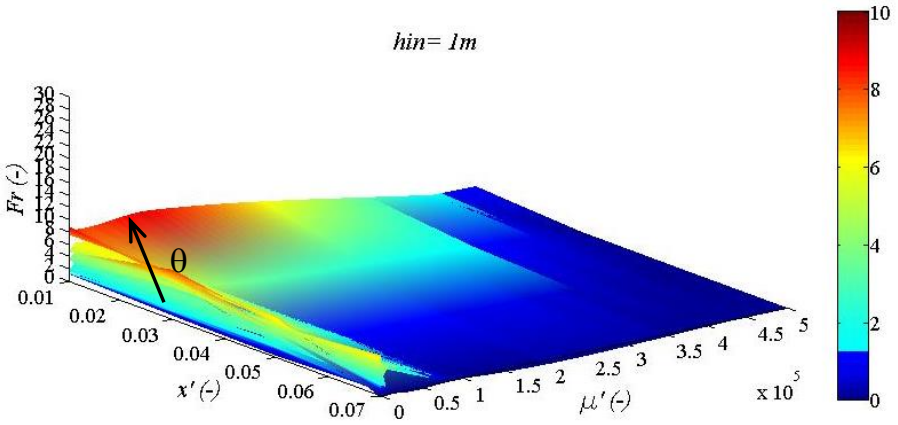

Figure 5.8 Froude numbers of the flows computed by FV model with h_{in}=1m for different channel slope and dimensionless dynamic viscosity of the flow (Rendina et al., 2017).

Table 5.1 List of analyzed cases for viscoplastic flows with h_{in}=10 m; in bold the corresponding Froude numbers computed by FV model (Rendina et al., 2017).

h_{in}=10 m		μ'_1=100	μ'_2=500	μ'_3=10^4	μ'_4=10^5	μ'_5=5×10^5
θ=0°	x'=0.10	3.1904	3.1162	3.767	2.048	0.473
	x'=0.20	2.1735	2.1961	2.8706	1.0701	0.2821
	x'=0.30	1.5692	1.6828	2.2061	0.5481	0
	x'=0.40	1.0406	1.0898	1.7756	0.3041	0
	x'=0.50	0	0	1.6275	1.5478	1.4466
	x'=0.60	0	0	0	0	0
θ=10°	x'=0.10	6.111	6.1547	7.658	6.4466	2.7439
	x'=0.20	7.2336	7.3557	8.8557	7.3341	4.1758
	x'=0.30	8.0245	8.4617	10.0571	9.8649	6.2998
	x'=0.40	9.2228	9.7996	10.2838	11.0245	4.9531
	x'=0.50	13.5515	10.0739	11.3639	11.5699	5.6656
	x'=0.60	8.2928	9.987	11.8344	11.8224	6.812
θ=20°	x'=0.10	8.9501	8.8724	11.0266	9.8006	4.3467
	x'=0.20	11.4193	11.0837	13.418	12.6264	8.2696
	x'=0.30	13.0507	13.3626	15.026	16.6913	11.8035
	x'=0.40	17.9601	16.2895	16.9324	18.5016	12.6166
	x'=0.50	14.3779	18.8523	16.4235	20.4216	12.7631
	x'=0.60	19.1859	18.2971	19.0291	20.5345	12.0014
θ=30°	x'=0.10	11.6823	11.9425	13.4934	12.7332	8.8259
	x'=0.20	14.6181	15.5279	17.6065	16.8103	19.908
	x'=0.30	20.6361	18.7499	19.4217	19.2389	15.1911
	x'=0.40	17.4981	15.7207	22.7726	22.2324	17.9529
	x'=0.50	17.1207	18.2716	25.4093	21.0493	18.9635
	x'=0.60	19.1324	21.1823	21.7375	25.3371	18.8882
θ=40°	x'=0.10	15.1666	14.8168	16.2504	16.3915	11.6595
	x'=0.20	20.879	20.4398	23.6499	20.782	16.8088
	x'=0.30	19.6676	20.2046	20.0462	24.6985	18.7161
	x'=0.40	23.3235	14.9333	19.6558	28.5509	22.9167
	x'=0.50	26.8256	24.5805	24.1183	21.3966	8.1504
	x'=0.60	27.5438	26.9685	24.9786	19.3247	8.9843

Table 5.2 List of analyzed cases for viscoplastic flows with h_{in}=5 m; in bold the corresponding Froude numbers computed by FV model (Rendina et al., 2017).

h_{in}=5 m		μ'_1=100	μ'_2=500	μ'_3=10^4	μ'_4=10^5	μ'_5=5×10^5
θ=0°	x'=0.10	1.678	1.4704	1.7741	0.3854	0.4403
	x'=0.20	0.8211	0.8357	0.9526	0	0
	x'=0.30	0	0	0.5405	0	0
θ=10°	x'=0.10	5.2788	5.4031	6.4855	5.1977	0.9923
	x'=0.20	6.4216	6.7733	7.7426	6.987	0.346
	x'=0.30	5.0889	5.1354	8.9591	7.3624	0.9524
θ=20°	x'=0.10	8.6371	10.0766	9.8429	8.782	4.7863
	x'=0.20	13.3945	12.346	12.9375	12.0212	6.3089
	x'=0.30	8.8019	12.9254	13.0028	11.5679	3.6923
θ=30°	x'=0.10	11.5333	11.2004	13.2129	11.3203	7.9689
	x'=0.20	18.8236	18.3028	14.6256	14.2827	8.7276
	x'=0.30	16.3586	16.2827	6.3539	5.6926	6.6866
θ=40°	x'=0.10	16.5593	16.8808	14.3443	14.8623	6.7303
	x'=0.20	25.2558	21.6295	14.1297	12.8569	7.4506
	x'=0.30	9.993	10.2406	28.8364	18.4932	0

Table 5.3 List of analyzed cases for viscoplastic flows with h_{in}=1 m; in bold the corresponding Froude numbers computed by FV model (Rendina et al., 2017).

h_{in}=1 m		μ'_1=100	μ'_2=500	μ'_3=10^4	μ'_4=10^5	μ'_5=5×10^5
θ=0°	x'=0.01	1.4393	1.1523	0.6486	0.1075	0.0439
	x'=0.03	2.3488	0.6297	0.5501	0.0407	0.0723
	x'=0.05	2.5971	0.3674	0.2753	0.07	0
	x'=0.07	0.7369	0.8125	0	0	0
θ=10°	x'=0.01	2.4234	1.6079	3.4607	2.1433	1.1593
	x'=0.03	2.277	1.8745	3.4939	1.2684	0.0732
	x'=0.05	4.0831	2.9001	3.213	0.323	0
	x'=0.07	6.1231	5.3946	3.9598	0	0
θ=20°	x'=0.01	3.3692	3.5822	4.3666	1.7717	0.0626
	x'=0.03	5.491	5.1783	4.9647	1.0866	0.0653
	x'=0.05	5.374	5.4618	3.1182	0.7044	0
	x'=0.07	4.0991	3.0855	4.478	0	0
θ=30°	x'=0.01	4.8241	4.944	6.0598	3.5353	0.0572
	x'=0.03	8.0795	6.3745	6.1288	1.8943	0.0691
	x'=0.05	5.1465	6.6704	4.8752	0.9027	0
	x'=0.07	6.6042	0	0	0	0
θ=40°	x'=0.01	8.943	7.5126	8.1459	8.6758	0.0636

	x'=0.03	6.167	7.633	5.3336	3.4002	0.0748
	x'=0.05	3.8627	4.397	0.65	1.2453	0
	x'=0.07	0.1886	3.9286	0.2046	0.1043	0

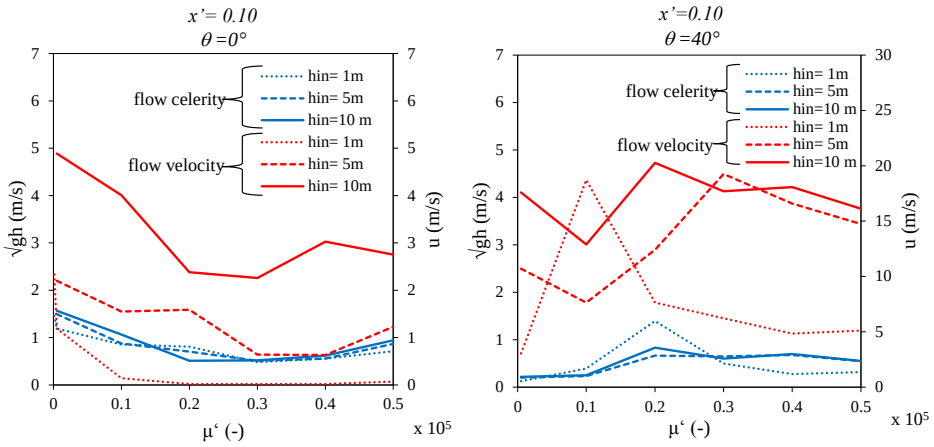

Figure 5.9 Trend of numerator and denominator of the Froude numbers computed by FV model for different dimensionless dynamic viscosities of the flow (Rendina et al., 2017).

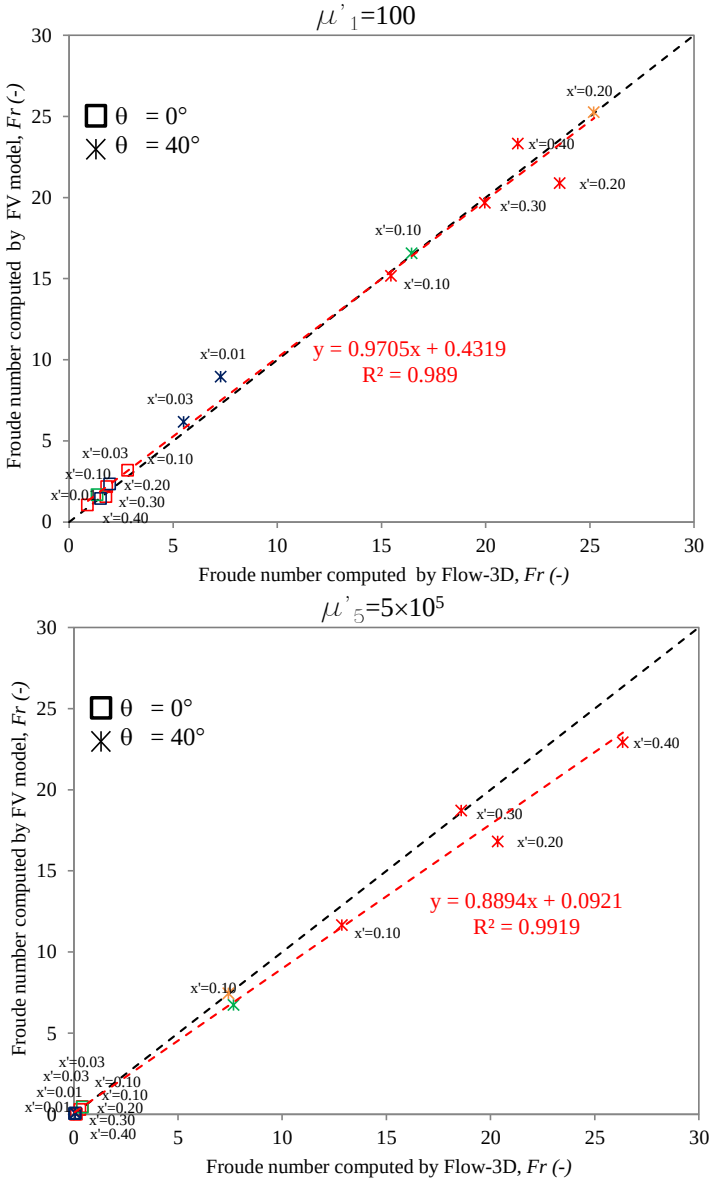

Figure 5.10 Comparison of the Froude numbers computed by FV model and Flow-3D model for two different dimensionless dynamic viscosities of the flow. The legend refers to different channel slope and the colors refer to the different

initial height of the flow. The h_{in}=10m is represented in red, the h_{in}=5m in green and h_{in}=1m in blue (Rendina et al., 2017).

5.3 DISCUSSION

The numerical results consisting of flow heights and velocities computed by FV model are summarized in Figures 5.11 and 5.12 at the cross-sections identified by the dimensionless coordinates x'=0.05 and 0.10 respectively. Equipotential Froude curves are sketched with black continuous lines from Fr=1 to Fr=25. Numerical results are grouped for increasing dimensionless viscosities considering the sequence μ_1'=100, μ_2'=500, μ_3'=10^4, μ_4'=10^5 and μ_5'=5×10^5. It can be observed that the Froude number is not monotonic with μ' and, for x'=0.05 and x'=0.10 two sub-regions can be identified: a first one in which Fr increases as μ' gets higher a subsequent second region in which the opposite behavior is given. This can be explained on the fact that, when the dimensionless viscosity increases, the flow profile passes from condition 1 to condition 2 as depicted in Figure 5.13. More specifically the Froude number increases because at cross-section investigated the flow height is lower and the velocity is higher respect to condition 1. Therefore, it is possible to identify a critical value $\overline{\mu'}$ for the dimensionless viscosity. For $\mu'>\overline{\mu'}$ a decrease of Fr is then observed as depicted by the condition 3 in the Figure 5.13 in which an yielded region is formed. In Table 5.4 the Percent Variation of flow height *PV(h)*, velocity *PV(u)* and Froude number *PV(Fr)* are given in terms of h_{in}=10m, channel slope varying from θ=0° to θ=40° and dimensionless dynamic viscosity ranging from μ_1'=100 to μ_5'=5×10^5. The Percent Variations *PV(h)*, *PV(u)* and *PV(Fr)* are evaluated as follows:

$$PV(h) = \frac{h|_{x'=0.10} - h|_{x'=0.05}}{h|_{x'=0.05}} \tag{5.11}$$

$$PV(u) = \frac{u|_{x'=0.10} - u|_{x'=0.05}}{u|_{x'=0.05}} \tag{5.12}$$

$$PV(Fr) = \frac{Fr|_{x'=0.10} - Fr|_{x'=0.05}}{Fr|_{x'=0.05}} \tag{5.13}$$

The *PV* highlights the variability of Froude number that clearly depends on the temporal-spatial evolution of the propagation of height and velocity. In general this number increases downstream, reaching increments greater than 100% or more, as indicated by cells with asterisk in Table 5.4, a condition typically observed for μ>105. When the channel is horizontal the Froude number decreases downstream for all considered viscosities.

This topic is very complex and certainly deserves in-depth research; however these preliminary analysis highlighted the following aspects: i) the higher is the channel slope, the higher is the Froude number as can be perceived; ii) the higher is the initial height of the flow, the higher is the Froude number; iii) the Froude number sharply increases with the increase of the dynamic viscosity then decreases for greater values; iv) the Froude number of water flows is always greater than the corresponding given by a viscoplastic flow.

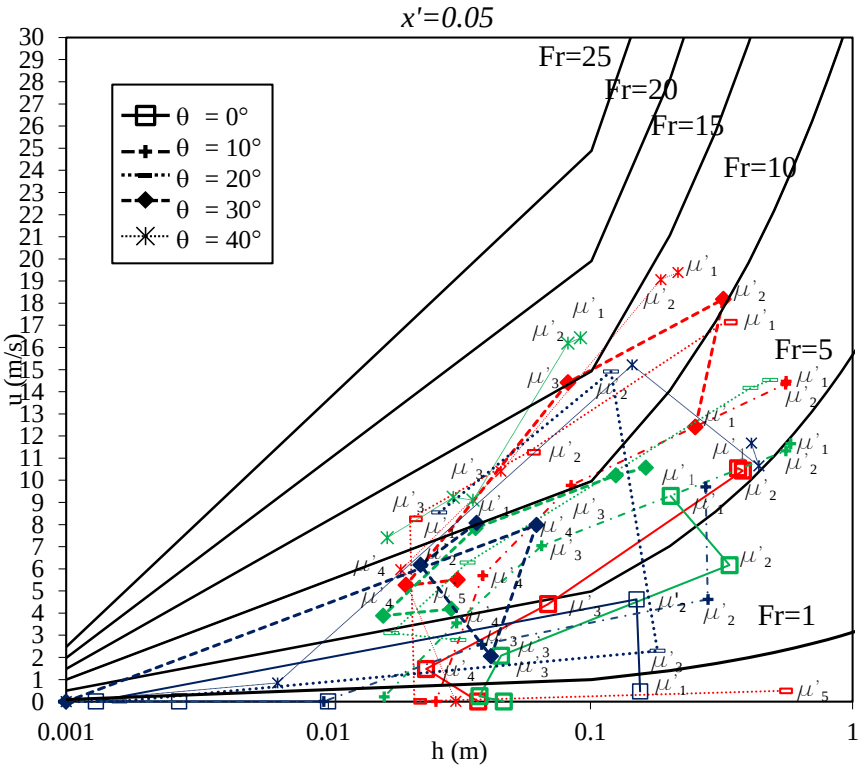

Figure 5.11 Flow height and velocity computed by FV model in a section x'=0.05 for different dynamic viscosity of the flow and channel slope. The colors refer to the different initial height of the flow. The h_{in}=10m is represented in red, the h_{in}=5m in green and h_{in}=1m in blue (Rendina et al., 2017).

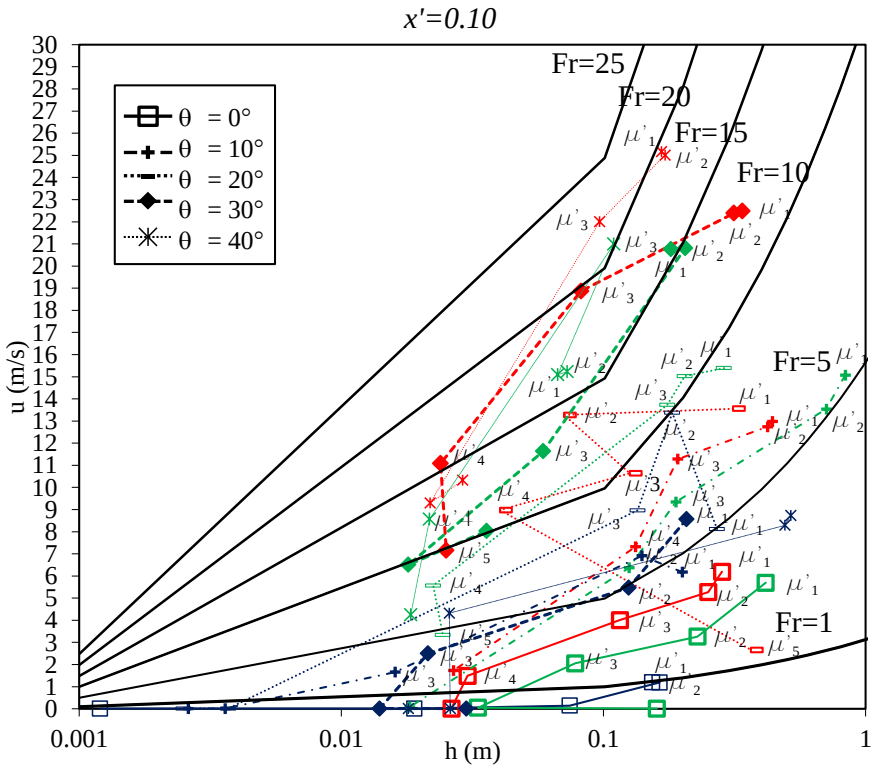

Figure 5.12 Flow height and velocity computed by FV model in a section x'=0.10 for different dynamic viscosity of the flow and channel slope. The colors refer to the different initial height of the flow. The h_{in}=10m is represented in red, the h_{in}=5m in green and h_{in}=1m in blue (Rendina et al., 2017).

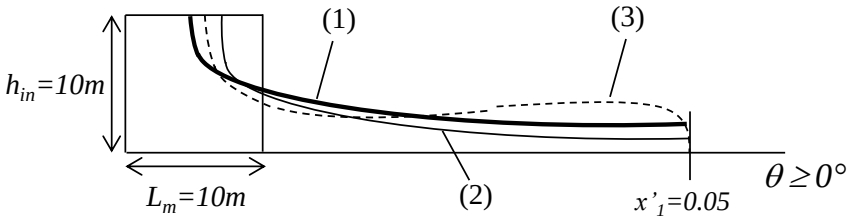

Figure 5.13 Flow heights at a generic cross-section (x'_1) for increasing dimensionless viscosities. The condition (1) corresponds to flow height with

lower viscosity, while the condition (3) corresponds to flow height with higher viscosity (Rendina et al., 2017).

Table 5.4 Percent Variation *(PV)* of flow height *(PV(h))*, velocity *(PV(u)* and Froude number *(PV(Fr))* in the sections x^*=0.05 and x^*=0.10 (Rendina et al., 2017).

h_{in} =10 m				
θ (°)	μ' (-)	*PV(h) (%)*	*PV(u) (%)*	*PV(Fr) (%)*
0	100	-23	-41	-33
	500	-34	-49	-38
	10^3	+68	-9	-30
	10^4	+28	+1	-11
	50^4	-29	-19	-16
10	100	-21	-10	+1
	500	-24	-11	+2
	10^3	*	+15	-23
	10^4	*	+29	-30
	50^4	+4	*	*
20	100	-31	-21	-5
	500	-4	+18	+20
	10^3	+22	+29	+16
	10^4	*	*	*
	50^4	+89	*	*
30	100	+35	+81	+56
	500	-2	+23	+24
	10^3	0	+31	+31
	10^4	+21	*	+92
	50^4	-19	+30	+45
40	100	-23	+30	+48
	500	-7	+31	+36
	10^3	*	*	+45
	10^4	+15	+56	+45
	50^4	-5	*	*

* Percent variations greater than +100%.

6 KINEMATIC CHARACTERISTICS OF NEWTONIAN AND FRICTIONAL FLOWS THROUGH SPH-FDM MODEL

Few studies in the scientific literature discuss the kinematic regime of hyperconcentrated flows and mudflows; whereas, some papers focus on the kinematic characteristics of granular flows exist (see Chapter 4). However, these studies do not relate the flow regime (subcritical, critical and supercritical) to rheological properties of the flowing mass (e.g. flow density, frictional angle, pore water pressures etc.).

This Chapter provides a contribution to this topic through the use of an enhanced numerical model developed by Pastor et al., 2015a, which combines a 3D depth-integrated hydro-mechanical coupled SPH (Smooth Particles Hydrodynamics) model for the propagation analysis and a 1D vertical FDM (Finite Difference Method) model for the evaluation of the pore water pressure along the height of the flowing mass. The SPH-FDM model is initially used to simulate, in 2D and 3D analyses, well-documented flume tests performed in USA in a 90 m long channel exiting at a sub-horizontal pad. Once the model has been validated, it is later used to estimate the regime of non-Newtonian flows in an open channel (Cascini et al. 2016a,b).

6.1 SPH-FDM MODEL

The model was proposed by Pastor et al. (2015a), and is a combination of a 3D depth-integrated hydro-mechanical coupled SPH model incorporating the propagation equations, and a 1D vertical FDM model describing the evolution of pore pressure along each vertical of the flowing deformable mass (Cascini et al., 2016a,b).
The 3D depth-integrated hydromechanical-coupled sub-model solves the propagation equations, which are: balance of mass of the mixture (solid

particles and interstitial fluid) and balance of linear momentum of the mixture (Eqs. 6.1 and 6.2).

$$\frac{\bar{d}h}{dt} + h\, div\, \bar{u} = e_R \tag{6.1}$$

$$\rho\, h\, \frac{\bar{d}\bar{u}}{dt} = \frac{1}{2}\, grad\,(\rho h^2 g) + \tau_b + \rho h b - \rho\, \bar{u}\, e_R \tag{6.2}$$

where: h is the flow height, $\bar{u}$ the flow velocity, e_R is the erosion rate (Hungr, 1995), ρ the flow density, t the time, b the body forces (i.e. gravity forces), g the gravity acceleration, and τ_b the resistance at the bottom.

The overbars denote depth-integrated magnitudes:

$$\bar{\phi} = \frac{1}{h} \int_z^{z+h} \phi\,(x_3)\, dx_3 \tag{6.3}$$

the time derivate represents

$$\frac{\bar{d}}{dt} = \frac{\partial}{\partial t} + \bar{u}_j \frac{\partial}{\partial x_j} \tag{6.4}$$

With j= 1, 2 and 3

The governing equations are set in a "quasi-Lagrangian" or "Lagrangian–Eulerian". It is difficult to obtain a Lagrangian form of the depth integrated equations, because the vertical integration is not performed in a material volume, so Pastor et al. (2009) found convenient to refer to an equivalent 2D continuum having the depth-integrated velocities as the velocities of their material points (Eq. 6.3). This cannot be considered as a Lagrangian formulation, because the moving points have not exact connection with material particles. Indeed, a moving point in the depth-integrated model represents a column of material extending from the bottom to the free surface (Pastor et al., 2009). The column travels with the depth-averaged velocity, and therefore, fluid particles travelling faster will enter it whereas fluid particles with a smaller velocity will be left

behind (Pastor et al., 2009). The Equation 6.4 it is used to derive a quasi-Lagrangian formulation of the depth-integrated equations.
The flowing mass is schematized as a continuum body, and it is discretized in a set of so-called "particles", which are used as integration points. The main advantage of this numerical technique is that the detail of the Digital Terrain Model (DTM) is completely independent on the number of particles used to discretize the flowing mass. A DTM often consists in millions of points, from one to few meters spaced in a regular grid of squares (Fig. 6.1), while number of the SPH "particles" usually range from hundreds to few thousands (Cascini et al., 2016a,b). This corresponds to a very efficient numerical tool, which guarantees very short computational times compared to other Eulerian FDM models, e.g. Flow-2D (O'Brien et al., 1993), FEM_GeoFlow (Pastor et al., 2002). Since many flow-like landslides have small average depths (also named, propagation soil height or propagation height) in comparison with their length or width, the above equations can be integrated along the vertical axis and the resulting 2D depth-integrated model offers an excellent combination of accuracy and simplicity. Thus, the model is 2D as it concerns its mathematical formulation, while it is 3D in its general output, which include the spatial location (X_1, X_2 in Fig. 6.1) of the deformable propagating mass and the propagation height (X_3, in Fig. 6.1) at each point of the mass (Cascini et al., 2016a,b).

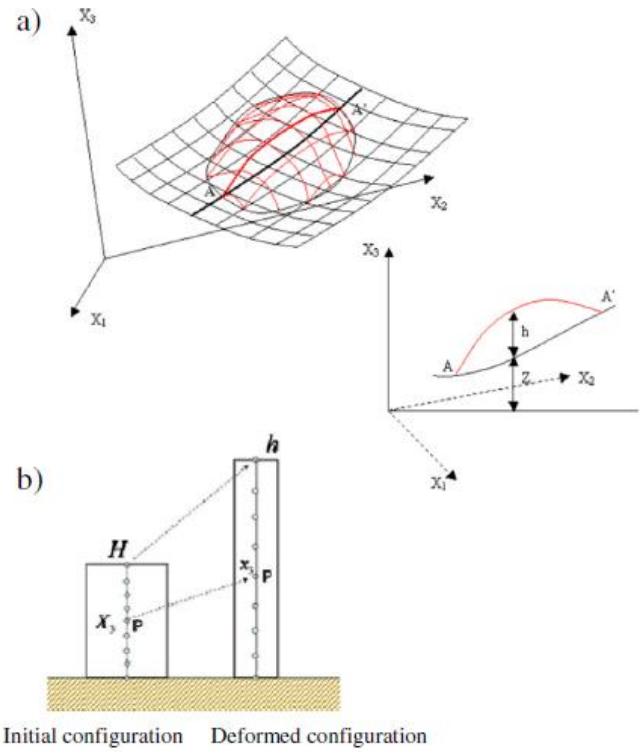

Figure 6.1 a) Schematic of a Digital Terrain Model (DTM), in black, over which a landslide mass is propagation, in red, (Pastor et al., 2014); b) initial and deformed configuration of a column of the landslide mass (Pastor et al., 2015a).

Firstly proposed by Pastor et al. (2009) for application to flow-like landslides, this model has been extensively applied so far, either for channelized flows, i.e. debris flows (Cascini et al., 2014) and unchannelized landslides, such as debris avalanches (Cuomo et al.,2014, 2016). In this version of the model, called in the scientific literature "SPH model", the vertical distribution of pore water pressure is approximated using a quarter cosinus shape function, with a zero value at the surface and zero gradient at the basal surface (Pastor et al., 2009). As parabolic problems dissipate faster shortwave lengths, any smooth

function having as boundary conditions zero at the top and zero derivative at the bottom will evolve towards the quarter cosinus. This approach can be viewed as approximating the pore pressure by a set of shape functions of harmonic type. If we denote the height by *h*, the longest wavelength in the solution will be *4h*, followed by *4h/3*, *4h/5* and so on. Then, from the limitation to a single Fourier component, the time-evolution of pore water pressure is given by Equation 6.5 (Cascini et al., 2016a,b):

$$\frac{dP_b}{dt} = \frac{c_v \pi^2}{4h^2} P_b \tag{6.5}$$

where P_b is the basal pore water pressure, c_v is the consolidation coefficient and h is the propagation height.

A recent enhancement for pore water pressures evaluation was proposed by Pastor et al. 2015a through the model named "SPH-FDM model", which includes a Finite Difference Method (FDM) model for the 1D equation of vertical consolidation (X_3 and x_3, in Fig. 6.1 a, b). Starting from Biot-Zienkiewicz model, Pastor et al. (2015a) consider the landslide mass constituted by a set of differential volumes to solve the consolidation equation in the deformed configuration at time *t*. The Figure 6.1 b shows a schematic of a deformable mixture column, discretized along the vertical axis, moving and deforming during the propagation stage (Cascini et al., 2016a,b).

The equation describing the evolution of pore pressure (P_w) along x_3, which is the vertical axis, can be written as follows:

$$\frac{dP_w}{dt} = \rho g \frac{dh}{dt}\left(1 - \frac{x_g}{h}\right) + \frac{K_v}{\alpha} d_{v0} + k_w \frac{K_v}{\alpha} \frac{\partial^2 P_w}{\partial x_g^2} \tag{6.6}$$

where K_v is the elastic volumetric stiffness ratio, a is the constitutive coefficient - Pastor et al. (2015a,b) assume elastic behaviour and oedometric state of deformation - K_v/a is the oedometricmodulus, d_{v0} is the volumetric component of the rate of deformation tensor and kw is the permeability. It is worth noting that the term k_w K_v/α is the consolidation coefficient (usually labelled as "c_v").

The vertical variation of pore water pressures can be analyzed incorporating, at each SPH particle, a 1D finite difference vertical mesh and: i) an initial condition and ii) boundary conditions at the surface and

the bottom (for instance, zero at the surface and zero flow at the bottom).
This mathematical framework allows taking into account the time space evolution of the pore water pressures due to: i) variations of the height at each SPH particle, which depends on the flow velocity, local topography and soil stiffness, ii) the free-drainage boundary condition at the top of the flow, and iii) pore water pressures applied at the bottom of the flow (Cascini et al., 2016a,b).

6.1.1 Rheological models

The flow resistance term at the bottom of the propagating mass (τ_b) considers both a fluid phase and a solid phase (Naef et al., 2006).

As it concerns the mechanical behavior of the propagating mass, the frictional rheological model is an excellent approximation for coarse-grained soils and medium-sized debris (Equation 6.7) (see Section 2.3 and 2.4). It entails:

$$\tau_b = -\left((1-n)(\rho_s - \rho_w) g\, h - p_w^b\right) tg\phi_b\, sgn(\bar{u}) \tag{6.7}$$

where n is the soil porosity, ρ_s is the solid grain density, ρ_w is the water density, ϕ_b is the basal friction angle, p_w^b is the excess of pore water pressure to hydrostatic, sgn is the sign function and $\bar{u}$ is the depth-averaged flow velocity.

Furthermore, a Chezy-Manning model can be used to describe turbulent flows with small-sized debris or water flows (Equation 6.8).

$$\tau_b = -\frac{\rho g m^2}{h^{\frac{7}{3}}}\, sgn(\bar{u}) \tag{6.8}$$

where *m'* is the Manning coefficient that takes into account the turbulent and dispersive components of flow.

6.1.2 Numerical model

There are two steps to obtain a SPH formulation. The first step is to represent a function and its derivatives in continuous form as integral representation, through the evaluation of the smoothing kernel function and its derivatives. This step is usually termed as kernel approximation. The second step is usually referred to as particle approximation. In this step, the computational domain is first discretized through a set of particles in their initial spatial configuration representing the initial settings of the problem. After discretization, field variables on a particle are approximated by a summation of the values over the nearest neighbor particles (Liu and Liu, 2010).

The SPH method is based on the following equality:

$$\phi(x) = \int_{\Omega} \phi(x')\delta(x' - x)dx' \qquad (6.9)$$

where ϕ is a function of the position vector x $\delta(x)$ is the Dirac delta, that is defined as:

$$\delta(x) = \begin{cases} \infty, & x = 0 \\ 0, & |x| > 0 \end{cases} \qquad (6.10)$$

In the Equation (6.9) Ω is the volume of the integral that contains x (Liu and Liu, 2010). This equation (6.9) cannot be used for discrete numerical models, for this reason Pastor et al. (2009) replace the Delta function $\delta(x'- x)$ by a smoothing function W(x'-x, h) with a finite spatial dimension *h* (Pastor et al., 2009, Liu and Liu, 2010). The kernel approximation of $\phi(x)$ becomes:

$$\langle \phi(x) \rangle = \int_{\Omega} \phi(x')W(x' - x, h)dx' \qquad (6.11)$$

where h is the smoothing length defining the influence or support area of the smoothing function or kernel W. A smoothing function W should satisfy a number of conditions (Equations 6.12 to 6.15):

$$\lim_{h\to 0} W(x'-x,h) = \delta(x) \tag{6.12}$$

$$\int_{\Omega} W(x'-x,h)dx' = 1 \tag{6.13}$$

The smoothing function W is positive and has compact support (Equation 6.14):

$$W(x'-x,h) = 0 \quad if\ |x'-x| \geq kh \tag{6.14}$$

where k is a positive integer, usually equal to 2.

The function is a monotonically decreasing function of ξ:

$$\xi = \frac{|x'-x|}{h} \tag{6.15}$$

Finally, W is a symmetric function of (x'-x).

Several kernel have been proposed in the past: the Gaussian kernel, the cubic spline etc.
As it concerns, the integral representation of the derivatives can be obtained by the application of integral theorems and taking into account that kernels have compact support (Pastor et al., 2009).
The second step represents the SPH discretization through particles to which information concerning field variables and their derivatives are linked (Fig. 6.2). The Equation 6.11 can be rewritten as:

$$\langle \phi(x_I) \rangle_h = \sum_{J=1}^{N} \phi(x_J) W(x_J - x_I, h)\, \varpi_J \tag{6.16}$$

Where N is a set of nodes, the sub-index *'h'* denotes the discrete approximation and ω_J denotes the weights of the integration formula.

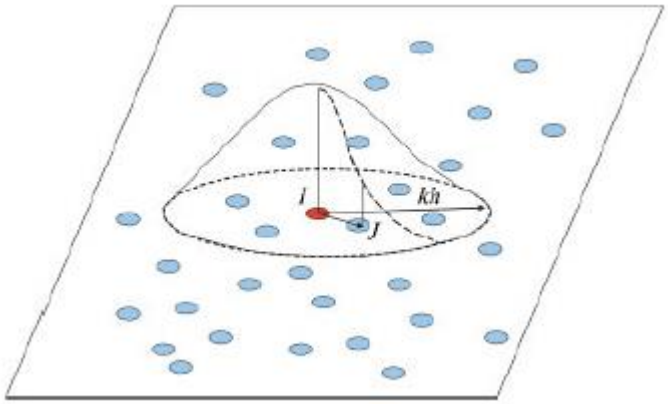

Figure 6.2 Numerical integration in a SPH model (Pastor et al., 2009).

The weight ω_J can be shown to be the volume Ω_J or the area associated with the node. In the context of continuum mechanics (solids and fluids), it is convenient to introduce the density ρ_J associated with node J as (Pastor et al., 2009):

$$\rho_J = \frac{m_J}{\Omega_J} \tag{6.17}$$

where m_J is the mass associated with node J or the mass of the volume associated with the considered node (Pastor et al., 2009).
In case we choose the function ϕ to represent the density, after substituting the Equation 6.16 becomes:

$$\rho_I = \sum_{J=1}^{N} W_{IJ} m_J \tag{6.18}$$

The techniques for deriving SPH formulations are shown in Liu and Liu (2010).
Following the procedure described above the balance of mass and linear momentum (Equations 6.1 and 6.2) can be rewritten as:

$$\frac{\bar{d}h_I}{dt} = h_I \sum_J \frac{m_J}{h_J} u_{IJ} gradW_{IJ} \tag{6.19}$$

$$\frac{\bar{d}}{dt}\bar{u}_I = -\sum_J m_J \left\langle \frac{P_I}{h_I^2} + \frac{P_I}{h_J^2} \right\rangle gradW_{IJ} + \frac{1}{\rho}\sum_J m_J \left\langle \frac{\sigma_I}{h_I^2} + \frac{\sigma_I}{h_J^2} \right\rangle gradW_{IJ} + b + \frac{1}{\rho h_I}|N^B|t_I^B \tag{6.20}$$

Where h_I is the height of the landslide at node I, $\bar{u}_I$ is the depth-averaged 2D velocity, t_I^B is the surface force vector at the bottom σ_I^* is the depth-averaged modified stress tensor, and P_{1I} is the pore pressure at the basal surface (Pastor et al., 2009). If the 2D area associated with the node I is Ω, then:

$$m_I = \Omega_I h_I \tag{6.21}$$

$$\bar{P}_I = \frac{1}{2} g h_I^2 \tag{6.22}$$

With $\bar{P}_I$ averaged pressure term. The resulting equations are ordinary differential equations that can be integrated in time using a scheme such as Leap Frog or Runge Kutta (2nd or 4th order) (Pastor et al., 2009). This numerical model was implemented by Pastor and coworkers in a numerical code called "GeoFlow_SPH".

6.2 MODEL CALIBRATION AND VALIDATION

In order to test the SPH-FDM model developed by Pastor et al., 2015a, well-documented flume tests including accurate measurements of both flow propagation heights and basal pore pressures (Iverson, 2003; Iverson et al., 2010, 2011) were selected.
Particularly, the reliability of such model was tested in a 90 m long, 31° steep (channel) flume exiting at a sub-horizontal open plain and the numerical results are compared to the experimental evidences to discuss

the potentialities of the SPH-FDM model to adequately capture the global behavior of the debris flow and measurements of propagation heights and pore water pressures at specific control points (Cascini et al., 2016a,b).

6.2.1 Flume test of Iverson et al. (2010)

As mentioned above, replicated experiments were performed at USGS (United States Geological Survey) in a 90 m long (L), 31° steep flume, constituted by a rectangular concrete channel 2 m wide (*B*), and 1.2 m deep (*H*), with $B/L = 0.025$. The Figure 6.3 shows the longitudinal profile of flume and the geometry of the static debris loaded behind the head-gate (Iverson et al., 2010).
The points in red indicate where the flow thickness and basal pore pressure were measured: "A" and "B" are inside the channel, while "C" is at the exit of the channel in a sub-horizontal pad. The steepness of the flume bed slopes is equal to $\theta = 31°$, up to $x = 74$ m, comparable to the angles of many debris-flow initiation sites (Iverson et al., 2010), and then the slope of the flume bed decreases to 4° along a pseudo-circular curved slide.
The granular mixture was constituted by sand, gravel and mud (on average, 56% gravel, 37% sand and 7% mud), where mud refers to all grains passing at 0.0625 mm. The mixture had modal concentrations of grains in the 8–32 mm size classes and secondary modal peaks in the 0.25 to 0.5 mm size class. The gravel grains were rounded, whereas the sand was mostly sub-angular (Iverson et al., 2010). The geotechnical properties of soils are reported in Table 6.1. Granular mixture was hosted behind a vertical gate through a wedge-shaped prism, as shown in Figure 6.3. The initial sediment volume, including pore space was equal to 9.73 ± 0.45 m^3. The material in the initial state contained about 1.0-1.1 m^3 of water, later the mass was led near to saturation through subsurface channels and surface sprinklers.
This work refers to the experiments named "SGM", performed on a rough bed, made of a surface covered with bumpy concrete tiles (Iverson et al., 2010). The debris-flows motion was initiated by using a hydraulic system to lift the gate. This system, combined with the high static force of wet debris against the gate (40–80 kN), caused it to swing open horizontally in about 1 s (Iverson et al., 2010). Basal pore fluid pressure

was measured through differential strain-gage pressure transducers positioned along the centerline flume: three closely clustered sensors were built into the flume bed for both the cross section A and B (Fig. 6.3), while one single port at the base of the flume (section C in Fig. 6.3). Flow propagation height was measured through laser sensors installed on crossbeams mounted above the bed (Iverson et al., 2010).

The experimental measurements outline that the front of the flow reached a velocity equal to 11 m/s along the steepest portion of the flume (31°). The corresponding maximum height attained about 0.2 m (Iverson et al., 2010) at both points A and B (Fig. 6.4). Correspondingly, the measured pore water pressures were nearly equal to the basal total normal stress; this indicates that the effective stress acting on the solid skeleton of the granular mixture was nearly nil and material was fully liquefied once propagating over the points A and B. As shown in Figure 6.4, all the measurements (at points A, B and C) of both propagation height and basal pore water pressures exhibit an abrupt increase followed by a rapid decrease to a nearly nil steady-state value. This rapid increase-decrease in time clearly corresponds to the rapid transition of the flow above the transducers.

A series of pictures were also acquired during the experiment through a high-speed ready-camera, which show that gravel grains travel more rapidly than finer ones, and constitute a steep front at the head of the flow. Similar evidences are also common from field observations of real-size debris flows and this mechanism is usually referred as "grain-size segregation", and is also active along the vertical, with coarser materials floating above the finest ones. The presence of coarse material propagating at the boundary (at the front and at the top) of the flowing mass enhances a rapid dissipation of pore water pressures.

This special mechanism will be not included in the numerical modelling, and could explain some minor mismatch between experimental evidence and numerical results. A preliminary modelling of these replicate experiments was proposed by George and Iverson (2011) with an acceptable fitting of the experimental results for propagation heights and mismatches for the simulated basal pore water pressures justified with the lack of grainsize distribution into the model. Indeed, in real debris flows and in the experimental flume tests as well, large grains concentrate at the flow front and this process may modify the basal pore water

pressure along the propagation path. The same issue is also discussed by George and Iverson (2014), who still evidence that the lack of grain-size distribution into the model reduces the potential to simulate the experiments. In addition, the analysis of the effects related to the details of the gate-opening, for such gate-release simulations, provided further evidence of the importance of initial conditions (Cascini et al., 2016a,b).

Table 6.1 Geotechnical properties of soils for the SGM rough bed experiment (Iverson et al., 2010).

Property	Value*
Mean wet bulk density of sediment (kN m^{-3})	20.10
Basal friction angle from maximum angle of repose in tilt-table tests (degrees)	40.7±2.1 (N=12)
Internal friction angle from maximum angle of repose in tilt-table tests (degrees)	39.6±2.7 (N=14)
Internal friction angle from triaxial compression in 6- inch cell (degrees)	37 (N=1)
Internal friction angle from triaxial compression in 15-inch cell (degrees)	33 (N=1)
Slurry saturated hydraulic diffusivity (D) (i.e. consolidation coefficient) (measured) (m^2 s^{-1})	1×10^{-6} (N=6)
Slurry saturated hydraulic diffusivity (D) (i.e. consolidation coefficient) (calculated) (m^2 s^{-1})	2×10^{-2}
Total water (initial + added) in sediment at time of flow release (m^3)	3.34±0.45 (N=8)

* The value indicates the mean ± standard deviation obtained from N measurements.

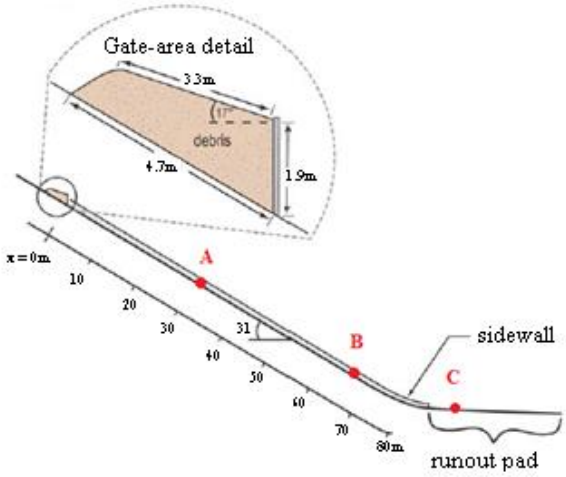

Figure 6.3 USGS flume geometry: longitudinal profile of the flume and geometry of static debris loaded behind the head-gate. The points in red indicate where the propagation heights and basal pore pressures were measured: A (x = 32 m) and B (x = 66 m) are inside the channel, while C (x = 90 m) is at the exit of the channel in a sub-horizontal open plain (Iverson et al., 2010).

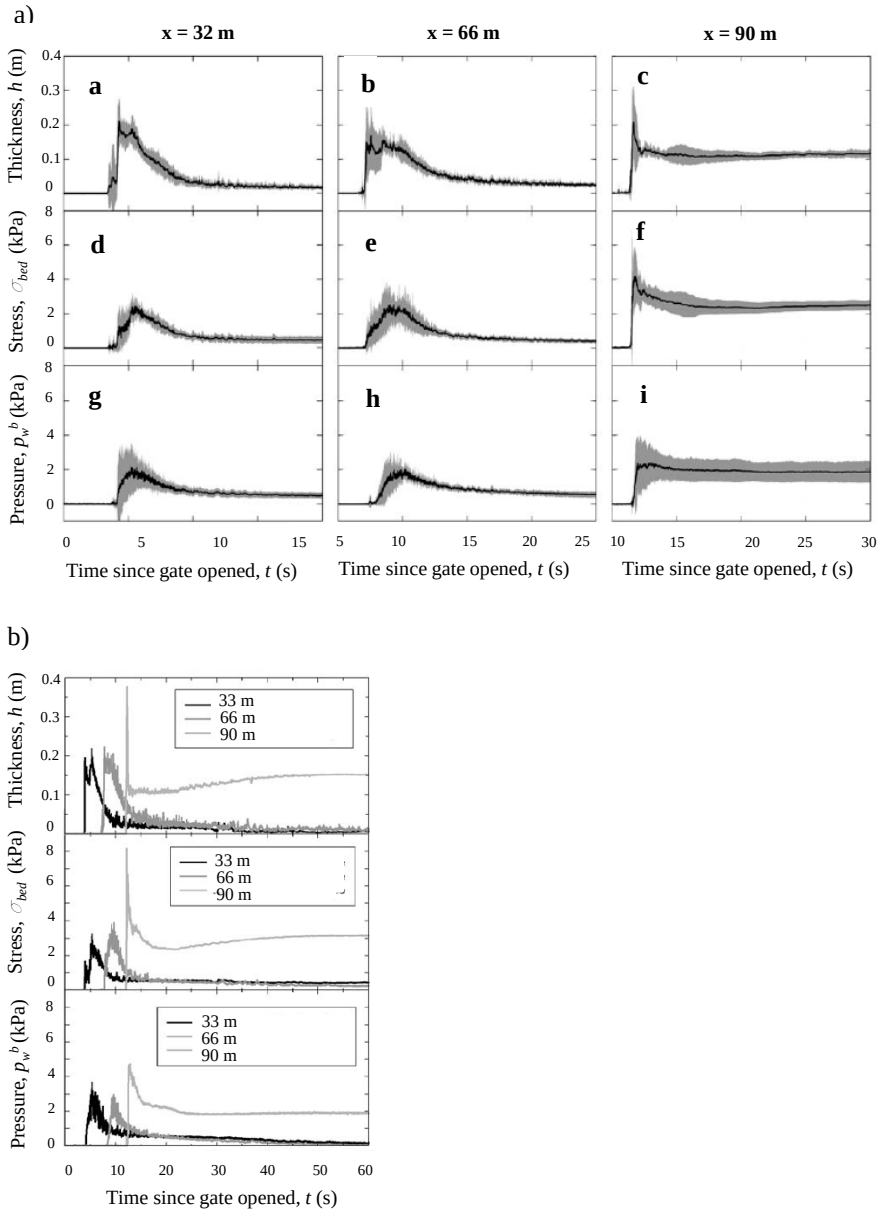

Figure 6.4 a) Aggregated time series data for SGM rough-bed experiments. Mean values (black lines) and standard deviations (gray shaded areas) are shown (Iverson et al., 2010); b) aggregated time series data for the flume experiment of 13 September 2001 (Iverson, 2003).

6.2.2 SPH-FDM numerical modeling

The modeling of such a flume test was developed referring to two different alternatives: *i)* a 2D x-z scheme ($\Delta x = 0.25$ m), which disregards the lateral distribution of the heights and velocities either during the propagation in the channel or at the exit of the channel, where the mass tends to spread laterally, *ii)* a 3D scheme, i.e. a 0.1 × 0.1 m DTM, which takes into account the previous features of the landslide propagation dynamics. For the 3D scheme, the analysis were carried out with the SPH model proposed by Pastor et al., 2009 (solving the Equation 6.5); while for the 2D scheme, with the SPH model and with the SPH-FDM model (described above, solving the Equation 6.6).

This choice was done because the first depth-integrated model solves the SPH propagation equations assuming a quarter cosinus shape function for vertical profile of pore water pressures, while the second model may compute - through a set of finite difference mesh (FDM) - any general vertical profile of pore pressures in relation to the hydraulic boundary applied to the ground surface.

The boundary conditions were well reproduced in the numerical models as it concerns the slope geometry, and the basal friction angle of the rough bed slide available from experimental measurements. Whereas, some approximations were done for the gate opening at the front of the soil mass such as: an instantaneous opening of the gate, e.g. the presence of the gate was not included into the model and, the mass was released without any confinement at the front, so the mass started moving freely (Fig. 6.5), numerical models named, 2D and 3D). Moreover, the presence of the wall shear stresses was not included into the model and these approximations determined a computed average velocity of the flow in the range 15-20 m/s versus measured flow velocity of about 10 m/s. A vast series of numerical simulations was performed assuming a frictional rheological model (Equation 6.7), and the input parameters were taken from the experimental data available from Iverson et al. (2010).

Particularly, it was assumed: *i)* soil unit weight of wet material at flow release (ρ) equal to 20.10 kN m^{-3}, *ii)* basal friction angle (ϕ_b) was

assumed from 25° to 27°, e.g. $\tan(\phi_b) = 0.47$ or 0.52, according to the relation: $\tan(\phi_b) = (1 - ru)\tan(\phi)$, where $ru = \rho_w / \rho$ is the ratio of the water density to the mixture density and ϕ is the dynamic basal friction angle, *iii)* relative water height (h_w^{rel}, e.g. ratio of the height of the water table to the soil thickness) up to 0.4 to take into account the total water (initial + added) in sediment at time of flow release equal to 3.34 ± 0.45 m^3 (N = 8) in an initial volume of 9.73 ± 0.45 m^3 and equal to 0.5 to assume liquefaction condition in the mass *iv)* relative pore water pressure (p_w^{rel}, e.g. the ratio of pore water pressure, p_w, to the total vertical pressure, p, at the base of the flow) equal to 0.5–0.6 in most of the cases assuming the hypothesis that the initial mass was not completely liquefied and equal to 1.0 to assume liquefaction condition in the mass since the beginning, *v)* consolidation coefficient (c_v) equal to 5×10^{-2}, 5×10^{-3} or 5×10^{-5} $m^2\ s^{-1}$ in agreement with the calculated and measured soil saturated hydraulic diffusivity (D) measured from 1×10^{-6} to 2×10^{-2} $m^2\ s^{-1}$ in the experiments.

The most relevant numerical cases are listed in Table 6.2 with their input parameters.

The results of these simulations are reported in Figures 6.6, 6.7 a, b and 6.8. The Figures 6.6 and 6.7 show the comparison between the flume test measurements (test 13 September 2001 of Fig. 6.4b) and the numerical simulation of the Case 5 of Table 6.2 (at points A, B), for both propagation height and basal pore water pressure. The comparison is presented with reference to $t\text{-}t_{flow}$, where t_{flow} represents the time when the flow reaches the observation point. The computed propagation height and basal pore water pressure sharply increase, followed by a similarly fast reduction down to zero, while the experimental measurements outline a slower decrease. The duration of the propagation "wave" is accurately predicted at the point A, while the simulated duration of the wave is almost half of the experimental results at the point B. However, the simulated peaks of soil propagation heights are well simulated in both points. The comparison of the peaks of the soil propagation height (h) and the peaks of basal pore water pressure (p_w^b) simulated for all the Cases of Table 6.2 are shown in Figures 6.8.a, b.

The numerical results are compared to the mean values and standard deviation of the measurements, and should be the points located along the 1:1 line in the plots of Figure 6.6 a, b. In details, the 2D numerical analyses, correctly predict the soil heights for the Cases 2–5 in Table 6.2.

These latter Cases correspond to the highest friction angles considered in Table 6.1 and a consolidation coefficient consistent with that calculated by Iverson (2010). In particular, the Case 5 simulated with SPH-FDM model, gives a peak of the propagation height located exactly on the experimental mean values line. A mismatch is found for the basal pore water pressures, which oppositely to the 2D scheme are simulated better with the 3D analysis.
Focusing on SGM experiment of 13 September 2001, the SPH-FDM model simulates a peak of the propagation height at the point A and pore water pressure at the points A and B, which are equal to those measured by Iverson (2003), i.e. Case 5. On the other hand, the Cases 2, 3 and 4 respectively have a larger h_w^{rel} (Case 2 and 3) or a smaller c_v (Case 4) compared to the best fit-cases (Case 5 and Case 5_3D); due to this, the simulated peaks of propagation height are comparable with the experimental measurements while the peaks of pore water pressures are not well reproduced. It is interesting to note that all the simulations carried out with the SPH model overestimate both the peaks of propagation height and pore water pressure compared to the new SPH-FDM model.
To sum up, the flume tests performed by Iverson (2010) and Iverson (2003) were properly simulated with different levels of approximation, either in 2D or 3D analyses. This is a valuable result also considering that the grain-size segregation is not reproducible in any numerical model and the models with a fixed rheology provide a global simulation of flow propagation, while not differentiating the behavior of the liquefied body of debris flow and the unliquefied front. As a contribution to the previous literature on the topic, the proposed SPH-FDM model simulates peaks of both the soil propagation height and pore water pressure higher than those simulated by George and Iverson (2011, 2014), with an acceptable global fitting of the experimental insight (Cascini et al., 2016a,b).

a)

b)

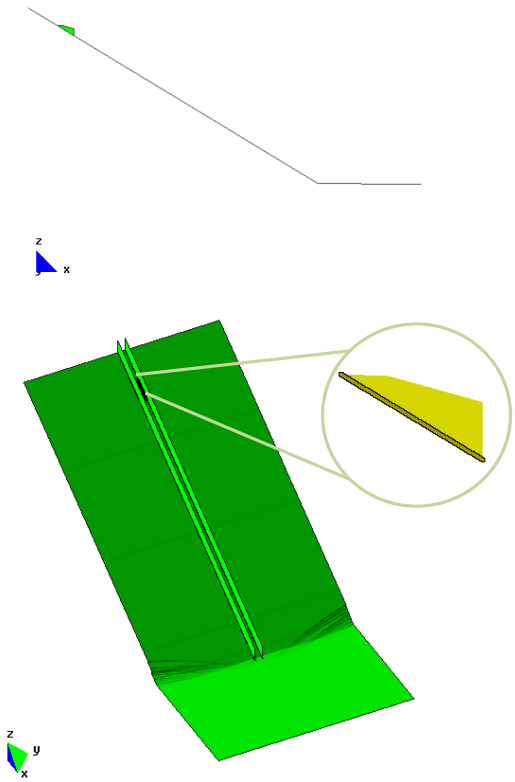

Figure 6.5 Geometrical schemes for the 2D (a) and 3D (b) analyses with the indication of the mass at the early stages of the test before the opening of the gate.

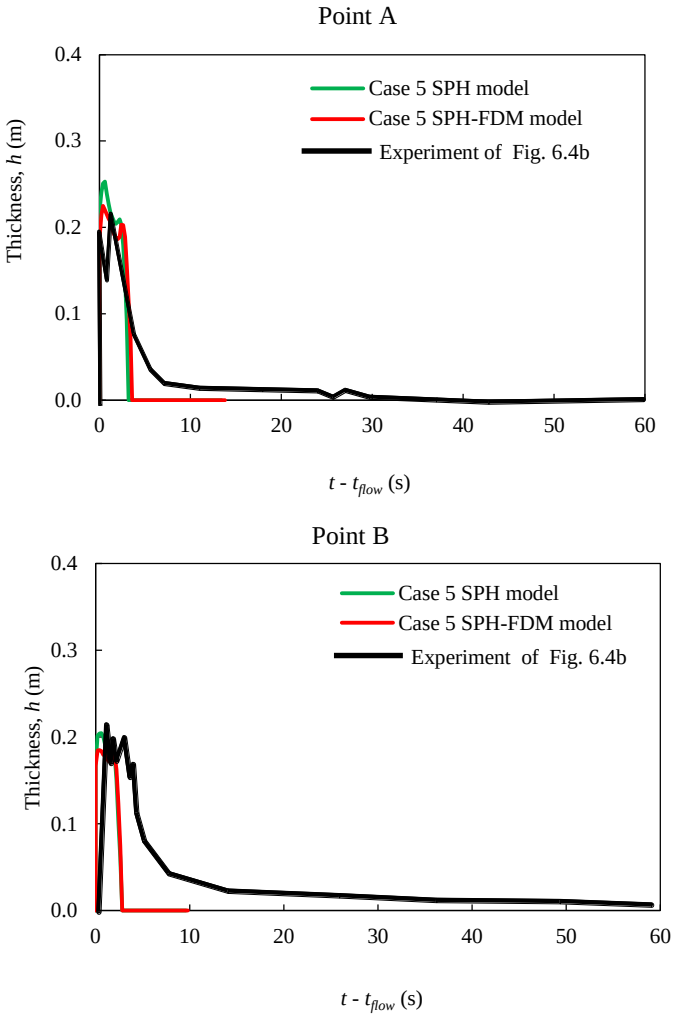

Figure 6.6 Comparison of the flume test measurements and numerical simulations: evolution of flow depth (*h*) at the points A and B.

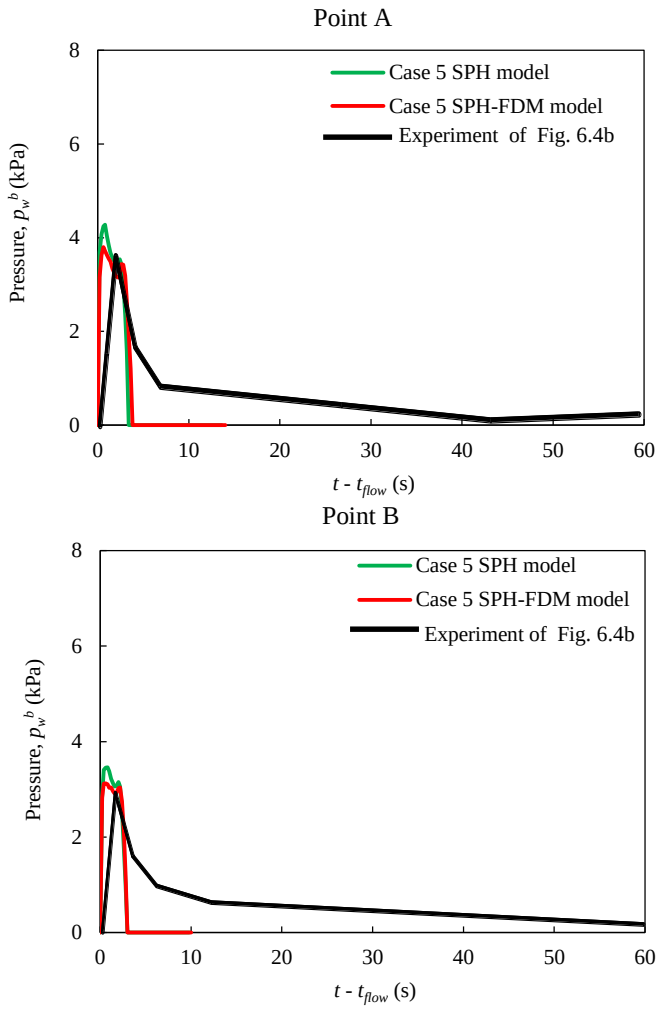

Figure 6.7 Comparison of the flume test measurements and numerical simulations: evolution of basal pore water pressure (P_w^b) at the points A and B.

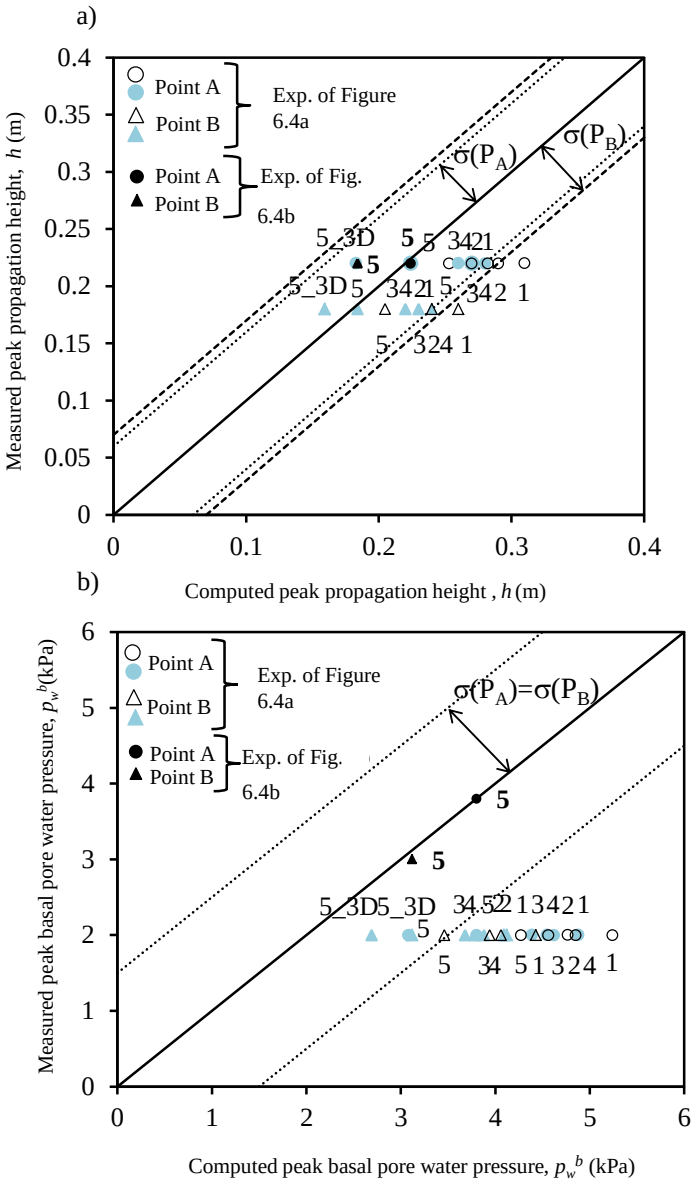

Figure 6.8 Comparison of the experimental measurements and the numerical simulations: a) peak of the propagation height (*h*); and b) peak of the basal pore water pressure (p^b_w) at points A and B. The legend refers to the experimental of Figure 6.4a, b. The simulations with SPH model are represented with empty

symbol, while the simulations with SPH-FDM model are represented with solid black and solid blue. The results are compared to the mean values and standard deviation (s) of the measurements at the point A (P_A) and B (P_B).

Table 6.2 Rheological parameters for the numerical simulations of the flume tests performed by (Iverson et al., 2010).

Case	*Models*			*tan* ϕ_b *(-)*	h_w^{rel} *(-)*	p_w^{rel} *(-)*	c_v $(m^2\ s^{-1})$
1	2D	SPH	SPH-FDM	0.47	0.3	0.6	5.0×10^{-2}
2	2D	SPH	SPH-FDM	0.52	0.2	0.5	5.0×10^{-2}
3	2D	SPH	SPH-FDM	0.52	0.1	0.5	5.0×10^{-2}
4	2D	SPH	SPH-FDM	0.52	0.05	0.5	5.0×10^{-3}
5	2D	SPH	SPH-FDM	0.52	0.05	0.5	5.0×10^{-2}
5_3D	3D		SPH-FDM	0.52	0.05	0.5	5.0×10^{-2}

ρ*:* mixture density equal to 20.10 kN m^{-3}, ϕ_b: basal friction angle, h_w^{rel}: relative water height, p_w^{rel}: ratio of pore water pressure to liquefaction pressure; c_v: consolidation coefficient.

6.3 FLOWS REGIME ANALYSIS THROUGH SPH-FDM MODEL

As in the previous Chapter, the SPH-FDM model was used to estimate the kinematic characteristics of flows; starting from the well-known case of water flow and then passing to frictional flows regime. For numerical analysis the same mass and channel geometry analyzed in Section 5.2 was used (see Fig. 5.1). All numerical analysis were repeated through the SPH-FDM model which is more suitable to simulate phenomena such as granular flows or debris flows, treating the propagating mass with the pore water pressure as an added variable. The Newtonian flow analyses were carried out to compare the FV model described in Chapter 5 and the SPH-FDM model described above.

6.3.1 Newtonian flow analysis

Resolving the Equations 6.1 and 6.2, and using a Chezy-Manning reology (Equation 6.8) for a 1D dam break problem of a water mass flowing along a horizontal surface with an initial height (h_{in}) equal to 10 m and initial length (L_m) equal to 10 m, it is possible to compare the height, the velocity and Froude number computed by both FV model and SPH-FDM model. As it concerns the Manning coefficient *m'* in the Equation 6.8, it is evaluated through the hydraulic relations as function of roughness coefficient (χ) and imposing the roughness index "m" equal to 0.5 $m^{1/2}$ (see Equation 5.2a in Section 5.1); in this way m' resulted equal to 0.02 $s/m^{1/3}$. The Figures 6.9, 6.10 and 6.11 show the computed height, velocity and Froude number using SPH-FDM model and FV model. *Fr* is evaluated as function of *h* and *u*, according to general expression $Fr=u/(gh)^{1/2}$. It is possible to observe: i) an overall agreement between both models and ii) high values of Froude number arising at the front of the flow in a very short time. This second issue is relevant for real flow-like landslides since the mass may have distinct behavior, i.e. the front of the mass moving as a supercritical flow, while the rear part of the mass as subcritical flow (Cascini et al., 2017).

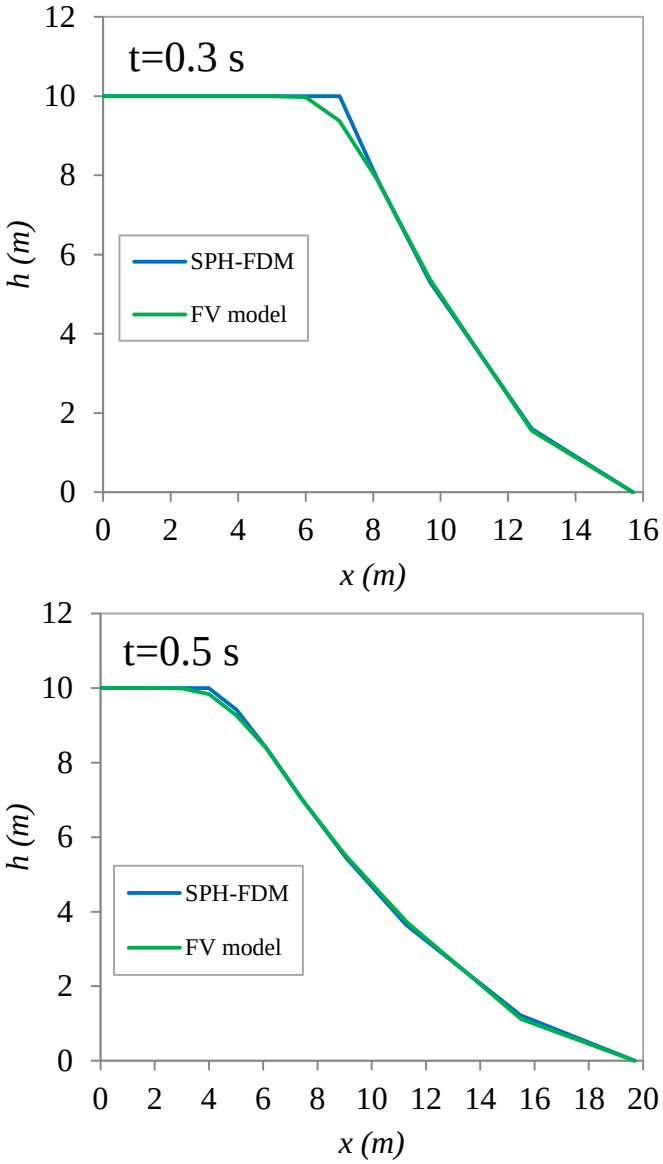

Figure 6.9 Computed height with SPH-FDM and FV methods of a water flow at t=0.3s and t=0.5s.

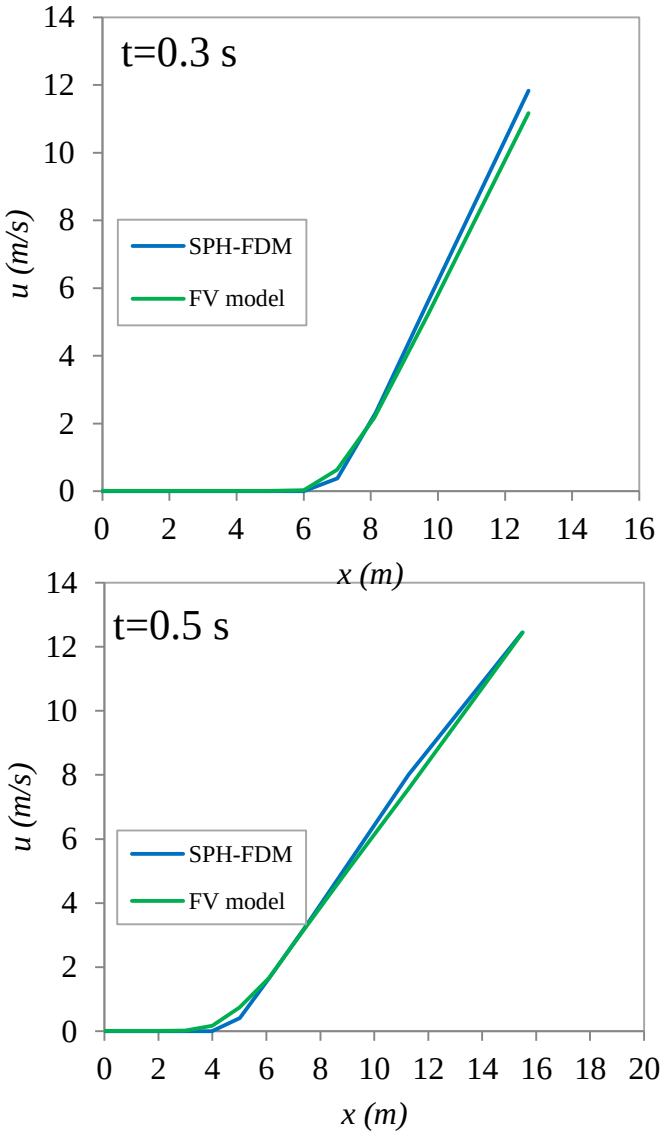

Figure 6.10 Computed velocity with SPH-FDM and FV methods of a water flow at t=0.3s and t=0.5s.

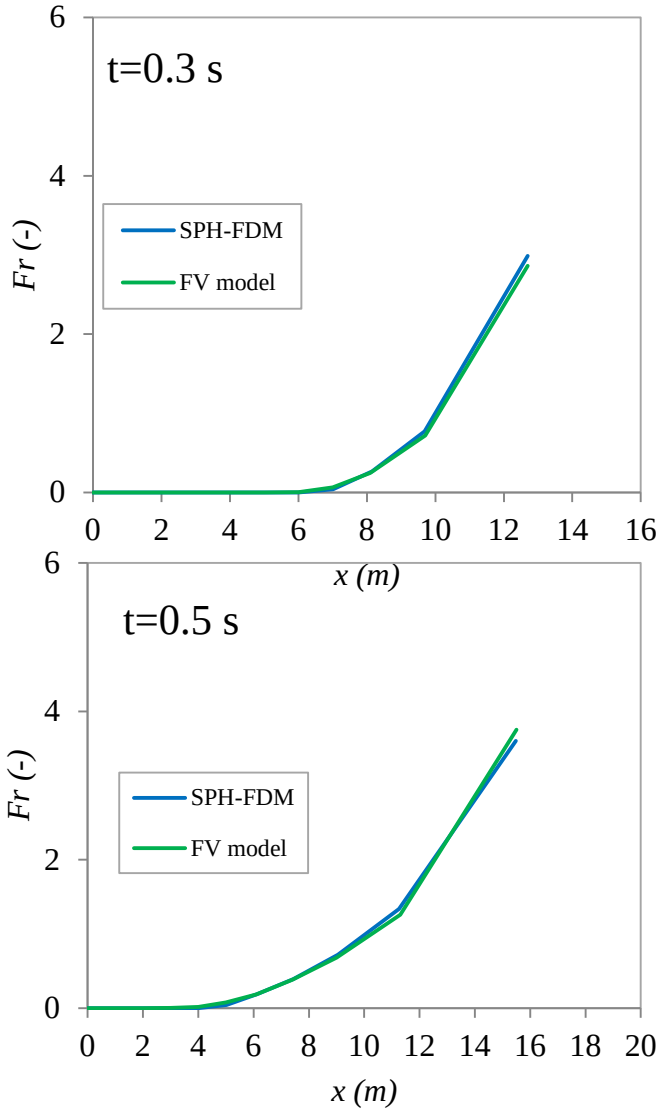

Figure 6.11 Computed Froude number with SPH-FDM and FV methods of a water flow at t=0.3s and t=0.5s.

6.3.2 Frictional flow analysis

In the same way of the Cross-Bingham flow analysis (see Section 5.2.2), the Frictional flow analyses were performed. Particularly, the Frictional modeling refers to a 1D unsteady flow moving over a surface inclined of an angle θ respect the horizontal. A vast series of numerical simulations was performed changing the frictional angle, the initial height of mass and geometry (L=1 km, Δx=0.1, L_m=10 m, θ=0, 10, 20, 30 or 40°, h_{in}=1, 5 or 10 m). The rheological parameters of the Equation 6.7 were taken from literature (Pastor et al., 2009, Cascini et al., 2012, Cascini et al., 2014 and Cuomo et al., 2014); these value were mainly used by those authors to back-analyze catastrophic channelized flowslides occurred during the May 1998 events in Campania region. The authors consider: $tan\ \phi_b$ equal to 0.35-0.40; h_w^{rel} =0.40; p_w^{rel} =1.0; c_v =1.0×10^{-2} m^2 s^{-1}. For the Frictional flow analysis, $tan\ \phi_b$ was assumed variable from 0.0 to 0.60, corresponding to ϕ_b from 0.0 to 30°; to establish a connection between the flow regime and rheological properties of the flowing mass.
Figures 6.12 and 6.13 show the Froude number evaluated at the front of the flow when it arrives at two target sections located 50 and 100 m far from the triggering zone. It was found that the larger the slope angle of the surface of the initial height of mass, the higher is the Froude number.

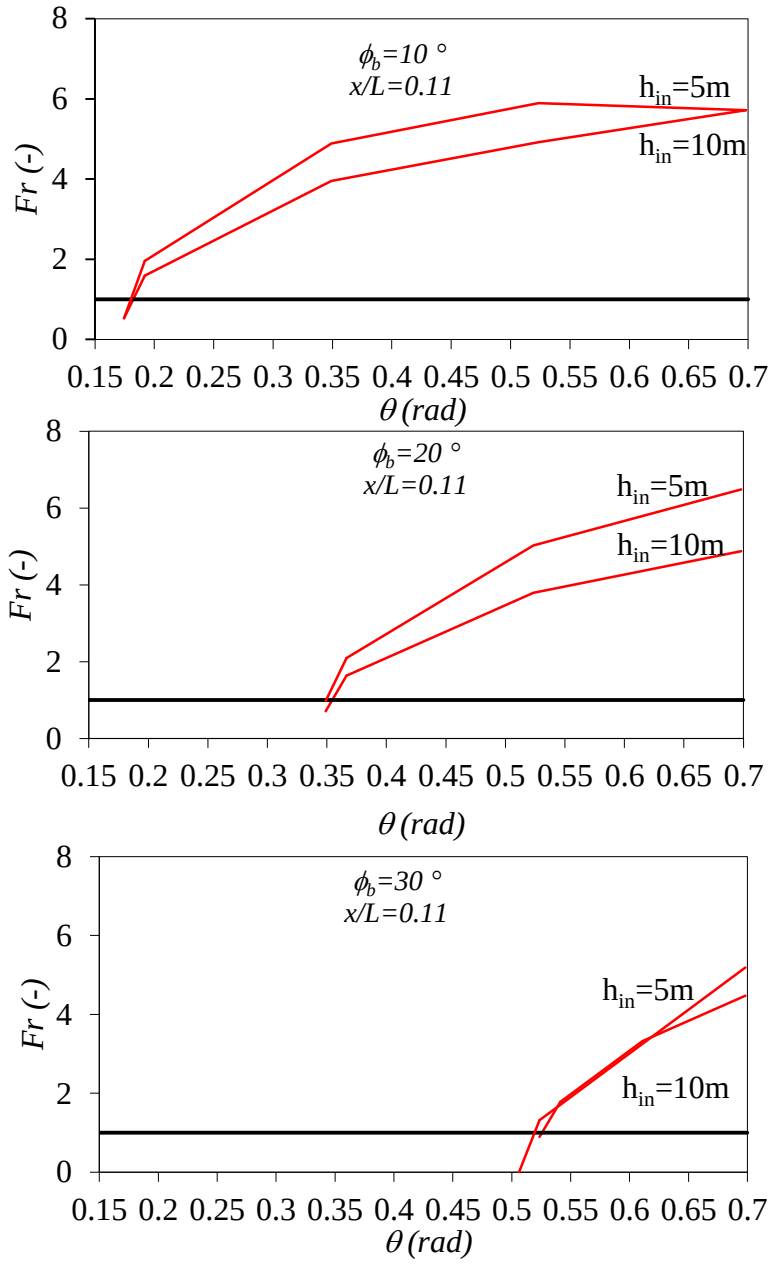

Figure 6.12 Froude number of Frictional flow with h_{in}=10 and 5m for different channel slope and frictional angle of the flow.

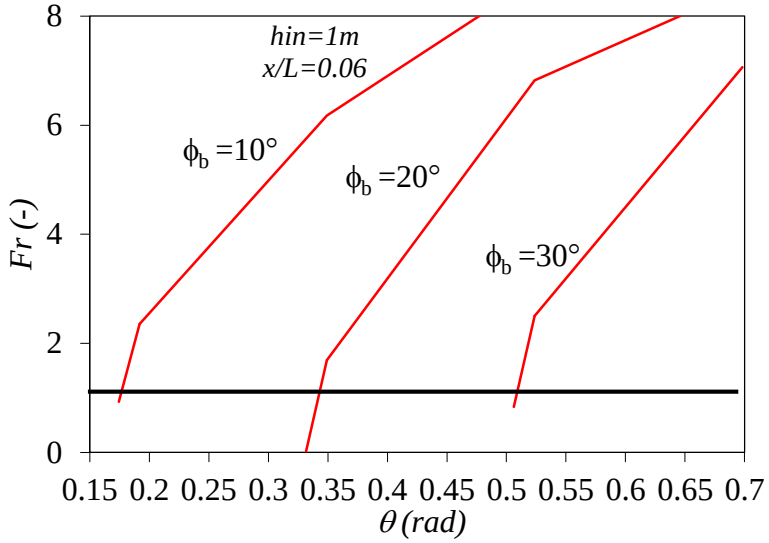

Figure 6.13 Froude number of Frictional flow with h_{in}=1m for different channel slope and frictional angle of the flow.

Moreover, the critical slope angle θ_{crit}, i.e. the slope that determines the transition from supercritical to subcritical flow, corresponds exactly to frictional angle of the flow and is independent on the initial height of the mass. For example, a propagating mass with initial height equal to 1, 5 or 10 m, with the frictional angle ϕ_b equal to 10° and the others above-mentioned specified rheological parameters, presents a transition from "rapid" to "slow" flow in correspondence of channel slope θ_{crit} equal to 10°. This numerical outcome well matches the previous literature (Linghtill and Whitham, 1955; Al-Mashidani and Taylor, 1974; Woolhiser 1977; Govindaraju et al., 1988; Arattano and Savage, 1994; Richardson and Julien, 1994).

Particularly, Richardson and Julien (1994) investigated one-dimensional unsteady water flow in open channel and evaluated analytically the dimensionless acceleration terms of the momentum equation (local acceleration a_l^*, convective acceleration a_c^* and pressure gradient a_p^*; function of $\partial u/\partial t$, $\partial u/\partial x$ and $\partial h/\partial x$, respectively) during the propagation phase. The Figure 6.14 shows that all three dimensionless

acceleration terms are initially zero and then a_l^* increases rapidly up to 0.04, while both values of a_c^* and a_p^* are negative, so the numerical sum of acceleration terms is about equal to 0.02. However, they conclude that the sum of acceleration terms could be neglected and for this condition the kinematic wave approximation is suitable. The kinematic wave approximation reduces the momentum equation to equality between channel slope and flow resistance term and is appropriate for supercritical flow with Fr>1.4 and for steep channels.

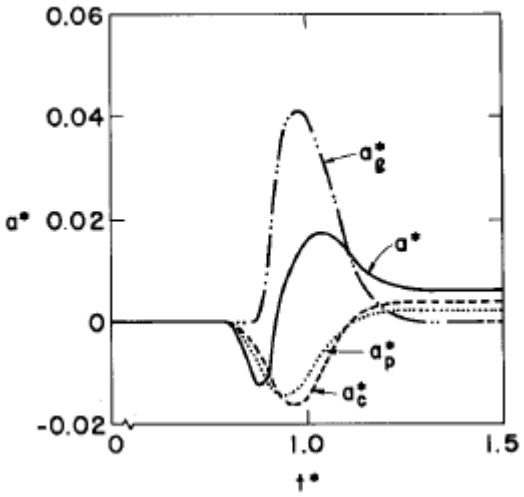

Figure 6.14 Acceleration terms of a water flow in open channel (from Richardson and Julien, 1994).

Arattano and Savage, 1994 used kinematic wave to modeling two debris flows; the agreement between the computed and measured height and velocity of the flows prove the irrelevance of the acceleration terms during the propagation.

Another important aspect is revealed by the Frictional flow analysis, the initial height of the flowing mass seems to be not relevance with respect to the calculation of the channel critical slope θ_{crit} . This aspect is to be found in classic hydraulics theories. Indeed, assuming: i) high height of the propagating mass ($m/h^{1/2}$ about equal to zero, with m the roughness

index) and ii) infinitely wide channel ($R_i=h$, with R_i hydraulic radius) the channel critical slope in uniform motion conditions is the following:

$$\theta_{crit} = \frac{g}{\chi^2}\frac{A}{B R_i} \text{ with } \chi = \frac{87}{1+\frac{m}{\sqrt{R_i}}} \quad (6.23)$$

This expression derives from equality between the uniform flow rate (calculated with Chezy, Equation 5.2a in Section 5.1) and the critical flow rate; for the above-mentioned hypothesis the critical slope become equal to $g/87^2$ i.e. completely independent of the flow height.

6.4 DISCUSSION

A SPH-FDM model was presented, which combines two sub-models: a 3D depth-integrated hydro-mechanical coupled SPH (Smooth Particles Hydrodynamics) propagation model, and a 1D vertical FDM (Finite Difference Method) model for the evaluation of the pore water pressure along the height of the propagating mass.
The SPH-FDM model was used to simulate, in 2D and 3D analyses, well-documented flume tests performed in a 90m long, U.S. channel flume exiting at a sub-horizontal open plain; later to analyze the Newtonian and Frictional flows regime.
The results of the calibration well match the experimental evidences of U.S. channel tests; indeed, the SPH-FDM model is capable to properly reproduce the propagation height and velocity, as well as flow deposition, and more importantly to correctly simulate the time-space evolution of pore water pressures during the whole propagation stage from initiation to propagation.
A comparison between the FV model and SPH-FDM model for a dam break problem of a water flow was performed and also in this case the results showed an excellent agreement between the computed variables by both models (flows height, velocity and Froude number).
The Frictional flow analysis highlighted some aspects already found in Cross-Bingham flow analysis, e.g. the higher is channel slope, the higher

is Froude number; the higher is initial height of the flow, the higher is Froude number. However, the Froude number of viscoplastic flows (or Cross-Bingham flows) is greater than Frictional flows (see Chapter 5).
Other considerations were made as it concerns the transition from "slow" (or subcritical) to "rapid" (or supercritical) flow; such considerations do not deviate much from those of classical hydraulics theories, e.g. the acceleration terms during the propagation are negligible, so the granular flows or debris flows can be modeling through kinematic wave approximation and the calculation of the critical channel slope depends on the mechanical characteristics of the soil (friction angle), while does not depend on the initial height of the mass.

7 EFFECTIVENESS OF THE PROPOSED APPROACH: THE CASE STUDY OF CANCIA

The case study of Cancia is emblematic since some storage basins dramatically failed in 2009 due to a short-time sequence of rainfall-induced debris flows and flash floods. Thanks to an accurate data-set, these events are analyzed through the SPH model using as input data detailed field evidences during the time and a set of different rheological models taken from the literature and calibrated for the study area. The numerical results confirm the efficiency of the control works against debris flows and their unsuitableness for the subsequent flash flood. This issue is tackled referring to the Froude number highlighting that debris flows and flash floods propagated like subcritical and supercritical flow, respectively (Cascini et al., 2017; Rendina et al., 2017).

7.1 CASE STUDY

7.1.1 Site description and past events

The study area is located in the Dolomite Alps that border the Northern Italian territory and are characterized by a typically "alpine climate" with spring and autumn moderately cold, freezing winter, and average yearly cumulated rainfall of about 1,000 mm. Rainy season mainly last from June to September, with the maximum daily rainfall equal to about 500 mm, i.e. half of the yearly cumulated rainfall. In addition, freezing and snow melting regularly alternate along the seasons, causing intense weathering of rocks and superficial soil covers. Consequently, huge debris flows and minor flow-like mass movements systematically occur along several torrent catchments (Tecca et al., 2003).

This is the case of the "Cancia" catchment (Borca di Cadore, N 46°25'30.22", E 12°14'19.95") which extends from 2,451 m a.s.l. (top of the Antelao Mount) down to the valley approximately situated at 900 m a.s.l.. In the catchment two main torrents, named "Boite" and "Bus del Diau", join at the intermediate elevation part of the massif (1,335 m a.s.l.) threatening the houses located downslope (Fig. 7.1).

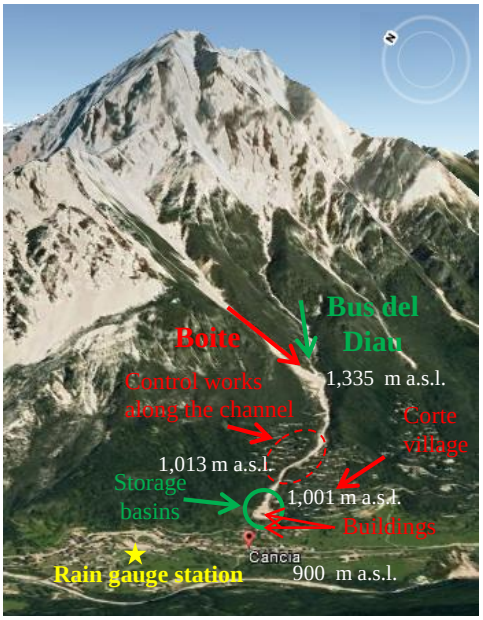

Figure 7.1 Antelao Mountain and Cancia catchement (Borca di Cadore) located in the Northern Italian Dolomite Alps, N 46°25'30.22", E 12°14'19.95" (Cascini, 2011).

Both the torrents are about 35° steep in the uppermost portion while at the conjunction area of the torrents the maximum steepness is about 25°. Downslope this zone, the longitudinal profile of the channel (where the major flows occurred) is gentler, from 22° down to 8°. The "Bus del Diau" torrent is essentially free of sediments while the "Boite" torrent is filled by debris originated from the instability phenomena of the Antelao

Mount. Such debris is systematically mobilized by rainfall infiltration or runoff and several typologies of flows can be originated.

The catchment and the surrounding areas have undergone during the last 60 years several changes due to the flow-like mass movements occurred, the urbanization of some areas and the construction of control works in the piedmont area aimed at reducing the risk to life and property in the Cancia village. The latter developed up to 1957 while the tourist village "Corte" was built during the 50's and 60's. Some of the houses damaged by the past events were also rebuilt. They consisted in small 2-floors wooden buildings and cottages nearby the main road of the valley and the tourist village.

Because of the recurrence of many flow-like mass movements and simultaneous urban development of the area, a retaining wall was built along the channel during the 55's and 60's to protect the Corte Village.

Moreover, two adjacent storage basins were constructed at the piedmont area. The first was built before the 90's, being a small triangular basin located at 1,013 m a.s.l., with storage capacity of approximately 7,500 to 8,000 m3. The second basin was ovoid-shaped, 25,000-30,000 m3 sized, and located downslope the first basin (at 1,001 m a.s.l.). Built in 1998, it was expected to be temporary during the construction of a bigger final basin storage. Unfortunately, at the time of the 2009 events, the bigger storage basin was still hosting a three-floors concrete building (Fig. 7.1 and labelled as building "1" in Fig. 7.4), supposed to be demolished during the storage construction, but still there due to administrative delays.

Cancia village was affected by several flow-like mass movements in the past as it is highlighted by the available dataset that includes a total number of n. 11 events (Table 7.1) starting from 1868 when an estimated volume higher than 100,000 m^3 threatened the downslope urban area. Afterwards, several other events occurred until the end of the last century when two medium-sized flows (tens of thousands of cubic meters) reached the piedmont area in 1994 and 1996, respectively (Fig. 7.2).

Table 7.1 Past events at the Borca di Cadore cacthment.

Date	Volume (m^3)
27/07/1868	> 100, 000
27/05/1957	25,000
05/11/1966	25,000 m^3
19/07/1987	> 10,000;15,000
02/07/1994	25,000; 30,000
07/08/1996	40,000; 40,000-50,000; 60,000
16/08/1999	6,000-7,000
20/09/1999	50,000
01/08/2002	800
04/09/2005	900
18/07/2009	30,000

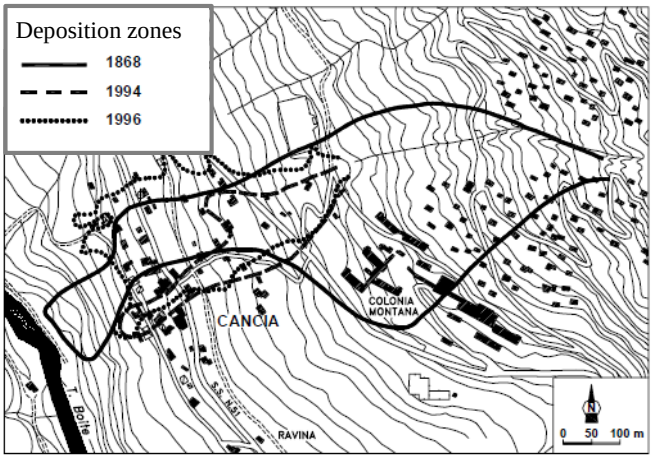

Figure 7.2 Deposition zones of the debris flows occurred in 1868, 1994 and 1996 (Bacchini and Zannoni, 2003).

Finally, another phenomenon occurred in 2009 whose features will be discussed in Section 7.2.2. Referring to the data in Table 7.1, all the events have been analysed following the procedure proposed by Moon et al. (2006), which allows to obtain estimates of both Frequency (referring to return period) and Magnitude (in terms of total mobilized volume). The results are summarized through the so-called F-M curve (Fig. 7.3), representing the annual frequency ("F", i.e. given by the inverse of the time interval, expressed in years, between two consecutive events), versus the magnitude of each class of past event ("M", i.e. mobilized volumes, sorted in descending order). The linear regression so obtained is characterized by a correlation coefficient (R^2) equal to 0.9482. Additional information about the past events were taken from Bacchini and Zannoni (2003) as it concerns: i) the quoted alluvial fans of the 1994 and 1996 events, ii) and that of the huge event dated 1868, when the urbanization along the catchment and the piedmont area was totally different (Fig. 7.2). Furthermore, Ferretti (1995) describes the 1994 event in a geological report, identifying multiple flow-like mass movements characterized by some debris flows that stopped at the piedmont area and one flash flood that propagated beyond the urban area of Cancia. Further data as well as specific information are not at hand to distinguish the triggering mechanisms characterizing the occurred phenomena (Cascini et al., 2017).

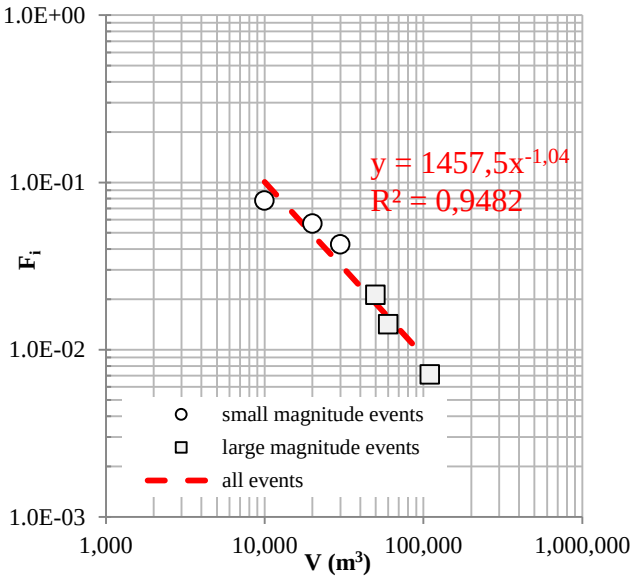

$i = 1,...n$ class of events with a volume (M) :
(i.e. class "1" with volume of 0 - 10'000 m^3;
class "2" for 10'000 - 20'000 m^3, etc.)

n_i number of events for each class

Δt time interval

$f_i = n_i / \Delta t$ absolute frequency of events for each class

$F_i = \sum_i^n f_i$ cumulatuve frequency (F) of events

$T_i = 1 / F_i$ return period (T) of events

Figure 7.3 Frequency-Magnitude (F-M) curves computed for the Cancia catchment.

7.1.2 The July 2009 events

The catastrophic flow-like mass movements recorded on early 18th July 2009 were caused by intense rainfall recorded, from 1:50 a.m. to 4:00 a.m, in the rain gauge station of "Rovina bassa di Cancia" highlighting two peaks of rainfall intensity: the first peak was equal to 11.6 mm in 5 minutes (2:55 a.m.) and the second peak equal to 6.2 mm in 5 minutes (3:40 a.m.).

As a consequence of rainfall, several surges of debris flows (DFs) were heard by a resident person who has been moving beside the control works and in the forest while trying to understand and to react to what was happening. Some tens of minutes later the same resident person, who at that time was near the house where two victims were recorded, heard a strong roar immediately followed by a flow impacting his house. On the basis of this eyewitnesses Cascini (2011) argued that a large volume of solid and water (debris flow, DF) filled the first storage basin and most of the second basin in between 3:15 and 3:20 a.m. while, at about 4:00 a.m., a small volume with a low concentration of solid (flash flood, FF) overpassed both the storage basins and reached the building where two people living inside were killed.

Figure 7.4 shows the tracks of the flows recorded after the events in the area where the storage basins were located, along the short distance between the large storage basin and the impacted house, outside and inside the impacted house.

Particularly, the DF reached maximum deposition height (8,00 – 10,00 m) in the upstream zone of the building labelled as "1" in Figure 4a (located in the storage basin at 1,001 m a.s.l.). The FF impacted the building "1" (Figs 4c, d, e) and caused the failure of the storage basin wall at 1,001 m a.s.l. (Fig. 4f). Later, the FF eroded the ground surface (Fig. 4 g) and reached the building "2" where the traces of the flows are evident in Figure 4a (1,50 m high). The traces on both buildings were 6-9° inclined and are attributable to the flash flood. The victims were sleeping in the basement of the building "2".

Referring to the described sequence of flows it can be observed that the reaction of the resident in Cancia village was significantly influenced by the night time and the active emergency plan suggesting resident people

to stay at home during any flow-like mass movement, also closing the windows and the doors and transferring to the second floor. These suggestions relied on the assumption that each potential flow may travel at low velocity regardless of its magnitude, that is true for a debris flow (DF) but not for a flash flood (FF) similar to that probably occurred on 1994 as can be argued by the description provided in Ferretti (1995) (Cascini et al., 2017; Rendina et al.,2017). However, site-specific measurements of flow velocity were not available for none of the flows, while in other nearby instrumented catchments velocity of 5-15 m/s had been previously measured (Tecca et al., 2003).

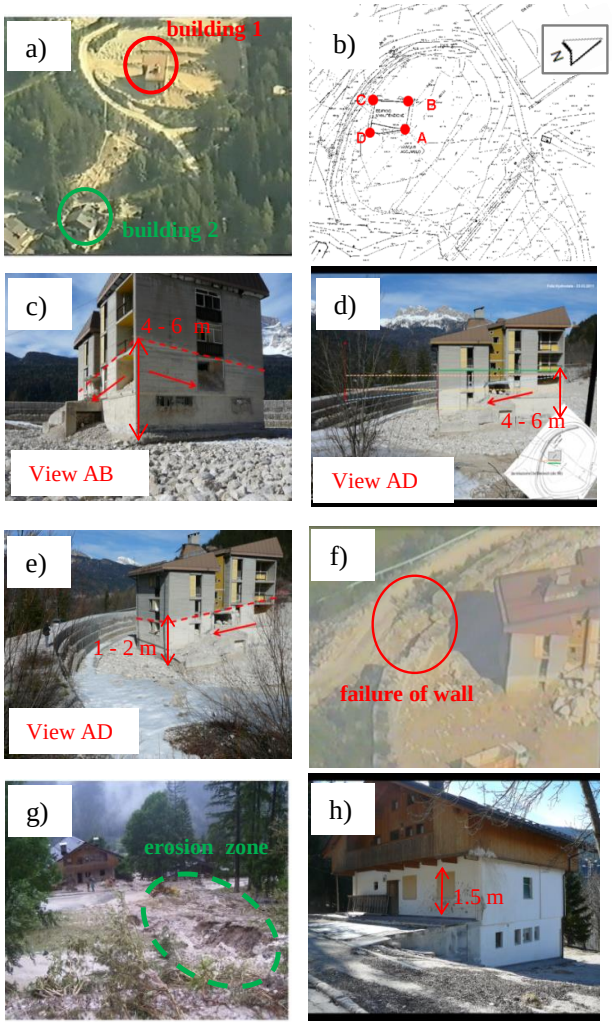

Figure 7.4 Some effects caused by the events dated 18th July 2009: a) buildings location; b) location of building 1 in storage basin; c), d), e) post-events traces on building 1; f), g) erosion zones and h) post-events traces on building 2.

7.2 NUMERICAL MODELING

Understanding the events occurred in 2009 at the study area is not a simple task for two reasons at least. Firstly, a descriptive reconstruction of time-sequence of events is only available for 1994 event (Ferretti, 1995) without any further detailed information. Similar comments are not provided for the other phenomena in the available database even though the shape of the alluvial fans suggests that a sequence of DD and FF cannot be considered an unusual event. Secondly, the magnitude of the event occurred on 18th July 2009 at 4:00 a.m., defined as FF, cannot be quantified since it essentially left tracks on several elements such buildings and walls while not a sediment volume deposited in a well-defined area.

Consequently, numerical modelling is of paramount importance bearing in mind that each numerical result is consistent only if derived from well-calibrated models implementing accurate input data and, if possible, allowing the estimation of additional and not usual information according to the current practice. For all these reasons different approaches were used and hereafter described together with the necessary information on the Froude number Fr, that is implemented for the first time to estimate the kinematical characteristics of different flows ranging from DD to FF (Cascini et al., 2017; Rendina et al., 2017).

7.2.1 The model

The flows were analyzed through the mathematical model "GeoFlow_SPH" described in Chapter 6 and the behavior of the flowing mass was implemented through Chezy-Manning model (Equation 7.1), frictional-type model (Equation 7.2) or frictional-type model with internal pore water pressure (Equation 7.3) that can be written:

$$\tau_b = -\frac{\rho g m^{'2}}{\frac{7}{h^{\frac{1}{3}}}} \cdot sgn(\bar{u}) \tag{7.1}$$

$$\tau_b = -\left((1-n)(\rho_s - \rho_w) g\, h\, tg\phi_b\right) \cdot sgn(\bar{u}) \tag{7.2}$$

$$\tau_b = -\left((1-n)\left(\rho_s - \rho_w\right) g\, h - p_w^b\right) tg\phi_b\, sgn(\bar{u}) \tag{7.3}$$

where τ_b is the basal shear stress of the flow, ϱ is the unit weight of flowing material and m the Manning number (Pastor et al., 2009b), ρ_s is the solid grain density, ρ_w is the water density, g is the gravity acceleration, ϕ_b is the basal friction angle (Pastor et al., 2009a), n is the soil porosity, h is the propagation height, p_w^b is the excess of pore water pressure to hydrostatic, sgn is the sign function and $\bar{u}$ is the depth-averaged flow velocity.

The numerical model implements the Froude number (Fr) that depends on the flow height and velocity during the propagation stage and for this reason it is a spatial-and temporal-dependent variable, as follows in Equation 7.4 (Cascini et al., 2017).

$$Fr(x,y,t) = \frac{u(x,y,t)}{gh(x,y,t)^{\frac{1}{2}}} \tag{7.4}$$

7.2.2 Methods and input data

In the case study of "Cancia" catchment, Equation 7.2 was used for model calibration referring to the events occurred in 1994 and 1996, essentially due to the available input data that did not allow the implementation of a more advanced rheological behavior. Once calibrated the same model was used to interpret the events occurred on 2009 while Equation 7.3 was later implemented to analyze the DF deposited in the storage basin.

Finally, the code MIKE 11-UHM (DHI Water Environment Health, 2003), as commonly done for hydraulic engineering purposes, was used to estimate the magnitude of the FF occurred at 4:00 a.m. in Cancia due to the lack of data usable to this aim. The procedure implemented in the code is the Unit Hydrograph Analysis and the hydrological evaluations were developed for the "Bus del Diau" basin with an area equal to 0.9 km^2. The assumption used for volume estimation is fully saturated soil based on CORINE Land Cover inventory and lithological features of the site.

As for the input data, the quality of the DTM is a crucial issue for a proper description of the ground surface and affects the global reliability of numerical results, as thoroughly discussed for the general aspects in (Pastor et al., 2014), and for the case of flows interacting with baffles in Cuomo et al. (2017). Thus, high-quality Digital Terrain Models (DTMs) were used for analysing both the flows occurred in 1994 and 1996, used as benchmark for more detailed analyses, and those dated in 2009.

Particularly, an accurate 1×1m DTM of the sites for the pre-failure stage on 2009 was obtained referring to the LIDAR survey of the Italian Environmental Ministry (Cascini, 2011) including the control works in the area that were all complete on 1998 (Fig. 7.5a). As it concerns the post-failure stage, the previous data were added with those deriving from an accurate topographical survey of the storage basins, which resulted almost full of sediments as shown in Figure 7.5b,c. Particularly, the figure provides some significant cross-sections of DTMs at the location of the first storage basin (labelled as section "1"), between the first and the second basin (section "2"), along the second storage basin (sections "3" and "4") with the section "4" crossing the building "1", and in correspondence of the building "2" (section "5"). Finally, to analyse the events dated 1994 and 1996, the DTM of the pre-failure stage was modified on the basis of field evidences and literature information. Some changes to the DTM were carried out to delete the storage basin at 1,001 m a.s.l., built in 1998; particularly, the elevations curves were modified between 1,001 m a.s.l. and 995 m a.s.l. (Fig. 7.6).

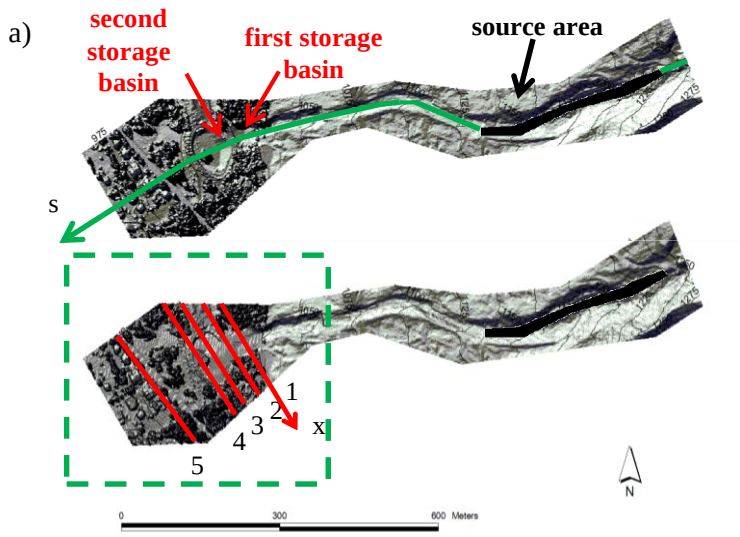

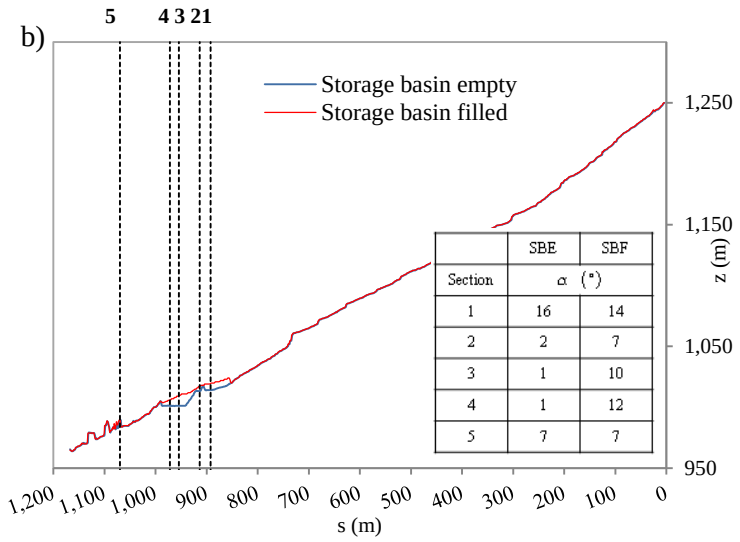

	SBE	SBF
Section	α (°)	
1	16	14
2	2	7
3	1	10
4	1	12
5	7	7

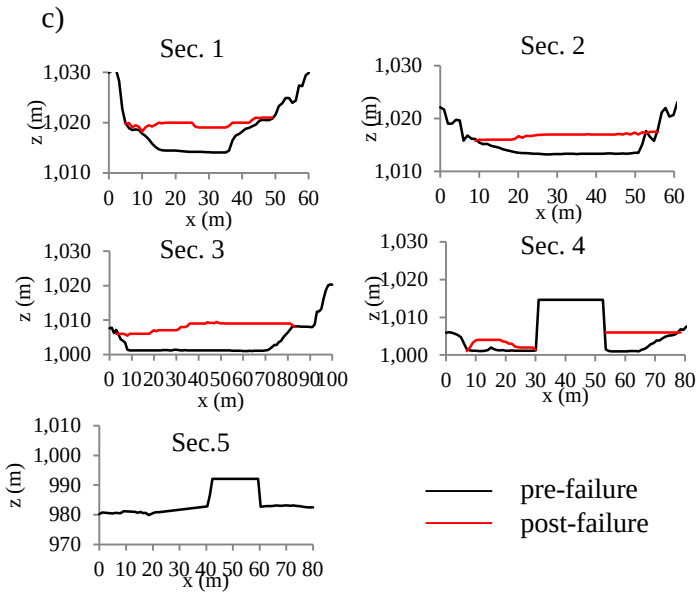

Figure 7.5 DTM used for the numerical modelling of the flows occurred in 2009: a) topography pre-failure (storage basin empty) and, b) post-failure (storage basin filled) (data from LIDAR survey) and c) longitudinal and cross-sections of the DTMs pre- and post-failure.

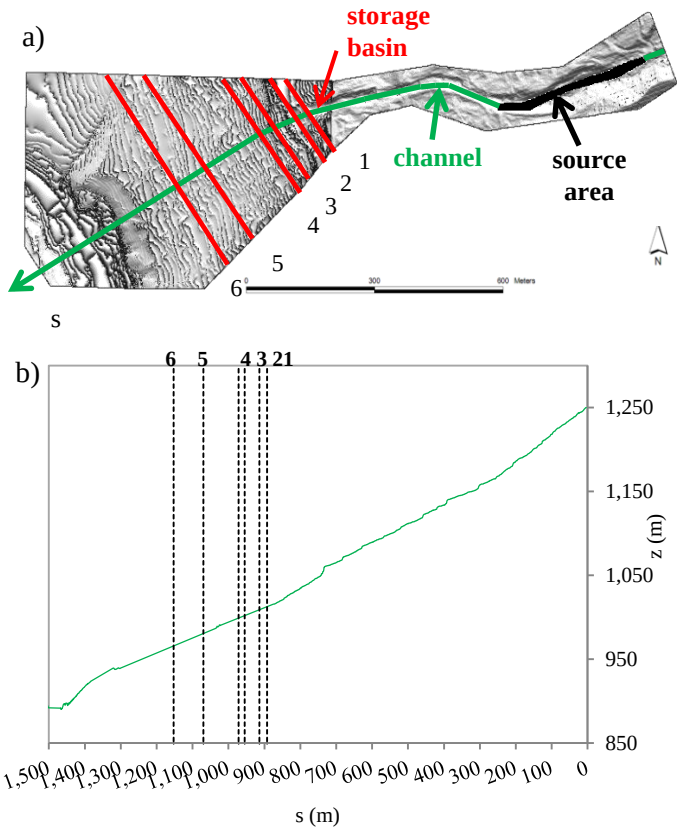

Figure 7.6 a) DTM used for the numerical modelling of the flows occurred in 1994 and 1996 (data from LIDAR survey), b) DTM longitudinal section.

The volume of soil accumulated inside the storage basins was evaluated comparing pre- and post-event topographic information, (Fig. 7.7a), and it resulted a total deposited volume of about 30,000 m3. The sediments deposited along a slope angle equal to 7-8° in the first storage basin, while 10-12° in the downstream basin (Fig. 7.7b). In particular, the presence of the building "1" promoted the accumulation of sediments mainly upstream of it, thus creating a depression downward it.

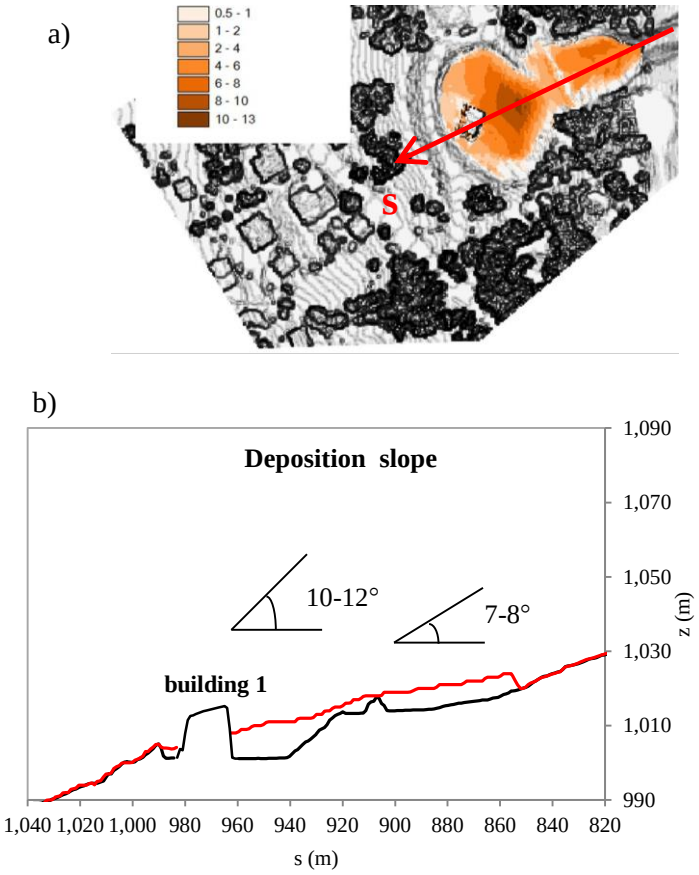

Figure 7.7 a) Plan-view extracted from DTM of Figure 7.5a of the deposition zone of the July 2009 flows, b) Longitudinal section and deposition slope.

Referring to the diagram in figure 7.3, the DF occurred on July 2009 (about 30,000 m^3, later used as input for the numerical modelling) had a frequency (F) equal to about 3×10^{-2}, corresponding a return period (T) of about 30 years (Fig. 7.3), that is in between low and high magnitude events.

On the contrary, the FF appears to be insignificant in comparison to volume mobilized by the DF, even though it appears comparable with that described by Ferretti (1995) for the event dated 1994. Anyway, the lack of data suggested referring to the rainfall data recorded at the rain gauge station of "Rovina Bassa di Cancia" (Fig. 7.8a), that recorded two peaks: the first peak was equal to 11.6 mm in 5 minutes (2:55 a.m.) and the second peak equal to 6.2 mm in 5 minutes (3:40 a.m.). These data were used as input data to implement a runoff model using the previously described DTM and the code MIKE 11-UHM. The water discharge (hydrograph) and the cumulative water volume computed at the catchment outlet (Fig. 7.8b,c) were equal to: i) about 25,000 - 30,000 m^3 from 1:50 a.m. to 3:40 a.m.; ii) about 1,500 m^3 from 3:40 a.m. to 4:00 a.m. Only a part of the first water volume (30,000 m^3) contributed to the first event (DF), while the second amount of water (1,500 m^3) was assumed as the magnitude of the second one (FF), considering the low percentage of sediment inside (Cascini et al., 2017; Rendina et al., 2017).

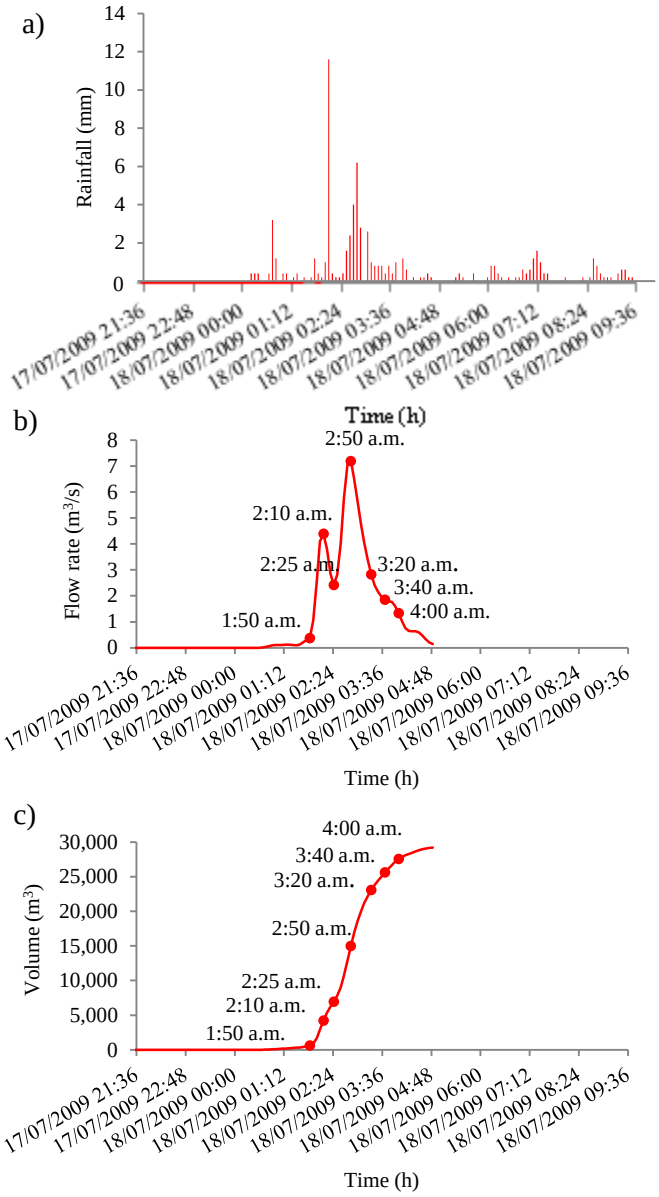
a)
Rainfall (mm)
14
12
10
8
6
4
2
0
17/07/2009 21:36
17/07/2009 22:48
18/07/2009 00:00
18/07/2009 01:12
18/07/2009 02:24
18/07/2009 03:36
18/07/2009 04:48
18/07/2009 06:00
18/07/2009 07:12
18/07/2009 08:24
18/07/2009 09:36
Time (h)
b)
Flow rate (m3/s)
8
7
6
5
4
3
2
1
0
2:50 a.m.
2:10 a.m.
2:25 a.m.
3:20 a.m.
3:40 a.m.
4:00 a.m.
1:50 a.m.
17/07/2009 21:36
17/07/2009 22:48
18/07/2009 00:00
18/07/2009 01:12
18/07/2009 02:24
18/07/2009 03:36
18/07/2009 04:48
18/07/2009 06:00
18/07/2009 07:12
18/07/2009 08:24
18/07/2009 09:36
Time (h)
c)
Volume (m3)
30,000
25,000
20,000
15,000
10,000
5,000
0
4:00 a.m.
3:40 a.m.
3:20 a.m.
2:50 a.m.
2:25 a.m.
2:10 a.m.
1:50 a.m.
17/07/2009 21:36
17/07/2009 22:48
18/07/2009 00:00
18/07/2009 01:12
18/07/2009 02:24
18/07/2009 03:36
18/07/2009 04:48
18/07/2009 06:00
18/07/2009 07:12
18/07/2009 08:24
18/07/2009 09:36
Time (h)

Figure 7.8 a) Rainfall data recorded at rain gauge station of Rovina Bassa di Cancia, runoff computed at the catchment outlet b) water discharge (hydrograph) and c) cumulative volume of water. (data from Cascini, 2011).

The modelling of the propagation of the flows was developed not doing any specific analysis of the triggering stage neither for the debris flows nor for the flash floods occurred at the site area. This was a precise choice to focus on the propagation stage and on the analysis of the kinematical features of distinct flows, considering that the literature already proposes many analyses of the triggering mechanisms for rainfall-induced flows (Cascini et al., 2014; Cuomo et al., 2014, among others). Particularly, the initial height of the flowing mass within the source areas of Figures 7.5 and 7.6 was simply obtained dividing the volume by the area of the triggering zone.

As it concerns the rheological parameters Equations 7.1-7.3 were calibrated and validated through a back-analysis of past events; in particular the simple frictional-type rheological model (Equation 7.2) has been used for 1994 and 1996 events. The same rheological model is used for modelling of DF and FF events of July 2009 and based on deposition slope of the material inside the storage basins and the traces inclination on the both buildings "1" and "2", the friction angle has been changed from 5° to 10°. Later, a frictional-type model with internal pore water pressure (Equation 7.3) is used to describe the DF behavior (Cascini et al., 2017; Rendina et al., 2017).

7.3 RESULTS

7.3.1 Model calibration

Based on the literature (Ferretti, 1995; Bacchini and Zannoni, 2003), the event dated 1994 was considered similar to that occurred on 2009, so assuming 30,000 m3 and 1,500 m^3 for the volume of debris flow (DF) and flash flood (FF), respectively. The sequence of these two events seems to be confirmed by the shape of the alluvial fan in Figure 7.2 showing an area where a concentrated mass stopped in the upper part of

the slope and another one elongated downslope. Indeed, the DF was modelled referring to the DTM of Figure 7.6, which was later modified adding the volume deposited by the DF to perform the modelling of the FF. As it concerns the event dated 1996, not being available further information in the literature, it was assumed that a unique DF event having a total volume of 60,000 m^3 created the alluvial fan in Figure 7.2. The DTM source area of the mobilized materials for all these cases study was located as shown in Figure 7.6. Finally, the simple frictional-type rheological model (Equation 7.2) was applied to a vast series of numerical simulations changing the friction angle from 6° to 9°, each 0.2°. The best obtained results are shown in Figures 7.9 and 7.10 for the 1994 and 1996 events, respectively.

Figure 7.9a highlights that an equivalent friction angle of 8° is able to back-analyse the DB dated 1994 while a friction angle of 7.2° reproduces the maximum run-out distance of the following FF even though the numerical alluvial fan is larger than that proposed in the literature; this is probably due to a modification of the site after the DF that is not properly reproduced by implementing the DTM through the previously explained procedure. For the event occurred in 1996, the best-fitting of the alluvial fan in the literature is given by a friction angle of 7° (Fig. 7.10a), while in correspondence of a 8° friction angle value the volume essentially stops not so far from the storage basin located in the upper part of the slope.

Considering the poor data available in the literature, further insights on these cases study cannot be obtained through current practice while their understanding is facilitated by the Figures 7.9b and 7.10b, which compare the Froude number computed for both events at significant time lapses from the triggering. Particularly, 6 specific time lapses were selected corresponding to the arrival of the front part of the flows to the sections 1-6, located at distances equal to 557-818 m from the lowermost point of the source area. Then, the frequency of all the SPH computational points (n_{tot} = 5040) into 25 classes (0-1, 1-2, etc.) of Froude number was computed and plotted for each simulation (Figs 7.9b, 7.10b.). Moreover, the average velocity ($\overline{v}$) was computed as the

run-out distance (travelled by the lowermost point of the source area) divided by the elapsed time.

Figure 7.9b evidences that the 1994 event had Froude number lower than 5-6 for DF, while higher for FF. On the contrary, figure 7.10b shows that the 1996 event had average values of Fr lower than 10-12.

However, the reduction of Froude, the progressive narrowing of plot and the final bimodal shape of the Froude plot are analogous for both events. Thus, Froude number was newly used as descriptor of the kinematical behaviour of the flows and substantial differences were outlined for the two events (mainly due to their different volume) with similarities during some intervals of the propagation stage. It is also worth mentioning that while the average velocity is monotonically decreasing in both cases, Froude number had different evolution in time, clearly depending on the temporal-spatial evolution of the propagation heights, in turn related to both initial volume and rheology (being the topography the same for the two events). What appears relevant is that while each variable among those mentioned above gives useful information about the flows, the Froude number is able to provide a unique overall description (Cascini et al., 2017; Rendina et al., 2017).

Globally, the numerical results highlight that the solid-water mixture had very low friction angles, and comprised in a very narrow interval, 7° to 8° passing from FF to a DF. Thus, the above results newly evidence that interstitial water played a paramount role into reducing the strength mobilised into the sandy-gravelly solid fractions of the flows occurred at the study area. While, this mechanism have been thoroughly analysed for silty-sandy materials (Cascini et al., 2013, 2016), this work proposes new insights for a context like Alps where dry granular flows have been more studied (Tecca et al., 2003).

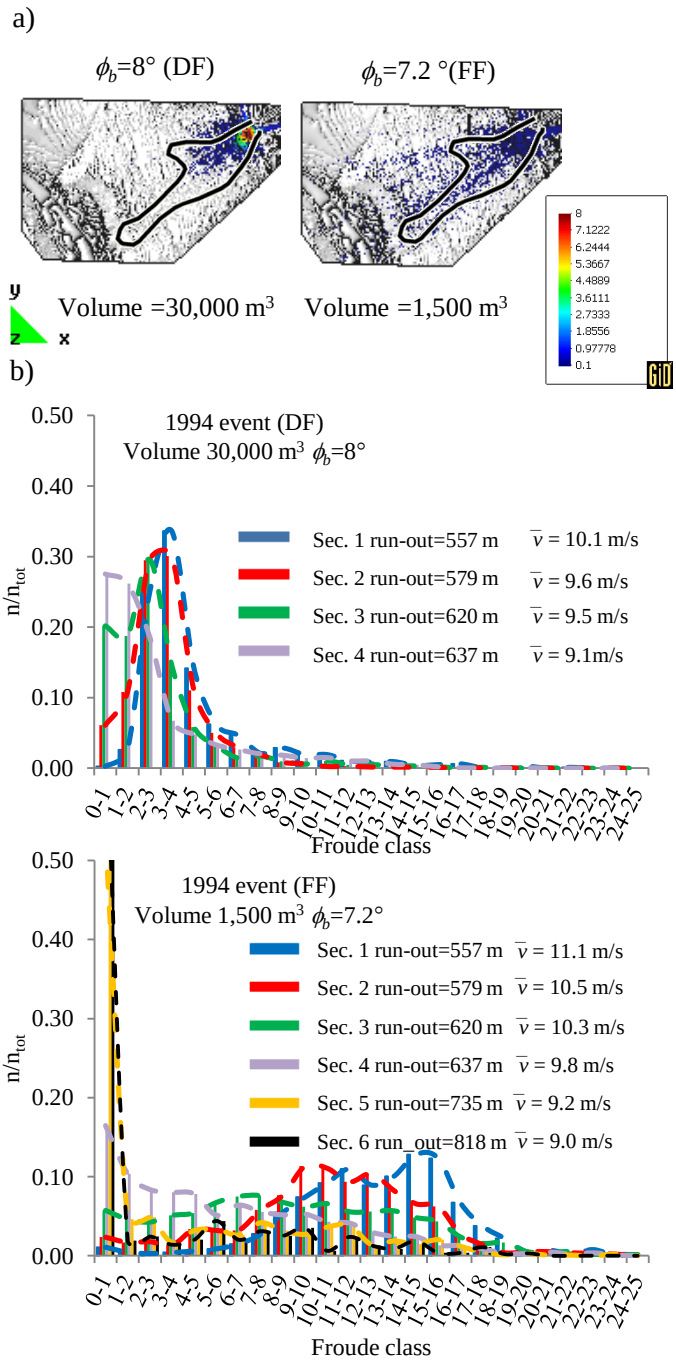
a)
ϕ_b=8° (DF)
ϕ_b=7.2 °(FF)
Volume =30,000 m³
Volume =1,500 m³
8
7.1222
6.2444
5.3667
4.4889
3.6111
2.7333
1.8556
0.97778
0.1
b)
1994 event (DF)
Volume 30,000 m³ ϕ_b=8°
Sec. 1 run-out=557 m $\bar{v}$ = 10.1 m/s
Sec. 2 run-out=579 m $\bar{v}$ = 9.6 m/s
Sec. 3 run-out=620 m $\bar{v}$ = 9.5 m/s
Sec. 4 run-out=637 m $\bar{v}$ = 9.1m/s
n/n$_{tot}$
Froude class
1994 event (FF)
Volume 1,500 m³ ϕ_b=7.2°
Sec. 1 run-out=557 m $\bar{v}$ = 11.1 m/s
Sec. 2 run-out=579 m $\bar{v}$ = 10.5 m/s
Sec. 3 run-out=620 m $\bar{v}$ = 10.3 m/s
Sec. 4 run-out=637 m $\bar{v}$ = 9.8 m/s
Sec. 5 run-out=735 m $\bar{v}$ = 9.2 m/s
Sec. 6 run_out=818 m $\bar{v}$ = 9.0 m/s
n/n$_{tot}$
Froude class

Figure 7.9 a) Deposition thickness simulated for the 1994 events (DF and FF) with different rheological parameters; the black line represents the boundary of deposit observed in the field; b) frequency distribution of the Froude number computed within the SPH computational points (ntot = 5040) used for 1994 and 1996 events, at the time lapses when the flows reached the target run-out distances (i.e. cross-sections 1-6 of Figure 7.6).

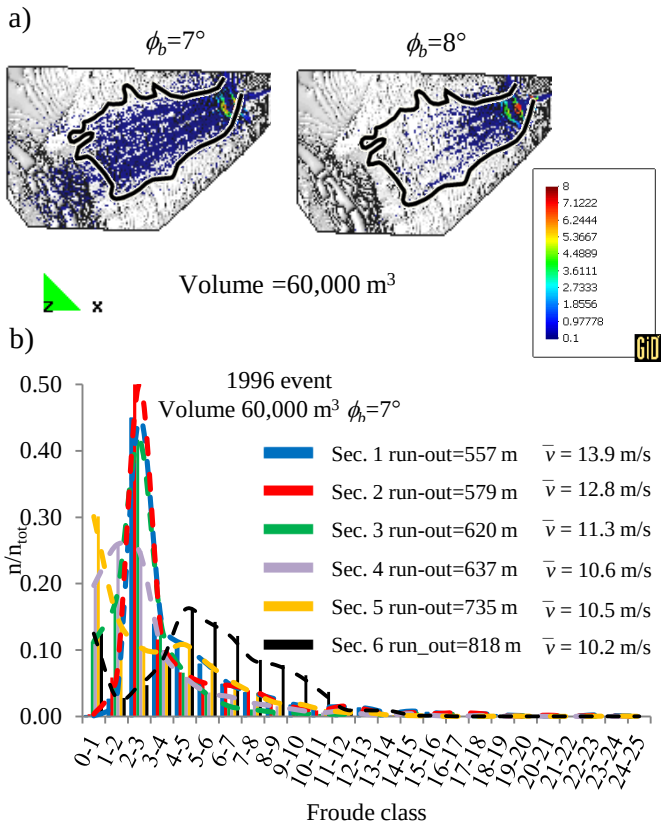

Figure 7.10 a) Deposition thickness simulated for the 1996 event with different rheological parameters; the black line represents the boundary of deposit observed in the field; b) frequency distribution of the Froude number computed within the SPH computational points (n_{tot} = 5040) used for 1994 and 1996, at the time lapses when the flows reached the target run-out distances (i.e. cross-sections 1-6 of Figure 7.6).

7.3.2 Modeling of the 2009 events

Two series of numerical analysis were performed to simulate: i) the propagation of a 30,000 m^3 debris flow with the two storage basins assumed empty (SBE), ii) the propagation of a 1,500 m^3 flash flood assuming the storage basin empty (SBE) or filled by debris (SBF) as observed after the events (Section 7.2.2). The numerical analysis of the 2009 debris flow (DF) was firstly developed by means of a frictional-type model (Equation 7.2) and then by implementing a frictional-type model with internal pore water pressure (Equation 7.3), where pore water pressure was a time-and space-dependent variable (Cascini et al., 2014, 2016; Cuomo et al., 2014, 2016). The propagation of the flash flood (FF) was firstly carried out through a frictional-type model (Equation 7.2) and then by using a Chezy-Manning model (Equation 7.1). The choice of the rheological model was based on both the analysis of the calibration events (1994 and 1996) and the suggestions provided by the extensive literature on the topic (Pastor et al., 2014, among others). The list of the most significant numerical cases is reported in Table 7.2, while the results of those best fitting the field evidence are shown in Figures 7.11 for DF and in Figure 7.12 for FF.

Table 7.2 List of numerical cases analysed for the back-analysis of the 2009 events.

Case	Site condition	Flow type	Volume (m^3)	Rheological models	m ($s\ m^{-1/3}$)	ϕ_b (°)	h_w^{rel} (-)	p_w^{rel} (-)	c_v ($m^2\ s^{-1}$)
1		DF	30,000	Frict	-	10	-	-	-
2a		DF	30,000	Frict	-	8	-	-	-
2b		DF	30,000	Frict	-	7	-	-	-
5	SBE	DF	30,000	Frict+PWP	-	22	0.4	1	10^{-4}
6		DF	30,000	Frict+PWP	-	22	0.4	1	10^{-2}
7		DF	30,000	Frict+PWP	-	22	0.6	1	10^{-2}
8*		DF	30,000	Frict+PWP	-	17	0.6	1	10^{-2}
9-13	SBF	FF	1,500	CM	from 0.005 to 0.015	-	-	-	-
3	SBE	FF	1,500	Frict	-	5	-	-	-
4*	SBF	FF	1,500	Frict	-	7	-	-	-

ϱ: mixture density equal to 11.21 kN m^{-3}, ϕ_b: basal friction angle, h_w^{rel}: relative water height, p_w^{rel}: ratio of pore water pressure to liquefaction pressure; c_v: consolidation coefficient, m: Manning number, SBE (Storage Basin Empty), SBF (Storage Basin Filled), DF: debris flow, FF: flash flood and CM: Chezy-Manning rheology; *best fitting of the in-situ evidences.

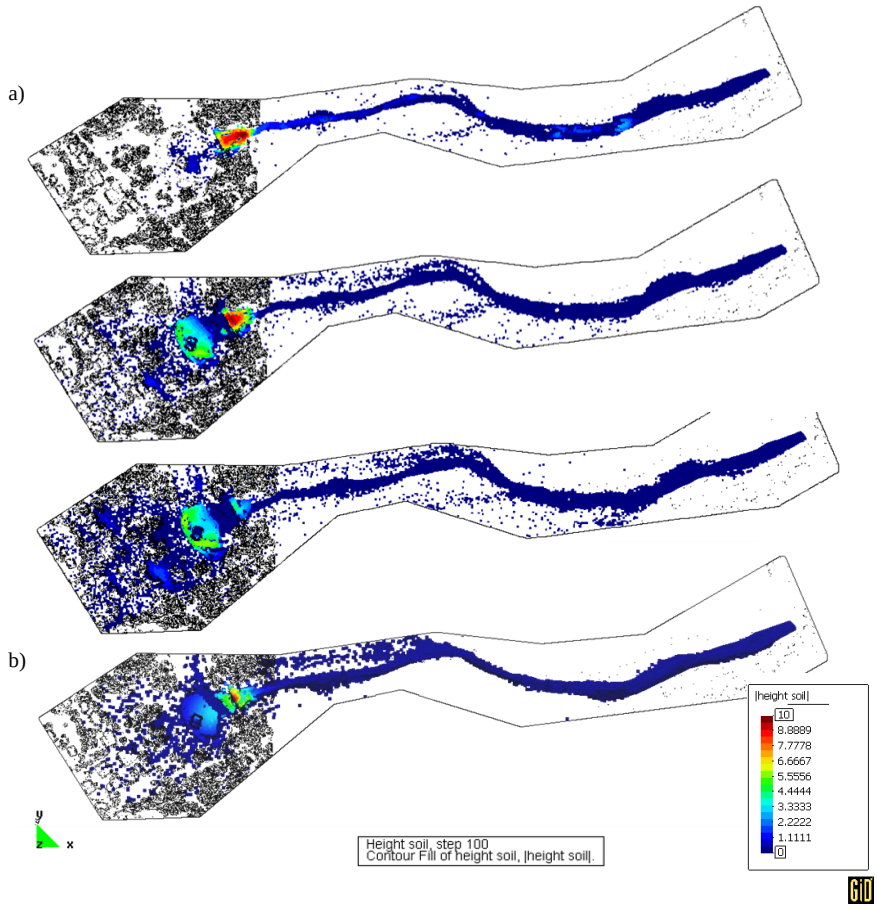

Figure 7.11 a) Final deposition thicknesses computed for the 30'000 m³ DF (scenarios 1, 2a, 2b of Table 7.2) propagating inside the Storage Basin Empty (SBE) and simulated through a frictional-type model. b) Scenario 8 of Table 7.2 propagating inside the Storage Basin Empty (SBE) and simulated through frictional-type model with internal pore water pressure.

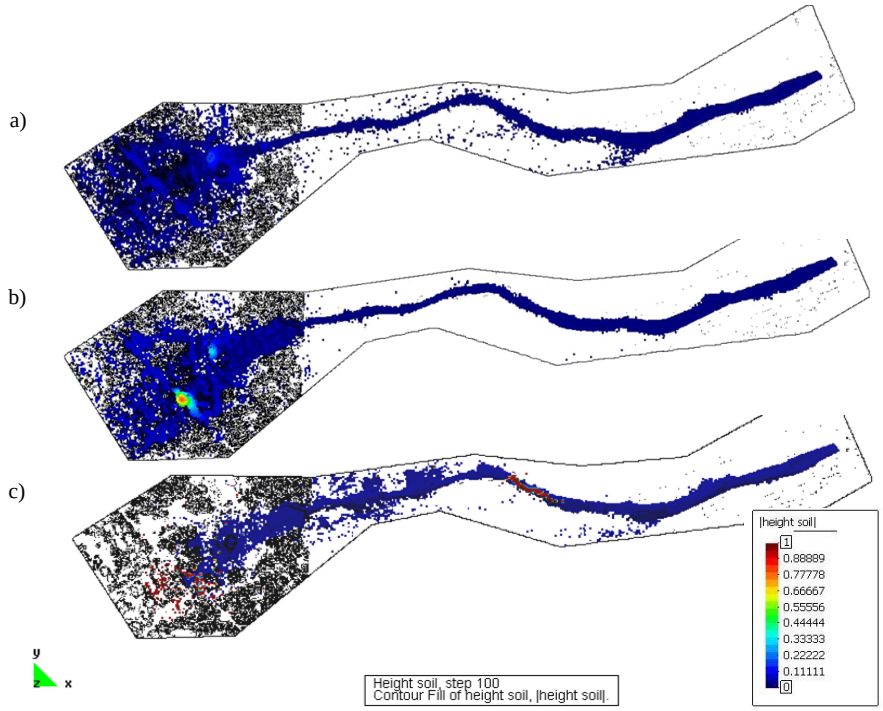

Figure 7.12 Final deposition thicknesses computed for the 1,500 m³ FF scenarios 3-4 of Table 7.2 propagating inside the a) Storage Basin Empty (SBE) or b) Storage Basin Filled (SBF), both simulated through frictional-type model. c) Scenario 13 of Table 7.2 propagating inside the Storage Basin Filled (SBF) and simulated through Chezy-Manning model.

The numerical results of the cases 8 and 4 satisfactorily reproduced the in-situ evidence for both the run-out distance and the extent of deposition zone, Figures 7.11 b and 7.12 b. In particular, the scenario 8 (DF) provided the most adequate deposition thicknesses in the both storage basins reaching deposition height (about 4,00 m) in the upstream zone of the building "1", while heights up to 1,0 m in the downstream zone. The deposition heights are distinctive of a slow flow, which stops mainly in the first storage basin and partially in the upstream of the second storage basin. The slope angles of deposit well resemble those measured in the basin at 1,013 m a.s.l, then are steeper and decrease again in the second basin (Fig. 7.13 a). As for the flash flood modelling, only the frictional-type model (Case 4) was able to reproduce the

deposition thickness near to building labelled as "2"of Figure 7.4. The low deposition heights and the flow traces on the building "2" (Fig. 7.13 b) are distinctive of a rapid flow that resulted in a vertical jet mechanism as defined from Choi et al. (2015). It is also worth noting that the simulated FF overpassed both the storage basins (so hitting the building "2") independent on the storage basin state: empty (scenario 3) or filled of soil (scenario 4).

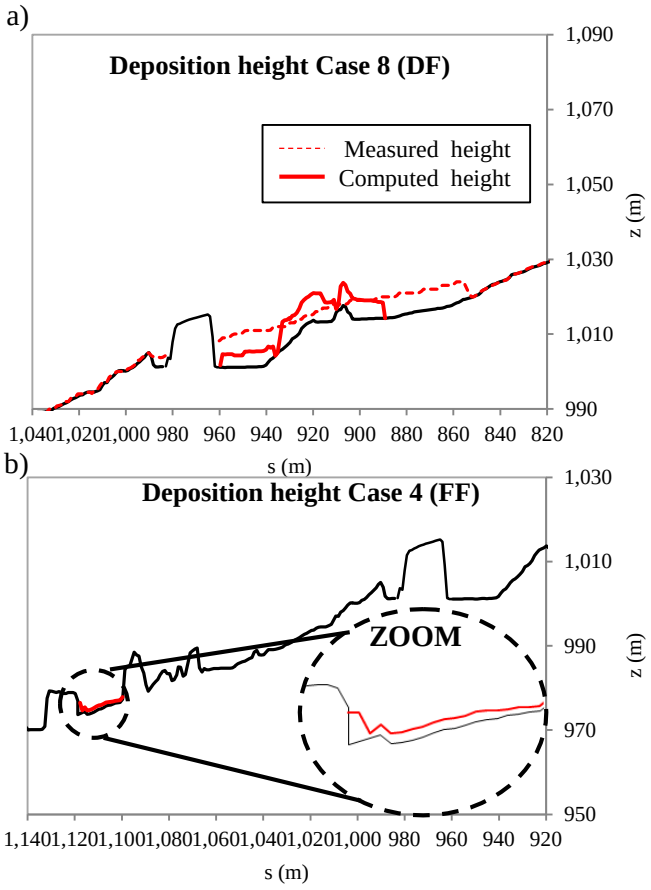

Figure 7.13 a) Longitudinal section and deposition height of DF (Case 8 of Table 7.2) b) Longitudinal section and deposition height of FF (Case 4 of Table 7.2).

The plots of Figure 7.14 clearly show that the FF had always Froude number higher than the DF. In the case of the FF, the Froude distribution curve mostly shifted to left in time, while for the DF the relative distribution shifted to the left and also changed in shape. This latter effect was clearly due to the interaction of the DF with the storage basin. Related to that, it is worth noting that when the run-out distance travelled by the DF reached 637 m (at section 4, along building "1"), the most of points had very low Froude number. This means that the DF had turned to a "subcritical flow", having been before a "supercritical flow". On the contrary, the FF kept high value of the Froude number all over the process, behaving as a "supercritical flow".

One further consideration was also added to deepen the differences between the two flows (DF and FF). The average velocity of FF was higher than DF: 14.2-18.6 m/s versus 12.7-15.9 m/s, respectively. The difference in average velocity contributed to the different Froude number for FF and DF, but also the heights were evidently important. Other factors such the difference in volume (1,500 m^3 versus 30,000 m^3, respectively), the different initial heights in the source area (5.96 m versus 0.30 m, respectively), and the specific features of DTM contributed to the magnitude of difference in Froude number, being the latter depending on time-spatial-distributed variables such propagation height (h) and velocity (v) (Cascini et al., 2017).

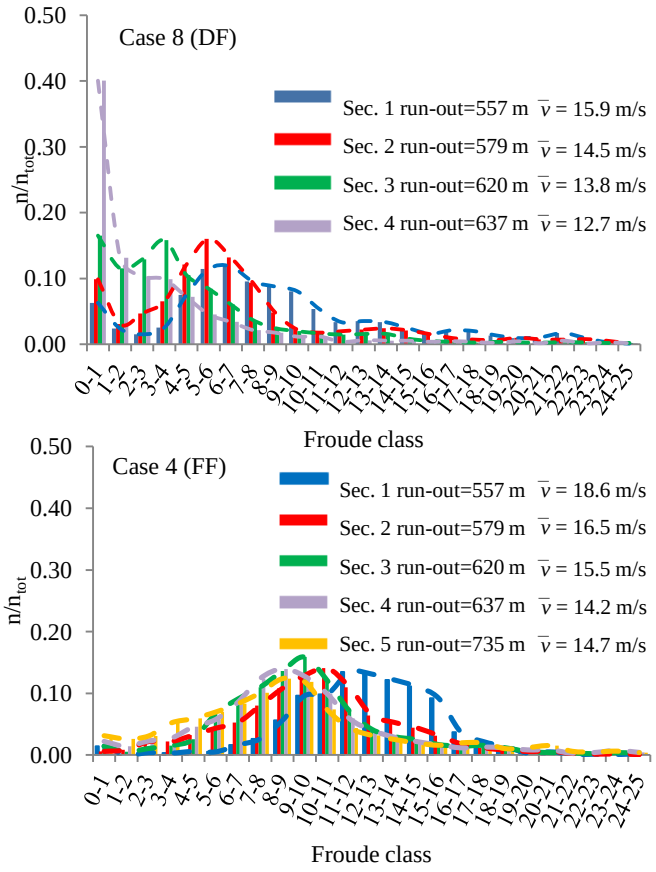

Figure 7.14 Frequency distribution of the Froude number computed within the SPH computational points (n_{tot} = 5040) used for DF and FF (2009 event), at the time lapses when the flows reached the target run-out distances (i.e. cross-sections 1-5 of Figure 7.5).

7.4 DISCUSSION

A combination of different flow-type mass movements occurring during the same critical rainfall event my cause unexpected flow propagation

patterns. This chapter deals with a peculiar case history from the Italian Dolomite Alps where, despite the presence of two storage basins, a combination of a large debris flow and a small flash flood was finally able to produce damage and victims down slope the control works.

This weak protection system was firstly analysed through the SPH numerical model referring to high-quality DTMs (Digital Terrain Models), and accurate field evidences regarding both the topography, types of materials and eyewitnesses of the occurred events. The numerical results pointed out that the observed behaviour of debris flow (DF) is adequately reproduced through a frictional rheological model (averaged behaviour of solid skeleton and pore water pressure) or considering the pore water pressure as an added variable. Whereas, the best-fitting numerical simulation of the field evidence for flash flood (FF-flow) is obtained through a frictional rheological model while not by using the Chezy-Manning rheological model, which disregards the presence of solid material in the flow.

The different performance of control works against DF and FF was then investigated through the analysis of the kinematical features of the flows, by introducing the Froude number (*Fr*). Referring to the events dated 1994, 1996 and 2009 events, the numerical results highlight that i) the higher the Froude number, the lower is the potential efficacy of any control work mainly aimed to reduce the velocity of the flow, ii) the more the distribution of Froude number within the flowing mass (i.e. distribution of the Froude number classes for the computational points) changes during the propagation stage, the more the topography and/or control works are effective to change the flow from supercritical to subcritical, or vice versa, iii) a specific example of a control work properly working is the 30,000 m^3 sized debris flow (occurred while the storage basin was empty), which had a change in the Froude number from very high to very low, iv) a specific example of flow insensitive to topography and control work is the 1,500 m^3 sized flash flood (occurred while the storage basin was full of solid), which did not have any significant change in the Froude number.

It could be concluded that Froude number can be usefully used in control works design even though, in the case of mixtures of solid material and water, *Fr* is a spatial- and temporal-dependent quantity, even much affected by local topography, flow rheology and the presence

of eventual obstacles and/or control works. It is also worth mentioning that the volume of solid-water mixture flows may span from few to hundreds of thousands of cubic meters and, consequently, the local velocities and heights of the flow are highly variable, and similarly do the Froude number.

Indeed, there is a relevant open issue related to the individuation of those range of Froude number corresponding to a supercritical (rapid-like) or subcritical (slow-like) behaviour of solid-water mixture flows and this topic deserves more extensive research. Other relevant factors deserving a proper in-depth analysis are the 3D effects, while one important limitation of the present work is mainly related to the use of a depth-integrated propagation model. Such limitations could be removed by using 3D models especially in the cases where the detailed description of the interaction of flows against structures is of interest (Cascini et al., 2017).

8 EXISTING STORAGE BASINS

In May 1998, tens of flow type landslides were triggered and travelled down to the towns of Bracigliano, Quindici, Sarno and Siano, located at the toe of the Pizzo D'Alvano massif (Cascini et al., 2014). Since 2000, overall, 35 storage basins with capacity of approximately two million m^3, more than 120 check dams and channels with total length of about 26 km were built and restructured to protect people and property (Versace, 2008). In order to analyze the protection system, the "Tuostolo" mountain basin (Sarno zone) was selected as testing case . The propagation stage was performed through the SPH model using as input data a 3x3 m DTM of the sites in 1999 and a 1x1 m DTM of the sites in 2011 including the control works. Furthermore, considering the field evidence after the '98 events and the studies about triggering mechanisms carried out by Cascini et al. 2003, Cascini et al., 2005 and Cascini et al., 2008, some hypotheses about the magnitude of possible future events were assumed.

As previously done in Chapter 7, this topic is tackled referring to the Froude number, which highlighted the effectiveness of passive control works when all components of protection system are operational.

8.1 Case study

8.1.1 Site description and the May 1998 events

The study area is located in the Campania region, where in 1998 two million m^3 of material were mobilized in the Pizzo D'Alvano massif (Fig. 8.1).

The massif extends for about 75 km^2 and reaches the maximum altitude of 1,200 m a.s.l. (Versace, 2008). The average slopes are about 30-35° in the upstream zone, while they are minor of 20° in the downstream zone. However, the slopes are influenced by structural factors (minor faults and jointing) as well as by morphological frames derived from limestone layers more resistant to erosion (Cascini et al., 2003).
As it concerns the geological features, the massif consists of a sequence of limestones, dolomitic limestones and marly-limestone rocks (Fig. 8.2). The pyroclastic soils, originating from the explosive activity of the Somma-Vesuvius volcanic apparata, cover the limestone layers (Cascini et al., 2011) with a thickness ranging from 0 to 5 m. The Figure 8.3 shows the hydrogeological features and the main structural elements. The massif structure is highly fractured and karsified with a suspended groundwater flow system mainly located in the upper part of the slopes (Cascini et al. 2008).

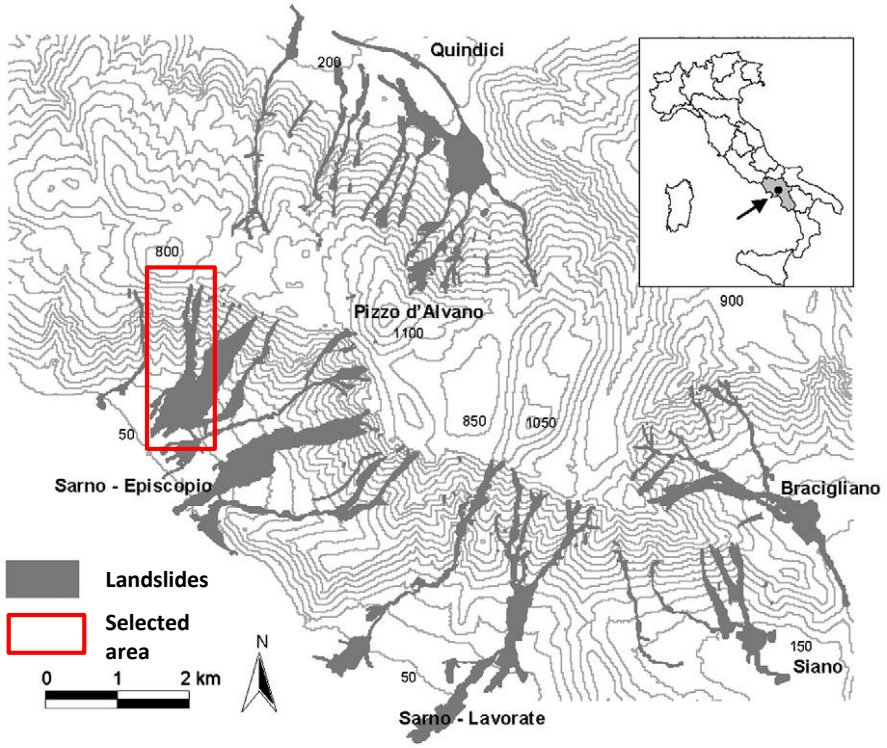

Figure 8.1 Overview of the 1998 Pizzo D'Alvano landslides and location of the selected area (modified from Cascini et al., 2011).

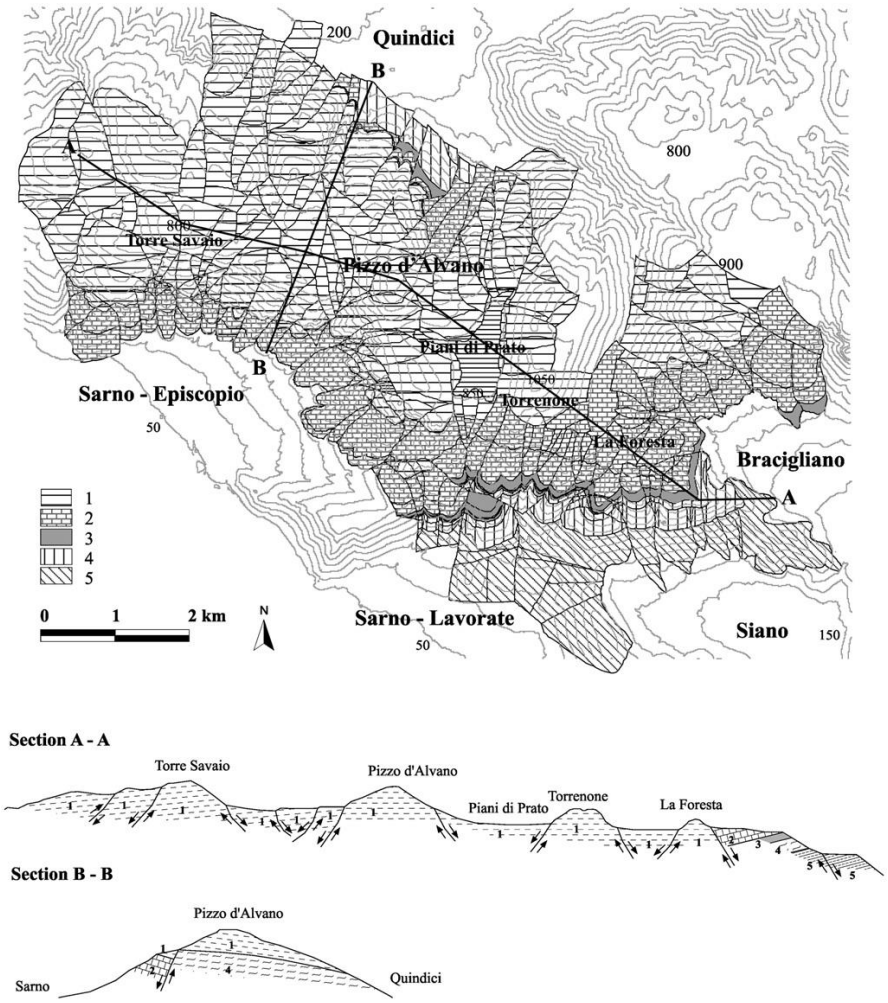

Figure 8.2 Geological map of Pizzo D'Alvano massif: 1) calcarenites and calcirudites (Upper Cretaceous), 2) calcarenites, calcilutites and dolomitized limestone (Middle-Upper Cretaceous), 3) marly limestone (Middle Cretaceous), 4) microcrystalline limestone partially dolomitized (Lower-MiddleCretaceous), 5) dolomized limestone (Lower Cretaceous) (Cascini et al., 2008).

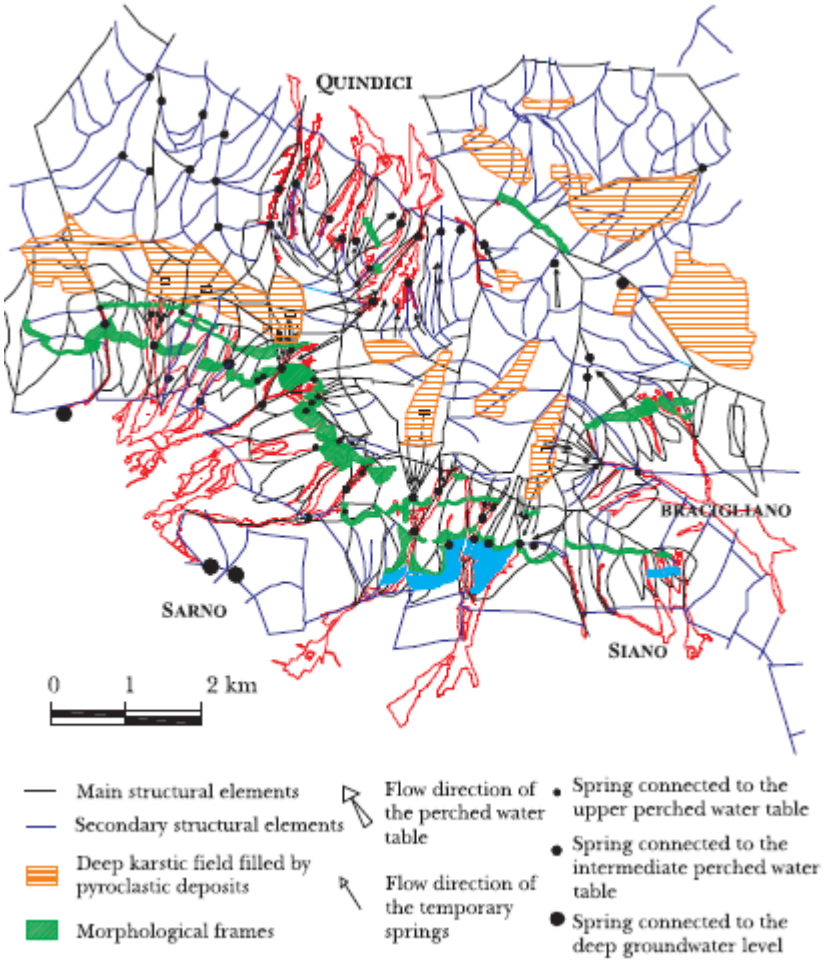

Figure 8.3 Hydro-structural map of Pizzo D'Alvano massif (Cascini et al.,2008).

The Tuostolo basin was selected since it is one of the most complex systems of passive control works built after the 1998 events and the main purpose of this chapter is to analyze its performance.

In 1998, two landslides were triggered at altitudes of 500–700 m a.s.l. with an initial volume of about 50,000m^3 and a total volume (sum of the initial volume and the entrained material) equal to 70,000m^3 (Cascini et

al., 2005). The triggering cause was related to the rainfall infiltration from the ground surface and water springs from bedrock (Cascini et al., 2014). The triggered masses joined in a channel with steep flanks and the whole mass travelled about 1500 m: 400 m in the channel and 1100 m in a flatter piedmont area (Fig. 8.4) (Cascini et al., 2014).

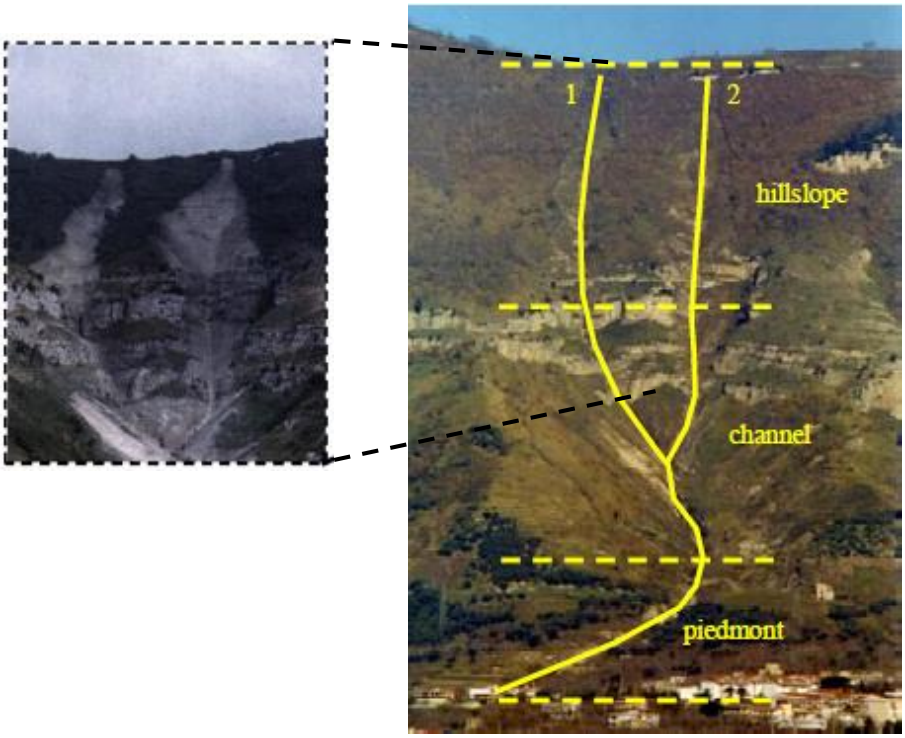

Figure 8.4 Overview of the "Tuostolo" mountain basin and 1998 landslides (Cascini et al. 2014).

During the propagation stage the mass was divided into two main branches at the apex of the piedmont zone and reached the Sarno town where eleven victims and about hundred damaged buildings were recorded. The Figure 8.5 shows a building that was carried by the flow for about 50 m.

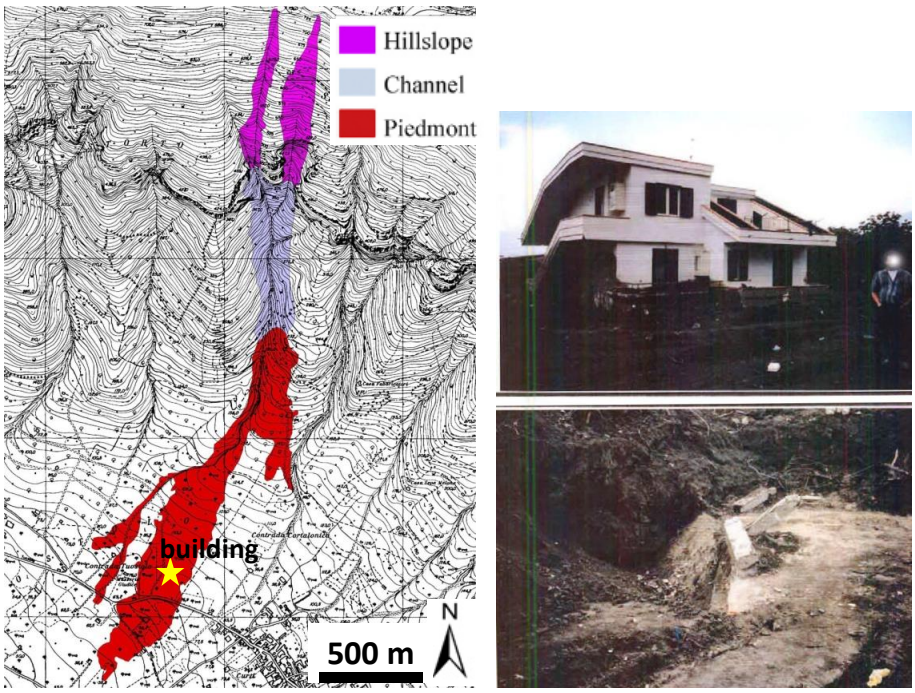

Figure 8.5 Morphological zoning and some effects of 1998 landslides (modified from Cascini, 2006).

8.1.2 The control works

After the catastrophic events of '98 channels, check dams and storage basins were built along the channels and at the toe of the slopes. The Figures 8.6 and 8.7 show the aerial photos of the Pizzo D'Alvano massif carried out in 1998 and 2010, respectively. In particular along the channel of the Tuostolo basin two check dams are located at 152 and 148 m a.s.l.. They are solid body dams with height equal to 5 m, width 20 m and with spacing equal to 30 m. The channel is located at 178 m a.s.l. with width of 4.80 and length of 567 m until the storage basin entrance. Two storage basins with a distance of 400 m were constructed to contain the flows from Tuostolo, Cortadonica and Trave basins. The first basin (located at 90 m a.s.l) is ovoid-shaped with storage capacity of approximately 200'000 m^3; the second consists of a smaller basin, of

triangular shape, located at 60 m a.s.l.. At the exit of the first storage basin, two check dams 10 m high are located to stop the coarser particles in the first basin and to allow the flow of the fine particles and water in the second basin (Fig. 8.8).

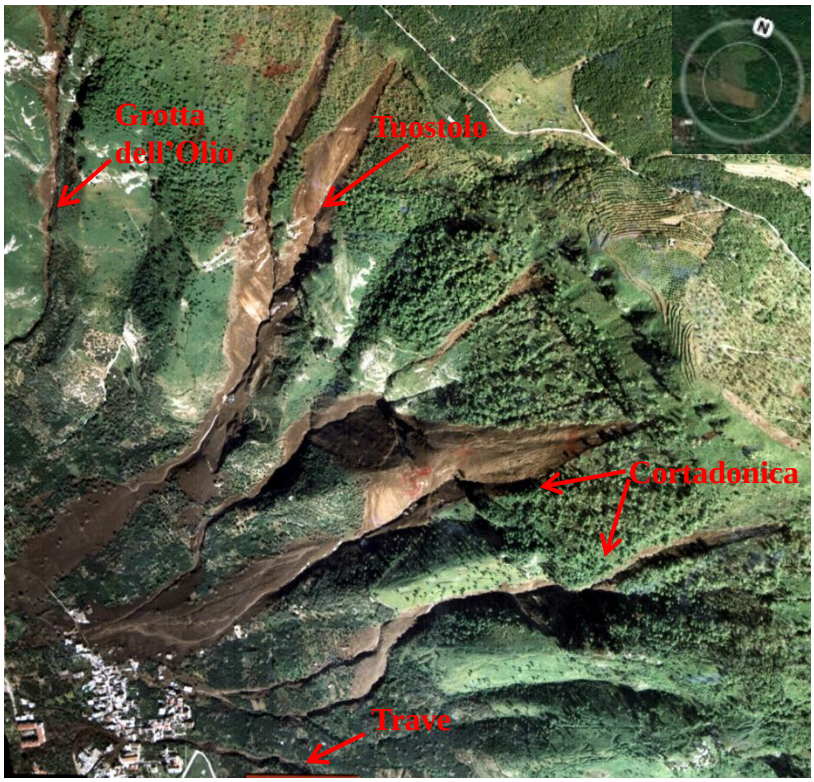

Figure 8.6 Overview of Pizzo D'Alvano massif just after the 1998 events (modified from Cascini, 2006).

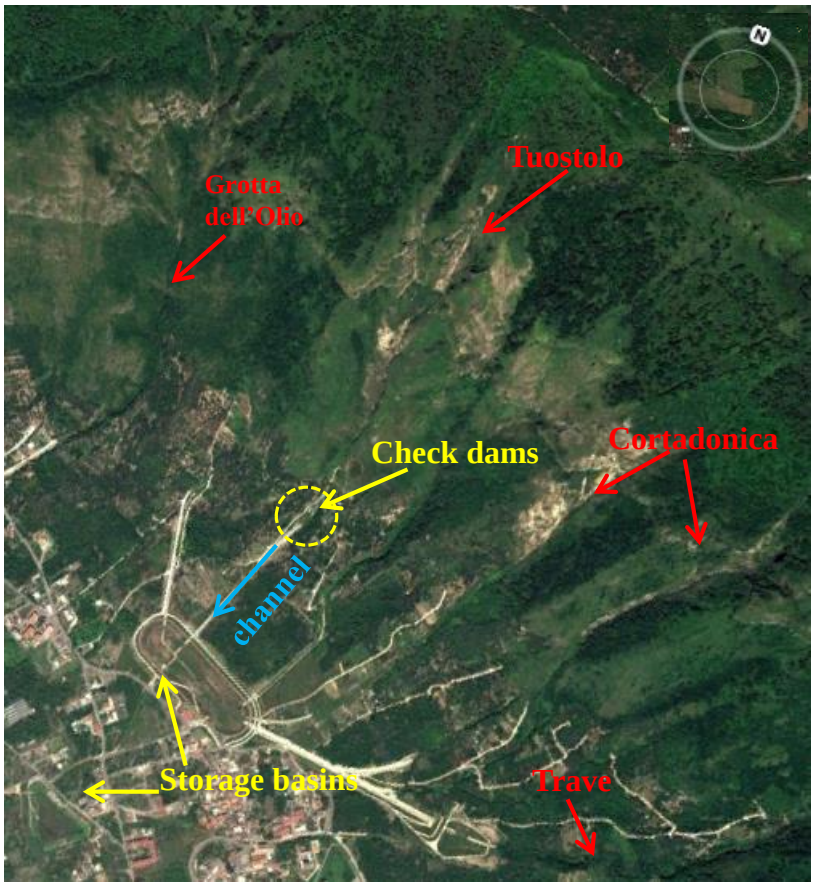

Figure 8.7 Overview of Pizzo D'Alvano massif with control works in 2010.

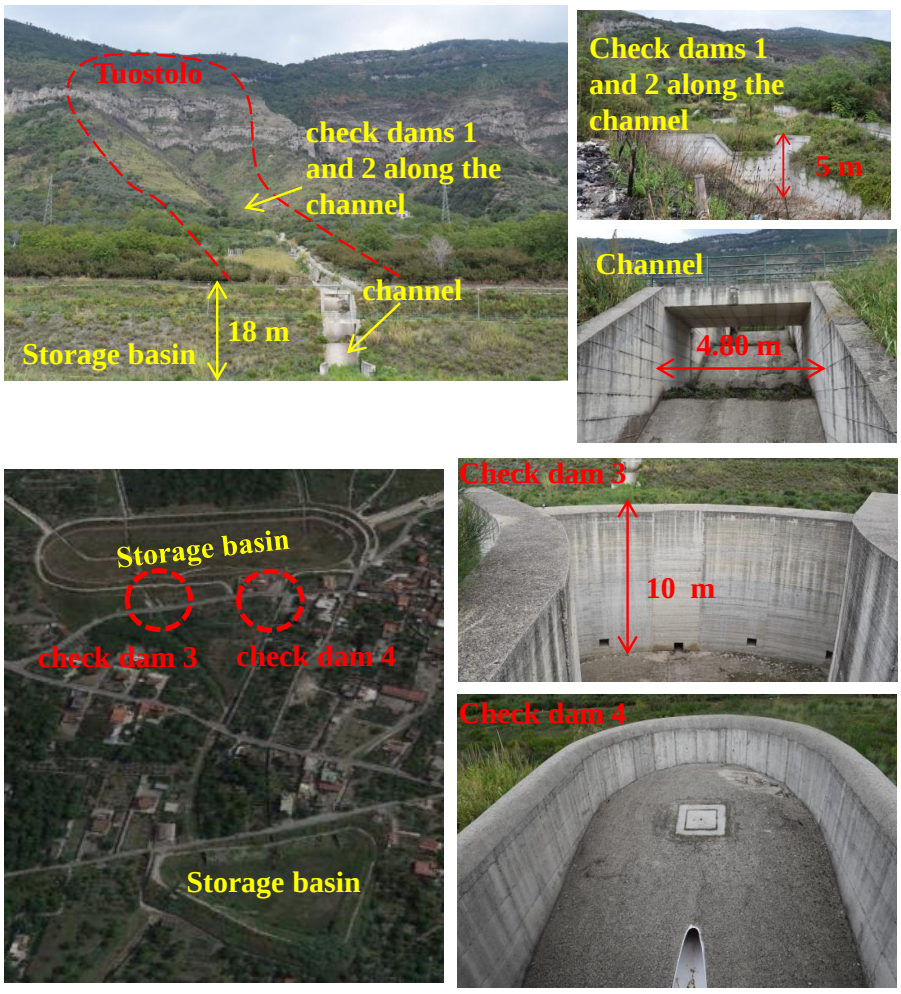

Figure 8.8 Overview of control works in Tuostolo basin.

8.2 NUMERICAL ANALYSIS

The numerical analysis is performed starting from:

- the modeling of triggering mechanisms as proposed by Cascini et al., 2003; Cascini et al., 2005 and Cascini et al., 2008;
- the satisfactory back-analysis of the propagation stage of the 1998 events as proposed by Cascini et al., 2014.

The triggering mechanisms in the Tuostolo basin (named "M1" in Cascini et al., 2005) occurred inside ZOBs (Zero Order Basins) affected by water supplies coming from the bedrock towards the pyroclastic covers. Zero order basins are colluvial hollows with a concave bedrock profile characterized by a maximum depth in the central part (Cascini et al., 2011). The extent of the triggering areas was estimated through the physically based models: SHALSTAB and TRIGRS (Cascini et al., 2003; Cascini et al., 2005 and Cascini et al., 2008).

SHALSTAB model overestimated the extension of triggering areas as it was not throughly capable to reproduce soil unsaturated conditions, variable stratigraphical settings and the presence of local boundary conditions (Cascini et al., 2005). On the other hand, TRIGRS model gave more satisfactory results because it considered different depths from the Map of pyroclastic deposits thickness (Fig. 8.9); different stratigraphic conditions arising from in-situ investigations (Fig. 8.10) and hydraulic parameters such as hydraulic conductivity, volumetric water content and diffusivity. The comparison between the provided results by two models is shown in Figure 8.11.

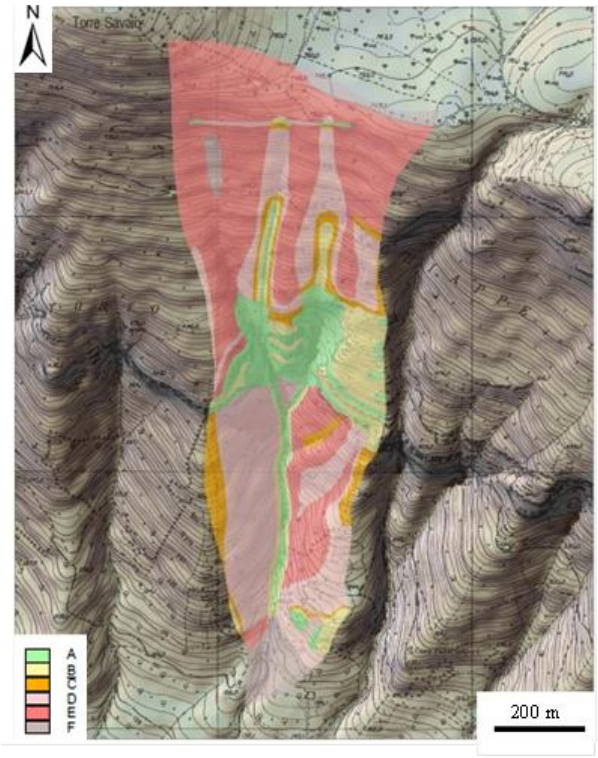

Figure 8.9 Map of pyroclastic deposits thickness: A) h=0 m, B) h<0.5 m, C) 0.5m<h<1m, D) 1m<h<2m, E) 2m<h<5m, F) h>5m) (modified from Cascini et al., 2006).

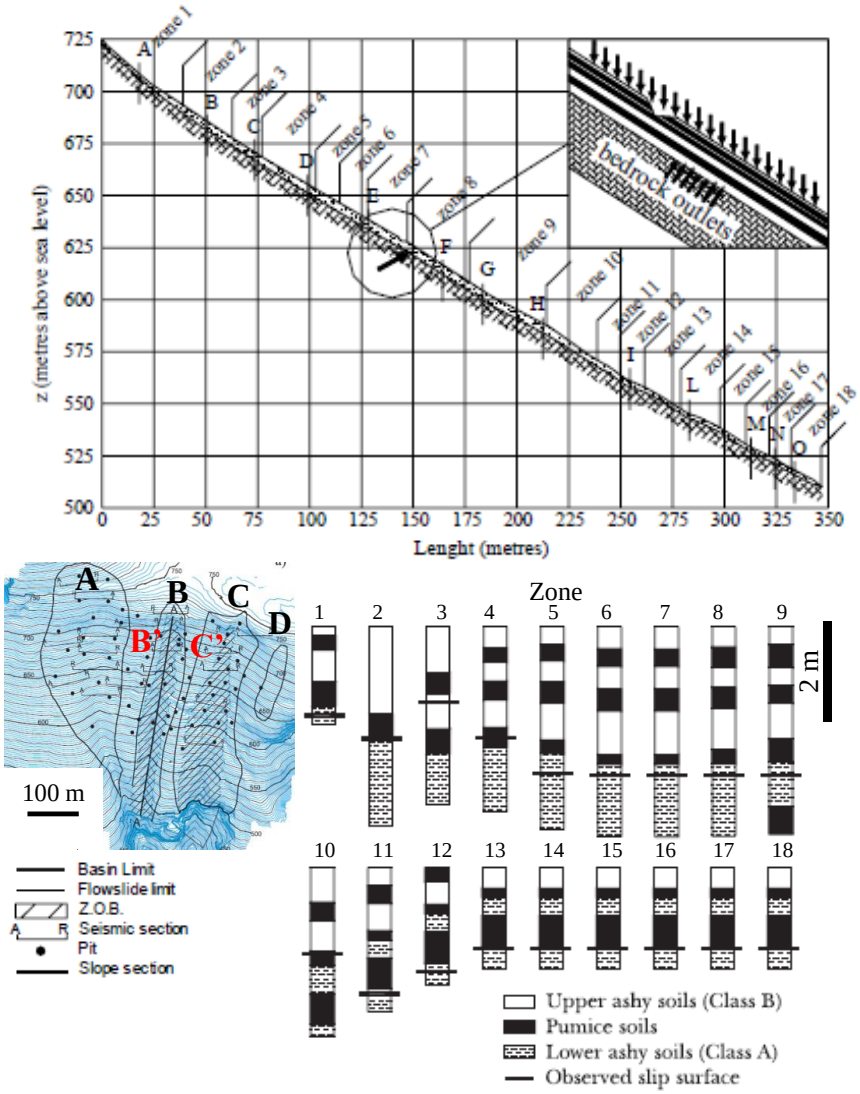

Figure 8.10 Overview of the in-situ investigations for the Tuostolo basin and stratigraphic characterization of the slope section (modified from Cascini et al., 2005).

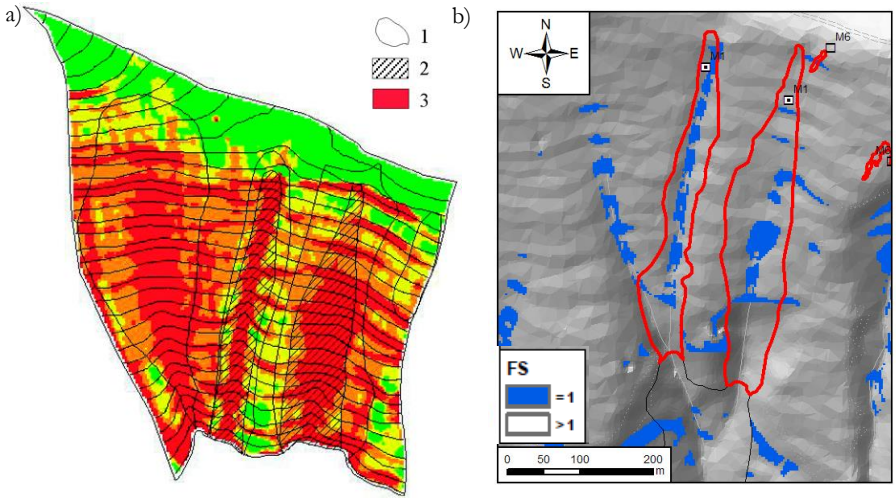

Figure 8.11 a) Output of the SHALSTAB code with reference to the May 1998 events in Tuostolo basin: 1) ZOB areas of the sample basin, 2) observed source areas, 3) simulated source areas (modified from Cascini et al., 2005). b) Output of the TRIGRS code (Sica, 2008).

The propagation stage of the 1998 events was analyzed in Cascini et al., 2014 with the mathematical model "GeoFlow_SPH" and the behavior of the flowing masses was implemented through the frictional-type model with internal pore water pressure (Equation 8.1):

$$\tau_b = -\left((1-n)(\rho_s - \rho_w)g\,h - p_w^b\right) tg\phi_b\, sgn(\bar{u}) \tag{8.1}$$

where τ_b is the basal shear stress of the flow, ρ_s is the solid grain density, ρ_w is the water density, g is the gravity acceleration, ϕ_b is the basal friction angle, n is the soil porosity, h is the propagation height, p_w^b is the excess of pore water pressure to hydrostatic, sgn is the sign function and $\bar{u}$ is the depth-averaged flow velocity. The erosion law proposed by Hungr (1995) was implemented to evaluate the bed entrainment along the landslide path.

As it concerns the input data of the Geoflow-SPH, a 3x3m DTM was used to reproduce the topographic conditions of the site; while the triggering volumes were obtained from detailed landslide inventory maps

and soil thickness maps (Cascini et al., 2005). The two landslides source areas of Sarno were discretized through 2936 and 4598 points and they were spaced at 3m at the beginning of the computation (Cascini et al., 2005). A large series of numerical simulations was performed changing the rheological parameters and landslide growth rates "E_r". The input parameters of the best fitting of the in-situ evidences were: basal friction angle (ϕ_b) equal to 22°, i.e. tan(ϕ_b) = 0.4; relative water height (h_w^{rel}, i.e. ratio of the height of the water table to the soil thickness) equal to 0.4; consolidation coefficient (c_v) equal to 1.0×10^{-2} m^2 s^{-1}; ratio of pore water pressure to liquefaction pressure (p_w^{rel}) equal to 1 and E_r=4.0×10^{-4} m^{-1} in the channel.

The Figure 8.12 shows the source areas on a 3×3 DTM and the best fitting the observed run-out distance and propagation path of the 1998 event carried out by Cascini et al., 2014.

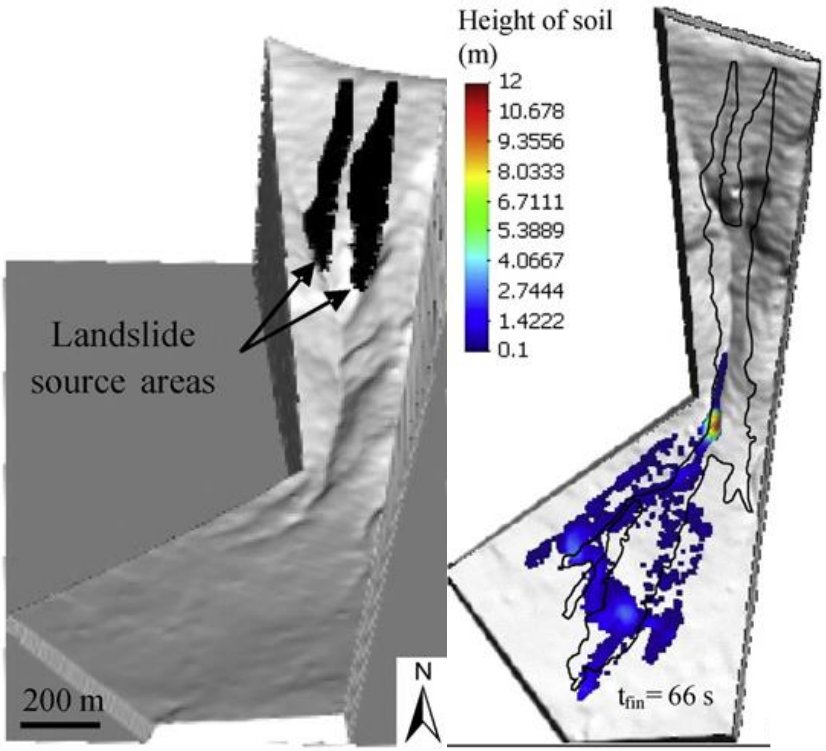

Figure 8.12 The landslide source areas and the final deposition thicknesses computed for the Tuostolo basin (modified from Cascini et al., 2014).

8.2.1 Model and input data

The numerical analysis was performed through the mathematical model "GeoFlow_SPH, using the frictional-type model with internal pore water pressure to describe the flowing masses (Equation 8.1) and implementing the Froude number (*Fr*) (Equation 8.2) to analyze the kinematic characteristics of the flows that interact with the control works.

$$Fr(x,y,t) = \frac{u(x,y,t)}{gh(x,y,t)^{\frac{1}{2}}} \tag{8.2}$$

The numerical modeling was not a simple task for different reason; firstly because of the different resolutions of DTMs: 3x3 m DTM of the sites just after the 1998 events and 1x1 m DTM of the sites including the control works; secondly, for the morphological changes from 1999 to 2011 (years of DTMs realization); lastly, for the hypotheses about the future events magnitude.

8.2.1.1 DTMs

The modeling was performed using two DTMs, both were obtained referring to the LIDAR survey of the Italian Environmental Ministry. The 3×3 DTM, used from Cascini et al., 2014, was realized in 1999; while high-quality 1×1 DTM was realized in 2011. The DTMs were called in Figures 8.13 and 8.14, "DTM" and "DTM CW", respectively. The latter, includes the control works that were all complete on 2005 (Fig. 8.13).

The longitudinal sections of the DTMs, shown in Figure 8.14, highlight many changes in the ground surface of natural and anthropic origin. Moreover, the DTMs resolutions capture in different way some topographical details, in particular the morphological frame located at about 450 m a.s.l. For all these reasons, some operations were carried out through Quantum GIS to take into account the DTMs differences:

- the resolution change of the "DTM" from 3×3 m to 1×1 m in order to make numerical results independent of the different resolutions;
- the cut and merge of different zones of both DTMs in order to make numerical results independent of the morphological changes that have occurred from 1999 to 2011.

Concerning the latter point, four cuts were operated on both DTMs, dividing each topography into five zones (Fig. 8.14). The four cuts were performed at 233; 157; 140 and 96 m a.s.l., where the longitudinal sections of the DTM and DTM CW overlapped exactly. The Figure 8.15 shows several combinations of the cut zones of both DTMs. In the upstream zone, the DTM CW was considered more suitable than DTM to represent the ground surface, due to the morphological frame. As it concerns the downstream zone, different conditions were considered: without control works (Fig. 8.15a); with the only check dams (Fig. 8.15b); with check dams and storage basins (Fig. 8.15c) and with the only storage basins (Fig. 8.15d). These conditions allowed us to evaluate the performance of each control work when the ordinary maintenance of the other structures is not carried out. Indeed, some site inspections carried out downstream of the Tuostolo basin in September 2017 have revealed low-maintenance and control works completely filled by vegetation (Fig. 8.16).

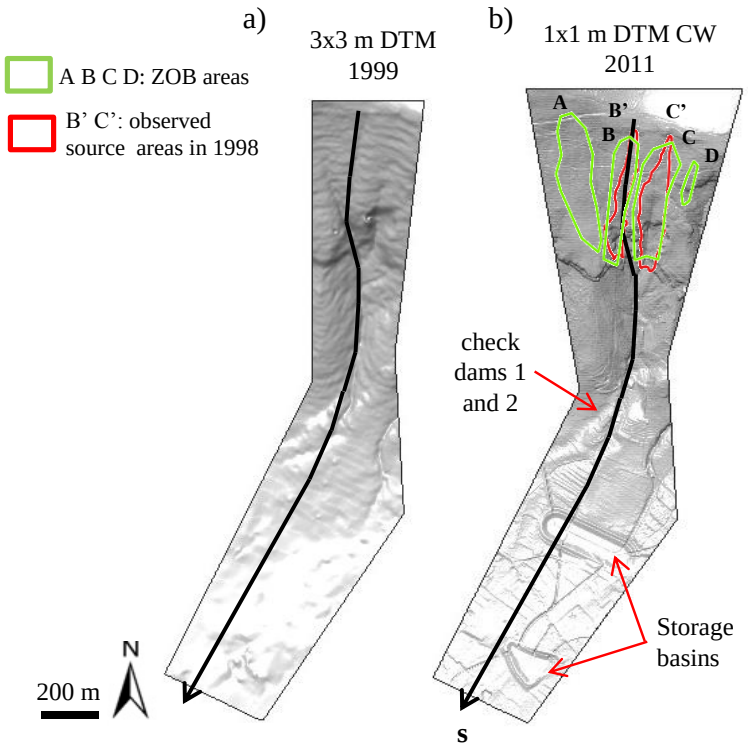

Figure 8.13 DTMs and source areas used for the numerical modelling of the flows.

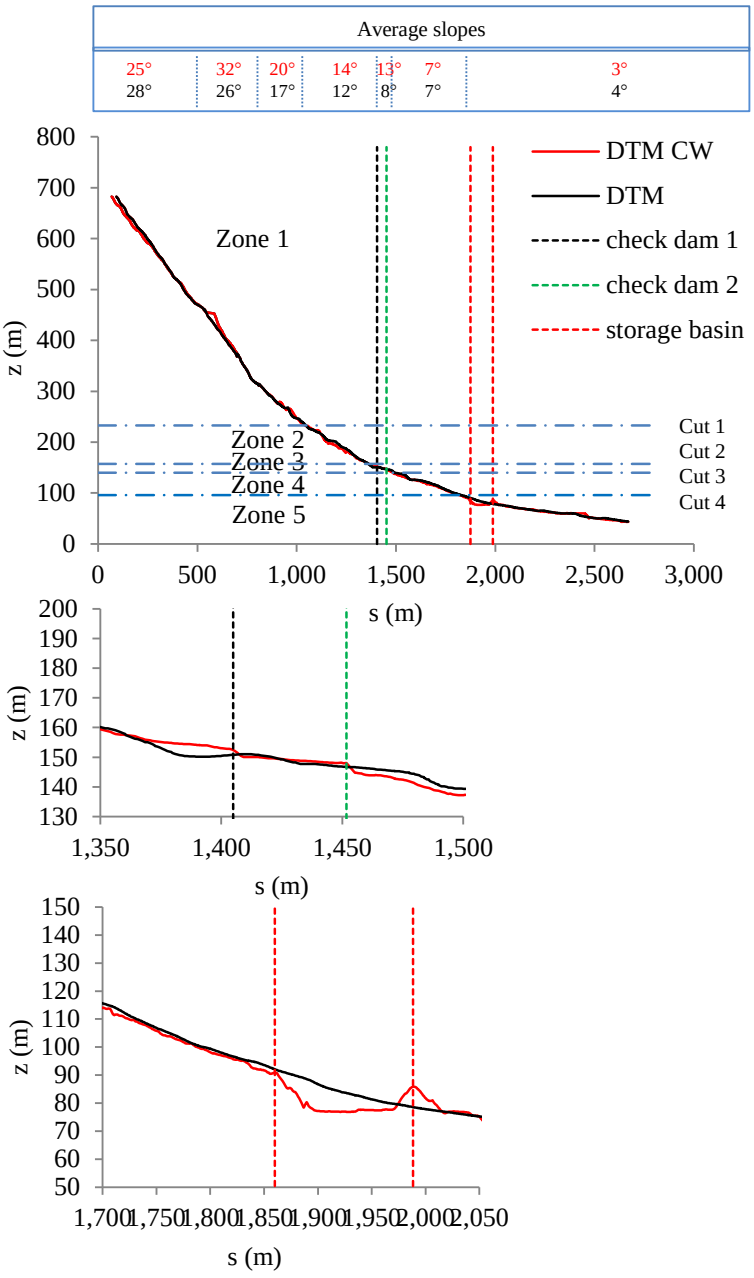

Figure 8.14 Longitudinal sections of the DTMs.

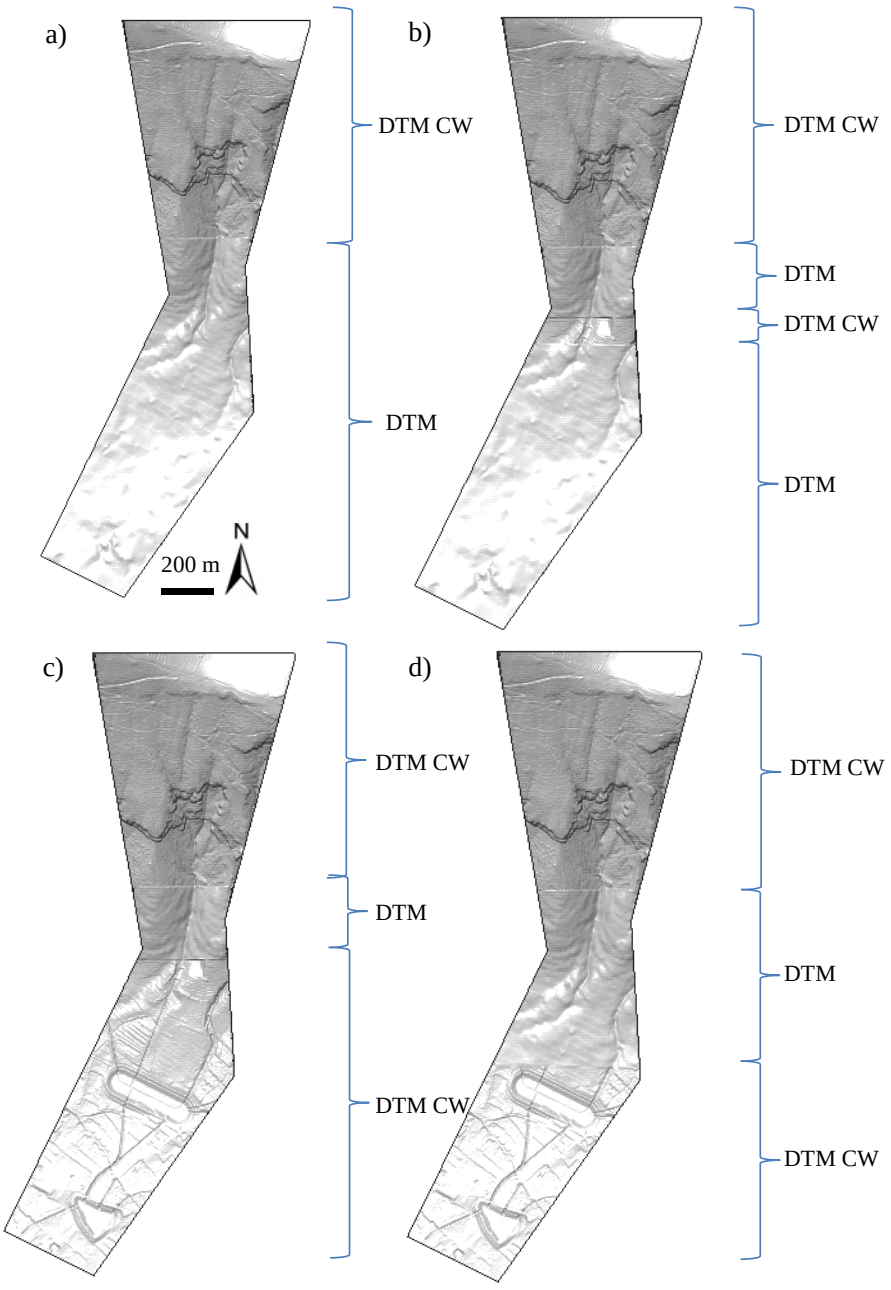
a)
DTM CW
DTM
200 m
N
b)
DTM CW
DTM
DTM CW
DTM
c)
DTM CW
DTM
DTM CW
d)
DTM CW
DTM
DTM CW

Figure 8.15 Several combination of two DTMs (DTM and DTM CW) used for the numerical modelling of the flows.

Figure 8.16 Check dams, channel and storage basin filled by vegetation (photo taken in September 2017).

8.2.1.2 Triggering masses

Some hypotheses have been introduced about events magnitude that might potentially occur in Tuostolo basin. The extent of the landslide source areas was obtained from the literature (see Section 8.2 and Fig. 8.11). The initial depths of the propagating masses were obtained from soil thickness maps (Fig. 8.9) and in-situ investigations (Fig. 8.10). In particular, for the ZOB area called "B" in Figure 8.10, the depth below the slip surface observed in 1998 events was used (Fig. 8.10); for the ZOB "C", the depth of the masses involved in 1998 events was

subtracted to the pyroclastic deposits thickness shown in Figure 8.9. Finally, for the ZOB areas A and D, the minimum and maximum deposits thickness shown in Figure 8.9, were used. The Figure 8.17 shows the obtained triggering masses.

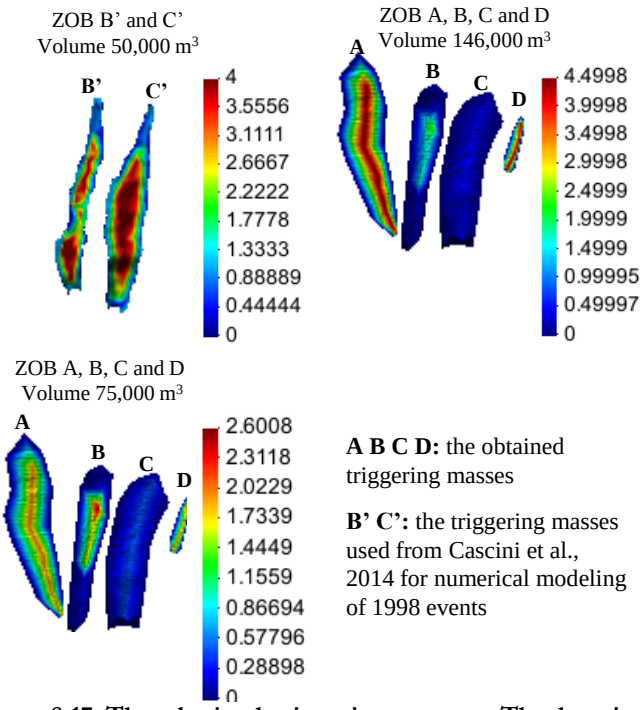

Figure 8.17 The obtained triggering masses. The location of source areas is shown in Figure 8.13.

8.3 RESULTS

8.3.1 Model calibrations

The 1998 event in Tuostolo basin with an initial volume of 50,000 m^3 was modelled referring to the DTMs of Figures 8.13a and 8.15a. The first was modified changing the resolution from 3×3 m to 1×1 m and the second was used because takes into account the "topographic jump" due to the morphological frame.

The Figure 8.18 highlights that using the DTM of Figure 8.13a, a friction angle of 20° is able to back-analyze the event dated 1998; while considering the DTM of Figure 8.15a, the best fitting the field evidence is given by a friction angle of 14°.

The calibrated parameters vary depending on the DTM; in particular, using a 1×1m DTM the calibrated rheological properties indicate a lower friction angle than for a 3×3m DTM. Sosio et al., 2012 in similar cases, interpreted this variation as a result of the higher roughness of the terrain when it is resampled to a smaller cell size. The decrease in the resistance offered by the material by means of its rheological properties serves to balance the increased resistance offered by the terrain (Sosio et al., 2012). This result is also evident in Figure 8.18c, where the "topographic jump" due to morphological frame, produces a decrease of friction angle from 20° to 14°.

In order to understand the flows kinematic behavior during the 1998 event, the Froude number along the section "s" shown in Figure 8.13, was computed for the modeling of Figure 8.18c at significant time lapses from the triggering. Particularly, 5 specific time lapses were selected corresponding to the arrival of the front part of the flows to the sections 1-5; "1" and "2" located at the channel exit and "3", "4" and "5" at the piedmont zone (Fig. 8.19a). The evolution of Froude number along the section "s" shows a fluctuating trend ranging from 0 to about 10. These oscillations depend on the evolution of the flow velocities and propagation heights on a the detailed DTM. However, it is possible to distinguish along the propagating mass three regions of Froude: high

values of Froude number at the front and the tail, low values along the landslide body. Passing from section "1" to section "5" the front Froude is constant (about equal to 10); while the tail and body Froude decrease until values lower than 1.

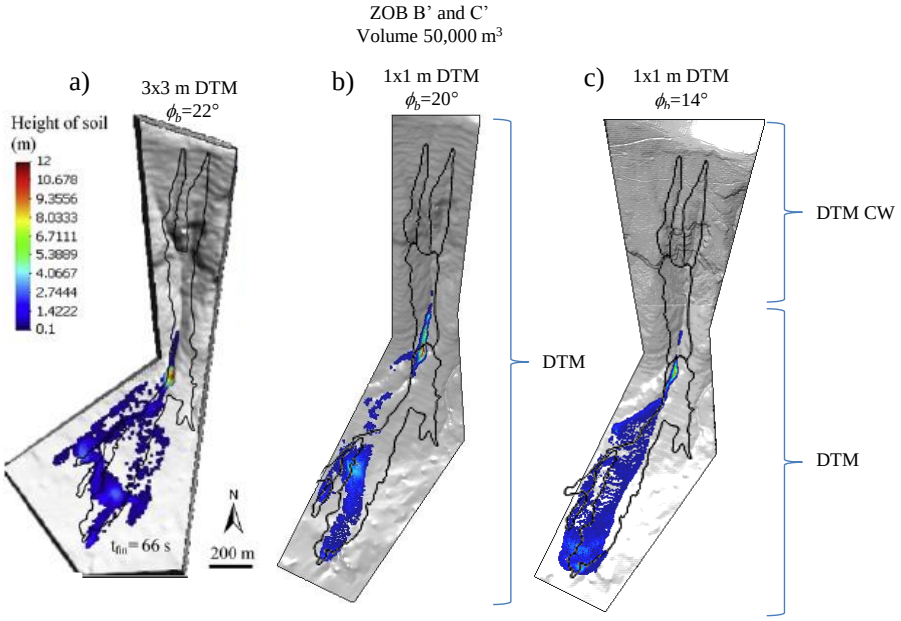

Figure 8.18 a) Deposition thickness simulated by Cascini et al., 2014 for the 1998 event; b)simulated deposition thickness using the 1×1 DTM of Figure 8.13a and c) the 1×1 DTM of Figure 8.15a. The black line represents the boundary of deposit observed in the field.

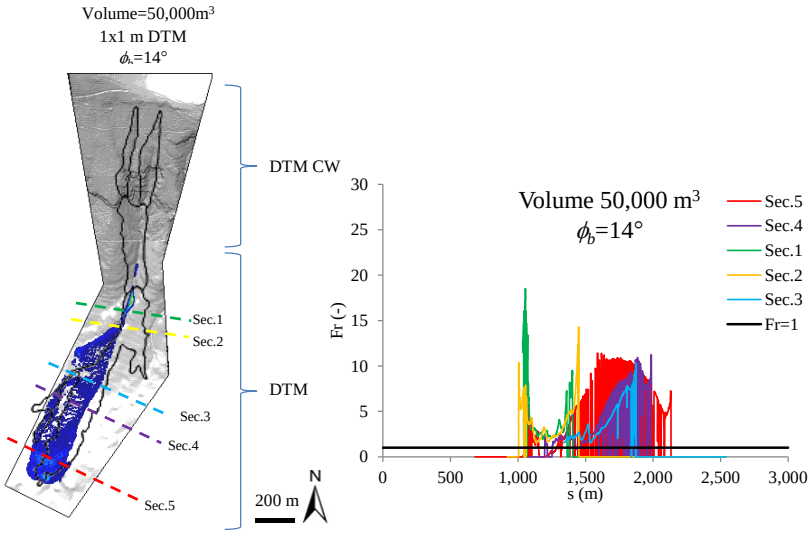

Figure 8.19 Froude number along section "s" computed at the time lapses when the flows reached the cross-sections 1-5.

8.3.2 Modeling of the possible future events

Once calibrated, the same model was used to interpret possible future events. Several numerical analysis were performed to simulate: the propagation of 75,000 m^3 and 145,000 m^3 events. The triggering masses used for modeling are shown in Figure 8.17, while the DTMs in Figures 8.15b, c, d and 8.13b.

The list of the most significant numerical cases is reported in Table 8.1, while the results are shown in Figures 8.20 and 8.21. The numerical results of the cases 1, 2, 3 and 4 reproduce the propagation of partially saturated volume of 75,000 m^3 and the interaction with the only check dams (Case 1); storage basins (Case 3) and both check dams and storage basins (Case 2 and 4). The simulated flows overpass the passive control works in cases 1, 2 and 3; while the flow is intercepted in Case 4 (Fig. 8.20). In particular for the Case 4, the deposition thicknesses near to the check dams and in the storage basins reaching height of about 5,00 m.

The plots of Figure 8.22 clearly show that the flows have always Froude numbers higher than one. However, the Froude number trend along "s" changes in shape due to interaction of flows with the check dams or

storage basins. In particular, the Fr at the front of the flow is equal to 10 when the flow interacts with the check dams, while it is about 20 when there are not the works (see Section 2 of cases 1 and 2 of Fig. 8.22); in the same way the Fr is equal to 5 or 3 when the flow interacts with the storage basin, while it is equal to 12 without basin (see Section 4 of cases 1, 2 and 4).

The Figure 8.21 shows the propagation of saturated volumes of 75,000 m3 and 145,000 m3. The 75,000 m3 propagating mass overpass the first storage basin reaching deposition height of about 5 m near to the check dams; while the 145,000 m3 propagating mass overpass both basins.

Table 8.1 List of numerical cases analysed for future events.

Case	DTM of Fig.	Volume (m^3)	ϕ_b (°)	h_w^{rel} (-)	p_w^{rel} (-)	c_v ($m^2\ s^{-1}$)
1	8.15b	75,000		0.4		
2	8.15c	75,000		0.4		
3	8.15d	75,000		0.4		
4	8.13b	75,000	14	0.4	1	1.0×10^{-2}
4b	8.13b	75,000		1		
5	8.13b	145,000		0.4		
5b	8.13b	145,000		1		

ϱ: mixture density equal to 13.0 kN m^{-3}, ϕ_b: basal friction angle, h_w^{rel}: relative water height, p_w^{rel}: ratio of pore water pressure to liquefaction pressure; c_v: consolidation coefficient.

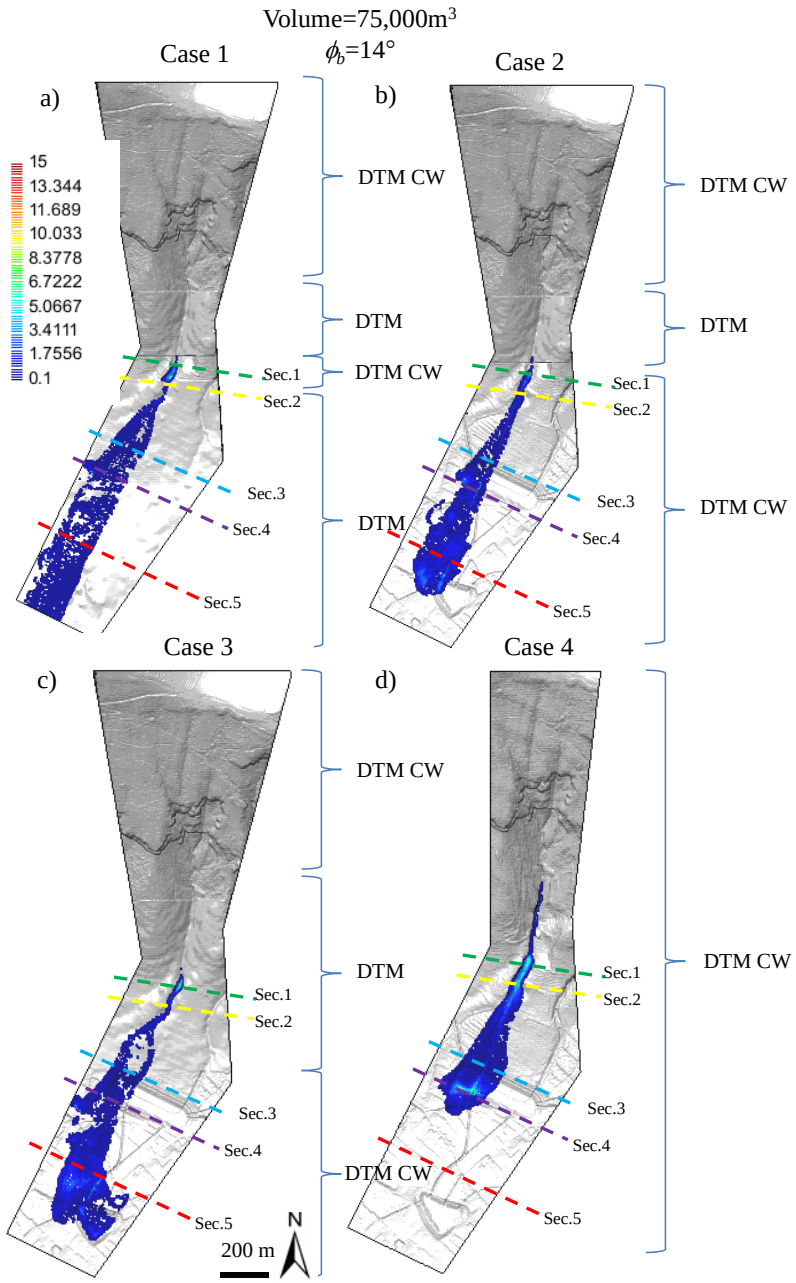

Figure 8.20 Final deposition thicknesses computed for the 75'000 m³ event: scenarios 1, 2, 3 and 4 of Table 8.1.

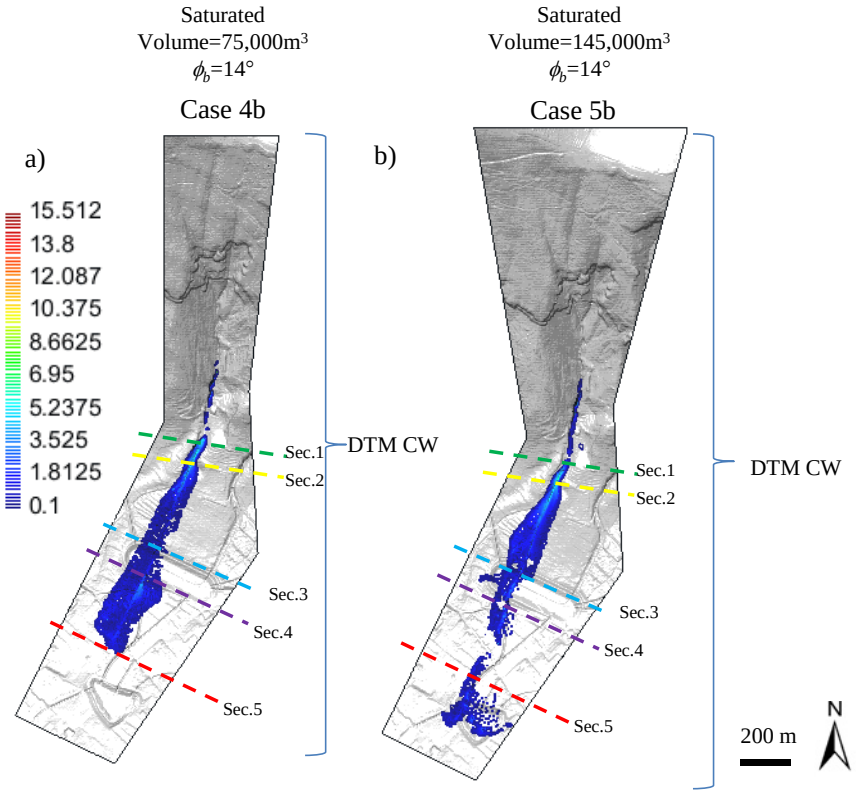

Figure 8.21 Final deposition thicknesses computed for the 145'000 m³ event: secenarios 4b and 5b of Table 8.1.

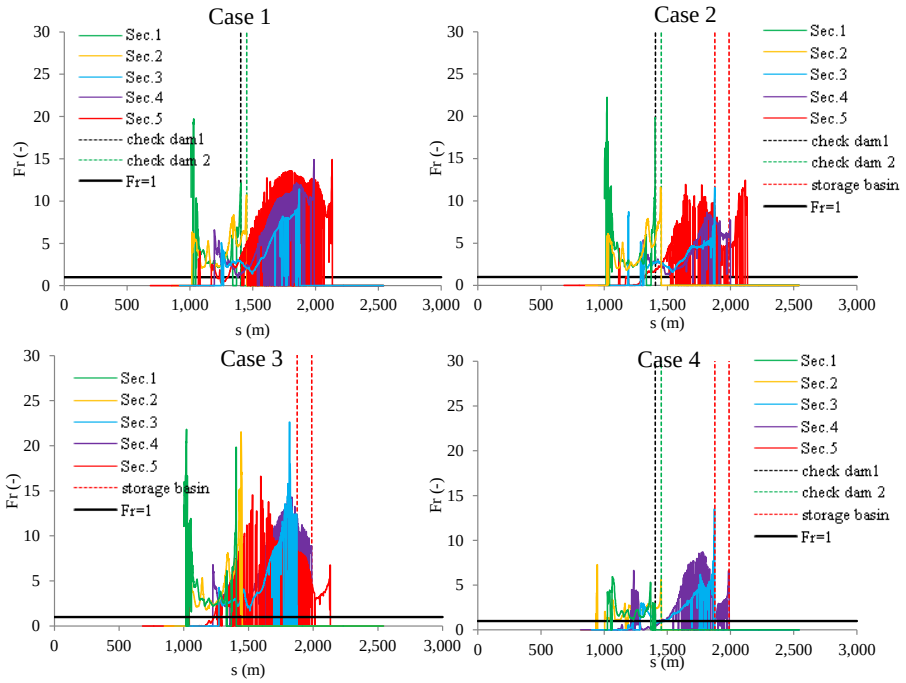

Figure 8.22 Froude number along section "s" computed at the time lapses when the flows of Figure 8.20 reached the cross-sections 1-5.

8.4 DISCUSSION

Several flow like mass movements have been considered to analyze the effectiveness of the control works in the "Tuostolo" mountain basin. The numerical results highlighted many aspects concerning the propagation analysis of flow-like mass movements and the evaluation of control works effectiveness.

As it concerns the propagation analyses, the quality of the DTM and the rheological behavior of flows represent critical issues that affect the reliability of numerical results. The analysis about effectiveness of control works highlighted the importance of planning a periodic and preventative maintenance.

In detail, the influence of terrain representation on the numerical results was already discussed in Pastor et al., 2014 and Sosio et al., 2012. The authors highlighted the topographical details are captured in a different way by DTMs with different resolutions. Moreover the calibrated parameters vary with the adopted topographic data resulting in lower values of the rheological parameters (friction angles) for smaller cell sizes. In agreement with the previous evidences, in analyzed cases the 1×1m DTM was considered more suitable than 3×3m DTM to represent the morphological frame; the calibrated friction angle using a 1×1m DTM was equal to 14° compared to 20°, considering a DTM with bigger cell sizes.
However, the rheological parameters were calibrated and validated through a back-analysis of past events in order to make numerical results independent of input data quality. In particular, the frictional-type model with internal pore water pressure was used for the calibration and potential events modeling. For latter, different percentages of water-solid in the mixture was considered, referring to the classification system of Coussot and Menieur (1996) (Chapter 2).

In the quoted reference of the passive control works, an important limitation was mainly related to the modeling of drainage systems since there were not adequate and detailed project data to be transformed into appropriate boundary conditions. Such limitations determine an underestimation of the works effectiveness, which has been analyzed through Froude number. In particular, it can be observed that the Froude number changes in shape and decreases when the flows intercept each component of protection system; however, the effectiveness of passive control works is guaranteed only if all the components are operational.

The control works functionality depends on emergency or ordinary maintenance; more specifically, as it concerns the case study it was observed that: i) the maintenance have to be performed at least every 20 years; ii) periodic and ordinary maintenance have to be concern especially drainages, channels and check dams; iii) lack of maintenance makes the control works totally useles

9 UPGRADING OF EXISTING CONTROL WORKS

"Debris-flow dewatering brakes" or "permeable rack" is an "old-new" control work carried out at downstream of the mountain basins to reduce the pore water pressures up to the mass eventually stops. It is an "old" control work, because the basic idea of rack was proposed by Hashimoto and other Japanese scholars in the fifties (Cascini et al., 2016a,b). It is "new" since it is rarely built because the local residents are skeptical about its efficacy (Fig. 9.1). Anyway, it can be an alternative or a completion to passive control works, as suggested by Mizuyama 2008 and Suwa et al., 2009 who proposed the use of the debris-flow breaker at upstream of a check dam to control sediment discharge.

The potentiality of a permeable rack is essentially related to three phenomena that occur when the debris flow crosses the permeable rack i) drainage of the pore water pressures through the "screen" of the debris flow breaker; ii) increase of the sediment concentration and the basal shear stress of the debris flow; iii) rest of the propagating mass behind the debris flow breaker. Indeed, the flowing mass rapidly passes from a supercritical to a subcritical flow.

The permeable racks were tested in three pilot projects in Japan to collect data and technical know-how regarding their construction and maintenance; then, a full-scale project was implemented at Mt. Tokachidake in Hokkaido, Japan (ICHARM, 2008). However, many authors are testing experimentally the efficacy and the efficiency; while the physically-based mathematical modelling of the interaction of debris flows with this type of structures has not yet been developed

This Chapter contributes to clarify the potential of a (permeable) rack, located along the propagation path, using the numerical model proposed by Pastor et al. (2015a,b) and the Froude number as an useful tool to estimate its performance. The SPH-FDM model combines a 3D depth-integrated hydro-mechanical coupled SPH (Smooth Particles Hydrodynamics) model for the propagation analysis and a 1D vertical FDM (Finite Difference Method) model for the evaluation of the pore water pressures along the height of the flowing mass (see Chapter 6). This model is used to simulate the flume tests, performed in Japan in a 3.4m long channel, equipped without or with a (permeable) rack at the end of the channel.
Once tested the reliability of the SPH-FDM model to describe the behavior of a debris flow on a permeable bottom boundary, the same model is used to simulate the presence of a permeable rack in a real mountain basin, located in Sarno town (described in previous Chapter). In particular, by way of example, the adaptation of the existing system of passive control works with permeable rack was proposed. The results show that the SPH-FDM model is capable to properly reproduce the propagation stage of flow-like mass movements with different hydraulic boundary conditions, such as an impervious or permeable bottom. Furthermore, the results highlight the effectiveness of the permeable rack and the potential use as adaptation structure in weak current protection systems.

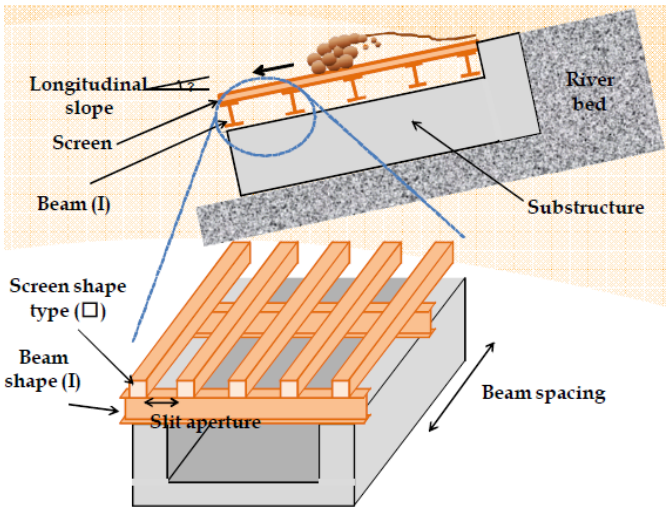

Figure 9.1 Structure of a debris-flow dewatering brake.

9.1 MODELING OF A CONTROL WORK BASED ON A PERMEABLE RACK IN FLUME TESTS

9.1.1 Flume tests of Gonda (2009)

Gonda (2009) performed flume tests in a channel, 16° to 19.7° steep, 2.40 m long, 0.20 m wide, equipped with a (permeable) rack – 0.20 m wide, and 1.0 m long – installed horizontally at the downstream end of the channel (Fig. 9.2) (Cascini et al., 2016a,b).

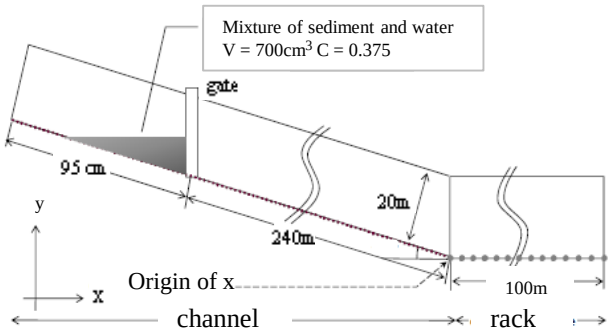

Side view of experimental channel

Figure 9.2 Experimental channel: longitudinal profile of the channel (wide 20 cm) and geometry of the initial mass. At the downstream end of the channel there is a (permeable) rack (Gonda, 2009).

A volume of soil equal to 7000 cm^3 was released through the opening of a vertical gate and the propagation of a debris flow was generated. A digital video camera was installed above the rack to measure the run-out distance over this draining boundary (Cascini et al., 2016a,b).

The sediment mixture used for propagation tests was composed of a nearly uniform gravel and water, with a volumetric concentration of the sediment particles equal to 0.375. Three types of materials (A, B and C) were used, different for median diameter size (d: 1.8, 3.4 and 4.7 mm, respectively), density (ϱ: 22.50, 25.00 and 24.00 kN m−3, respectively) and friction angle (φs: 40.1, 41.1 and 38.8, respectively). The experiments were performed varying both the inclination of the channel, 16° or 19.7°, and the material (A, B or C). The sizes of the openings of the rack were varied in a range of values from zero to 12mm, i.e. 0, 1, 2, 4, 8, and 12 mm. It is worth noting that the coarser racks (with the openings 8 or 12m large) allow the sediments to pass through, independent on the material used (A, B or C). Conversely, the finest racks with the openings 1 or 2 mm large allow the dissipation of pore water pressures, while do not permit the sediments passing through; in particular, for the finest 1.8mm"A" material, the rack is in the limit to permit the passing through. The intermediate rack (4mm) was permeable to finer solid sediments (A and B material),while permeable only to the water for the coarsest material "C" (Cascini et al., 2016a,b).

Figure 9.3 shows the variation of debris flow run-out with the size of the openings of the rack, while material A was adopted. A rack with 1mm large openings causes a reduction in the run-out distance about 45 cm; for a rack with 2 to 4 mm large openings, the run-out reaches a limit value almost equal to 25 cm for which the opening of the rack appears irrelevant; the last test with 8mm openings resulted in a slightly smaller runout (about 20 cm), probably due to a loss of mass volume through the rack (Gonda, 2009).

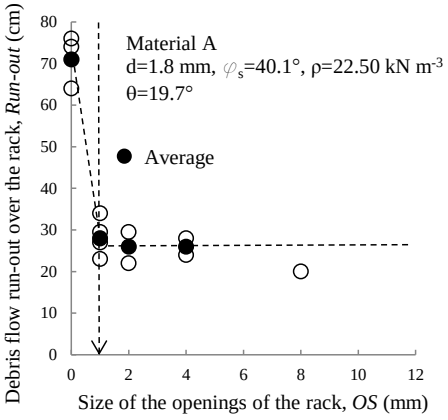

Figure 9.3 The variation of the debris flow run-out measured by Gonda (2009), using the material "A" and different sizes of the openings of the rack (from Cascini et al., 2016a,b).

Gonda (2009) performed a complete series of experimental flume tests varying all the variables above mentioned. A selection of these tests will be referred because the passage of the sediments through the openings of the rack cannot be simulated via the SPH-FDM model presented in this paper. Thus, the focus is on the Cases with openings of the rack smaller than the median diameter of sediments, as listed in Table 9.1. Among these, the tests with the water drainage allowed by a permeable rack will be included in the numerical analyses and the reduction of the run-out distance due to the presence of this control work will be one of the main issues considered in the numerical modelling. A role is also played by soil unit weight (Case 3 compared to Case 8). And similar run-out distances were measured from the different combination of material and bed slope (for instance Cases 6–9 compared to Cases 17–20) (Cascini et al., 2016a,b).

Table 9.1 Flume tests of Gonda (2009) selected for the numerical modelling.

Case	Material	Slope (°)	d (mm)	OS (mm)	Run-out* (cm)
1	A	19.7	1.8	0	70
2				1	28
3				2	26
6	B	19.7	3.4	0	57
7				1	28
8				2	17
9				4	19
11	C	19.7	4.7	0	58
12				1	38
13				2	29
14				4	21
17		16.0	4.7	0	49

18		1	38
19		2	23
20		4	17
OS: Opening size; *: distance on the rack			

9.1.2 Numerical analyses

The numerical analysis was easy due to the simple geometry of the flume used by Gonda (2009), i.e. a straight channel (B/L = 0.0833), where the mass propagates inside, confined from initiation to deposition. Thus, only a 2D analysis was carried out. In the experimental device, the initial mass was retained by a vertical gate abruptly opened to start the test and the initial configuration of the mass corresponding to a horizontal ground surface. Unfortunately, Gonda (2009) does not provide any image about the mass configuration just after the gate opening. Thus, the presence of the gate was not included in the numerical model and the mass was instantaneously released without any confinement or external constraint (Cascini et al., 2016a,b).

The rack was simulated by a special boundary condition assigning a zero pore pressure at the ground surface where the SPH nodes are propagating over. One of the advantages of incorporating a set of finite difference meshes at each SPH node is the ability to simulate cases where basal pore pressures go to zero as a consequence of the landslide crossing a terrain with very high permeability or a particular control work (Pastor et al., 2015a). It is important noting that for all of the cases including a permeable rack, the loss of water – escaping through the rack during the flow propagation over – was not included into the model. This is thought as a secondary process, because the time for the flow to decelerate and stop is in the order of few seconds, while a significant amount of water should require at least some tens of minutes to seep out of the mass (Cascini et al., 2016a,b). The numerical modelling was carried out assuming a frictional rheological model (Eq. 9.1), with the rheological parameter reported in Table 9.2.

$$\tau_b = -\left((1-n)(\rho_s - \rho_w) g\, h - p_w^b\right) tg\phi_b\, sgn(\bar{u}) \tag{9.2}$$

Table 9.2 Rheological parameters for the numerical simulations of the flume tests performed by Gonda (2009).

Material	ϱ (kN m^{-3})	tan ϕ_b (-)	c_v (m^{2}s^{-1})
A	22.50	0.84	3.0×10^{-3}
B	25.00	0.87	3.0×10^{-3}
C	24.00	0.80	3.5×10^{-3}

ϱ: mixture density, ϕ_b: basal friction angle, h_w^{rel}: relative water height equal to 1.0, p_w^{rel}: ratio of pore water pressure to liquefaction pressure equal to 1.0; c_v: consolidation coefficient.

In Figure 9.4 lower graphs we have plotted the vertical profiles of pore water pressure computed 3.35 m downslope the slope break, without or with the drainage rack. The Case 11 has lower pressures than Case 1 and Case 6, because the material C has a higher consolidation coefficient (c_v). The Case 17 has lower pressures than Case 11 (same material) because related to a channel inclination equal to 16°, consequently, the debris flow has a higher velocity component in the direction of the flow compared to that perpendicular to the bottom (Cascini et al., 2016a,b). The run-out distances measured for the tests of Table 9.1 are compared to the numerical simulations in Figure 9.5.

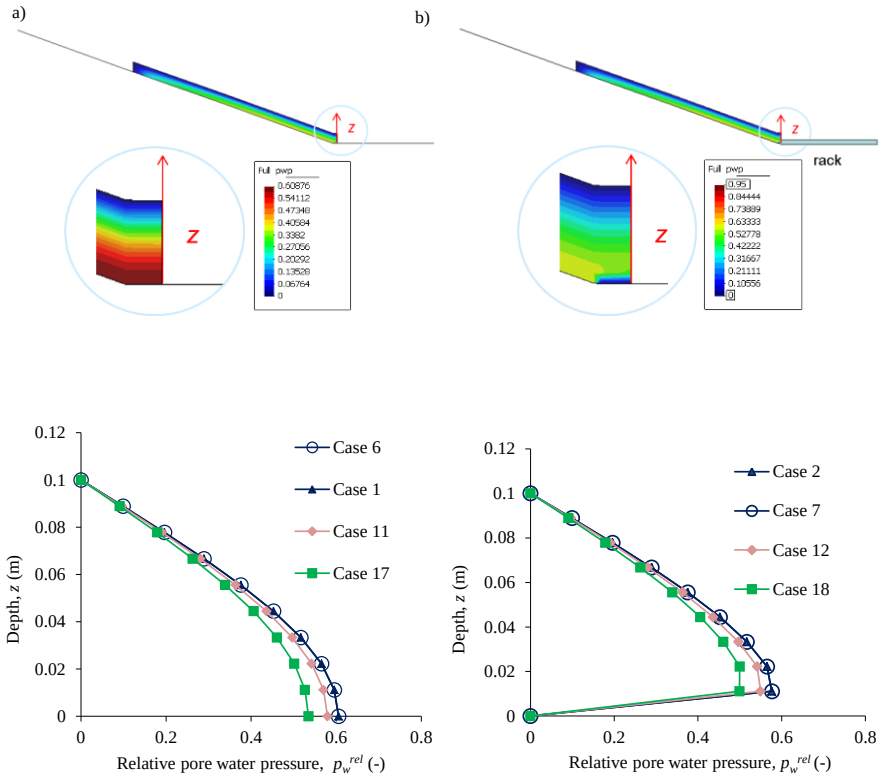

Figure 9.4 Vertical profiles of the computed relative pore water pressure (p_w^{rel}) without (a) and with (b) a draining boundary condition (i.e. p_w^{rel} assigned equal to zero) in the horizontal terminal part of the channel where the rack is located (from Cascini et al., 2016a,b).

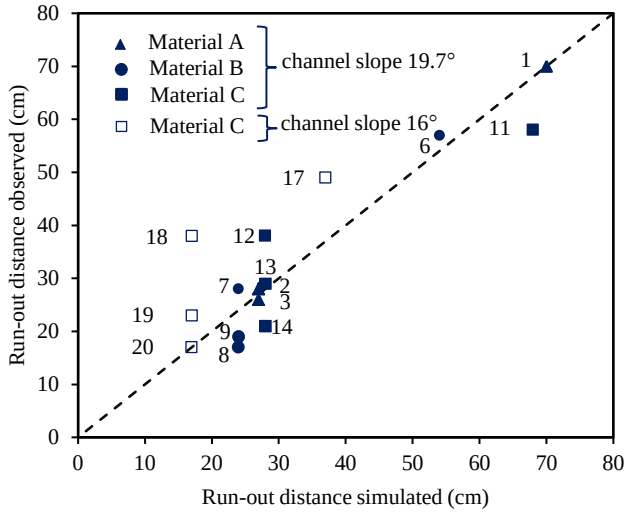

Figure 9.5 Comparison of the experimental measurements and the numerical simulations of the run-out distances on the rack for the tests of Table 9.1. The legend refers to the different material and channel slope and the numbers represent the experimental conditions of the Table 9.1 (from Cascini et al., 2016a,b).

The numerical results obtained for the flume tests with a rack impervious to both water and sediments (i.e. an impervious boundary condition) are quite satisfactory as they approximate the line 1:1 in the plot of Figure 9.5. Indeed, the plots are moderately dispersed around that line, and this dispersion – pretty acceptable – can be regarded as a measure of the uncertainties and approximations of the numerical analyses. It is also worth noting that in any reduced-size physical model, such as the flume tests of Gonda (2009), only 2.4 m long, the smaller is the prototype, the higher can be the differences between experimental and numerical results. This is because a reduced size model is much more influenced by any perturbation or measurement approximation than bigger prototypes are (Cascini et al., 2016a,b).

It is firstly important outlining that the numerical model simulates the propagation and run-out distance, for the cases without any drainage. On the other hand, the effect of the rack is properly simulated. in terms of the material A and B, the best simulations of the propagation and pore water pressure dissipation are obtained for the finest rack (opening size equal to 1 mm, see Cases 2 and 7). n the case of material C while the channel inclination equal to 19.7°, the best simulation test including a rack is that with 2 mm openings, see Case 13, while for the channel inclination equal to 16°, the best simulation test is the Case 20.

Later, the performance of the rack is investigated through the analysis of the kinematical features of the flows, computing the Froude number, described in previous chapters, for the Cases 1 and 2 of Table 9.1 at significant times. Particularly, seven specific times were selected starting from 0.79 s that corresponds to the arrival of the front part of the flow to the horizontal terminal part of the channel equipped without (Case 1) and with permeable rack (Case 2). Subsequently, the frequency of all the SPH computational points (n_{tot}=1000) into 6 classes of Froude number was computed and plotted for both Cases.

The Figure 9.6 clearly show that in Case 1, the Froude distribution curve shifted to left in time due to the velocity decrease on the horizontal terminal part of the channel. In Case 2 all computational points arranged into class of Froude 0-1, already starting from 0.79 s. This latter effect was due to the efficacy of the permeable rack, which tends to slow down and then stop the propagating mass.

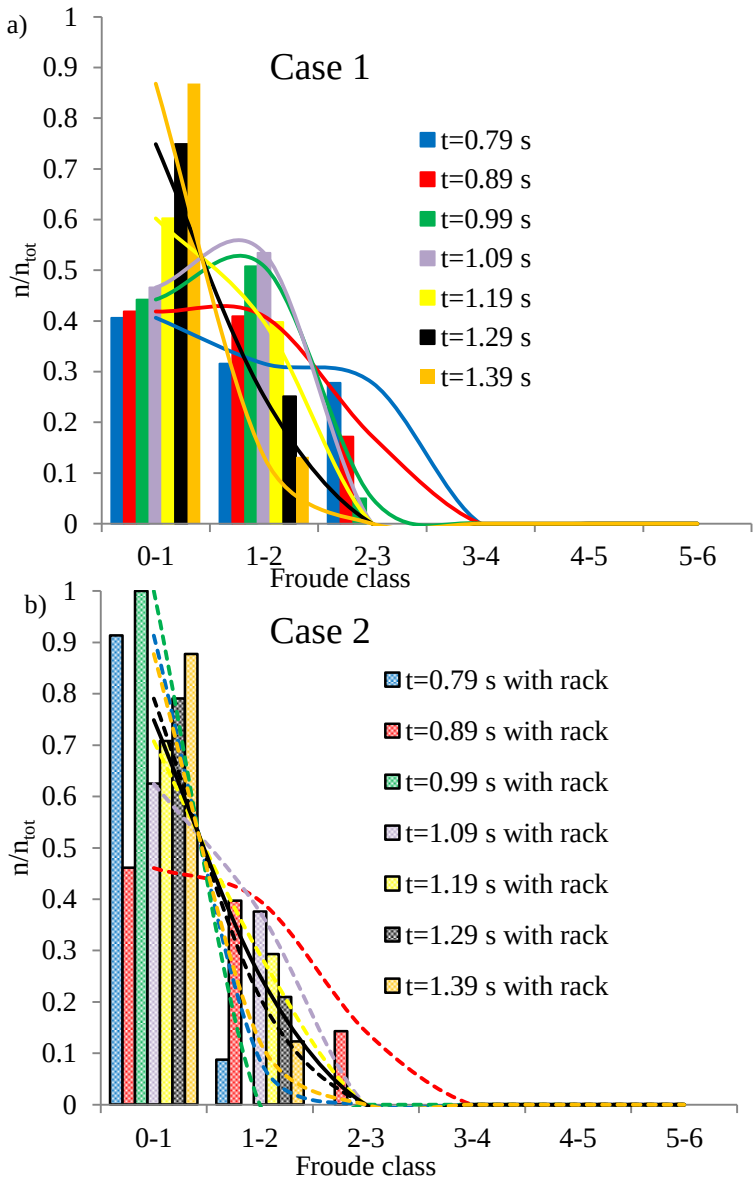

Figure 9.6 Frequency distribution of the Froude number computed within the SPH computational points (n_{tot} = 1000) used for numerical modeling of Case 1 (a) and Case 2 (b), at the significant times.

The results of this modeling are certainly not exhaustive for a difficult topic such as the interaction of debris flows with specific control works aimed to reduce the basal pore water pressures. Nevertheless, it is outlined that the SPH-FDM is actually capable to well describe the behavior of a debris flow propagating over a permeable bottom boundary.

9.2 MODELING OF A PERMEABLE RACK IN "TUOSTOLO" MOUNTAIN BASIN

Once tested the reliability of the SPH-FDM model to describe the behavior of a debris flow on a permeable bottom boundary, the same model was used to simulate the presence of a permeable rack at the toe of Tuostolo mountain basin, widely described in previous Chapter.

In this mountain basin, the numerical modeling was performed considering the rack located in the first storage basin to gather the coarser particles in the first basin and to allow the water to flow toward the second basin. The simulation was carried out using the frictional-type model with internal pore water pressure to describe the flowing mass of 75,000 m^3 (Eq. 9.1), with the following rheological parameter: basal friction angle (ϕ_b) equal to 14°, relative water height (h_w^{rel}, i.e. ratio of the height of the water table to the soil thickness) equal to 1; ratio of pore water pressure to liquefaction pressure (p_w^{rel}) equal to 1.0 and consolidation coefficient (c_v) equal to $1.0 \times 10{-}2$ m^2 s^{-1}. The rheological parameters are calibrated based on past events of '98 and using a 1×1 m DTM that includes the passive control works (see Chapter 8).

The Figure 9.7 provides a comparison of final deposition thickness when no rack is employed and when the rack is located in the first storage basin. In latter case, the run-out distance is lower and the flow is distributed along the total area of the basin reaching deposition height of about 6 m.

In order to understand the flows kinematic behavior when they cross the permeable rack, the Froude number along with the section "s" shown in Figure 9.7, was computed for the performed numerical modeling at

significant time lapses from the triggering. Particularly, 5 specific time lapses were selected corresponding to the arrival of the front part of the flows to the sections 1-5 of Figure 9.7 (as described in Chapter 8). When the flow reaches the permeable rack (Section 4 in Fig. 9.8b) the Froude number decreases at the front of the flow, while it increases along the landslide body (Fig.9.8). The low values of Froude number obtained for the front part of the flow are due to a velocity reduction of the flow and at the same time a height rising of the flow due to the "braking effect" of the rack.

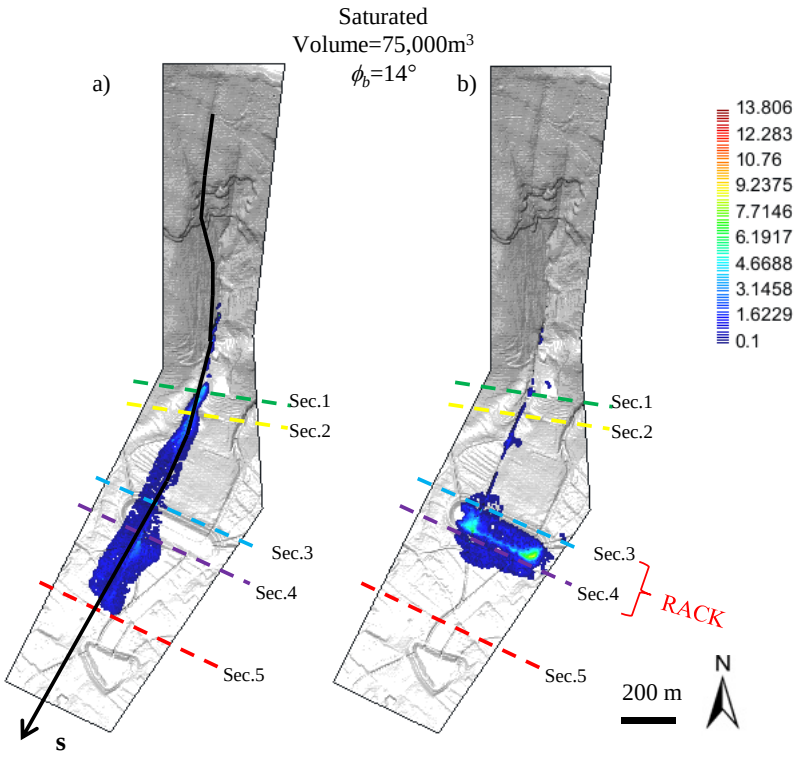

Figure 9.7 Final deposition thicknesses computed for a saturated volume of 75'000 m³ without rack (a) and with rack in the first storage basin (b).

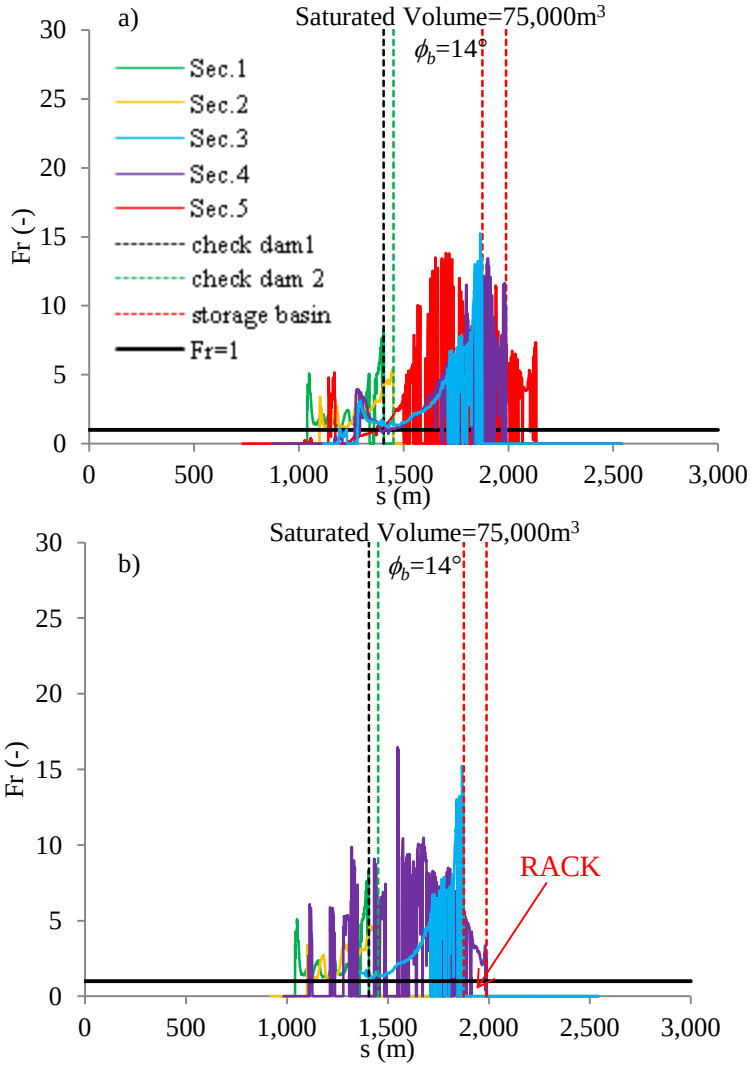

Figure 9.8 Froude number along section "s" a) without rack and b) with rack computed at the time lapses when the flows reached the cross-sections 1-5.

9.3 DISCUSSION

A 3D SPH-FDM model, which combines two sub-models: a formerly published 3D depth-integrated hydro-mechanical coupled SPH (Smooth

Particles Hydrodynamics) propagation model, and a recent 1D vertical FDM (Finite Difference Method) model were used to simulate: i) a 3.4 m long channel Japanese flume, equipped with a permeable basal rack located at the end of the channel. This allows the reduction of the basal pore water pressures, eventually stopping the mass and ii) the presence of a rack as a adaption structure in an existing protection system located in Sarno town.

The performance of the permeable rack was then analyzed through the Froude number computation as described in previous Chapters. the numerical results confirm the efficiency of this new control work. However, many open issues still exist about the efficacy of the permeable rack for different type of flows, different particles size in the propagating masses and different flows velocities.

10 REMARKS AND CONCLUSIONS

Classification of flow-like mass movements depends on several factors: concentration and size of the solid phase (Egashira et al., 1997), particle segregation, pore fluid pressure and mixture agitation (Montserrat et al., 2012). As a consequence, a number of distinct phenomena can be recognized: flash floods, hyperconcentrated flows, mudflows, debris flows, etc., (Coussot and Meunier, 1995; Costa, 1988; Cruden and Varnes, 1996 and Hungr et al. 2009).

The propagation stage of these phenomena can be evaluated through numerical models which implement different rheologies in function of: *i)* the concentration of solid fraction and water content, that change within the wave and along the flow path and *ii)* the regime of the flow, i.e. laminar or turbulent flows, which changes during the propagation phase. In particular, in laminar flows, the water and solid phase move at the same velocity as a single mixture (one-phase flow) while in turbulent flow the grains collisions dominate the flow behavior (two-phase flow).

Considering the consequence to life and properties caused by flow-like mass movements and the lack of criteria to design the risk mitigation measures, this work focuses on the so-called Froude number (*Fr)* that is a dimensionless number widely used in Hydraulic engineering and used in this PhD thesis to identify the flows kinematic regime and to evaluate the effectiveness of mitigation measures.

The Froude number discriminates two different kinematical features of the flow: subcritical or slow and supercritical or rapid. The first is influenced by down slope boundary conditions, while the second, behaving like a "blind" flow, is not influenced by down slope boundary conditions such as the presence of obstacles, other flows and some types of control works. This thesis dealt with flows regime of Newtonian and

non-Newtonian fluids considering simplified geometries, flume tests and case studies.

The kinematic of a 1 D dam break of Newtonian (water) and viscoplastic fluids (hyperconcentared flows or flash flood) was analyzed through the use of a single phase equivalent model developed by Rendina et al., 2017 (FV model). The viscoplastic flows are supercritical even in areas far from trigger zones and their Froude numbers reach maximum values of about 30. Moreover, the numerical analyses highlighted that the higher is the channel slope in which the mass flows, the higher is the Froude number; the higher is the initial height of the flow, the higher is the Froude number.

The *Fr* sharply increases with the increase of the dynamic viscosity then decreases for greater values and the Froude number of water flows is always greater than the corresponding given by a viscoplastic flow.

The same one-dimensional numerical analysis were repeated through the SPH-FDM model proposed by Pastor et al. 2015. The SPH-FDM model treating the propagating mass with pore water pressure as an added variable, is more suitable to simulate frictional flows such as granular flows or debris flows. The Frictional flow analysis highlighted some aspects already found in viscoplastic flow analysis. However, the Froude numbers of Frictional flows are lower than viscoplastic flows and reach maximum values of about 10.
Another important aspect was revealed by the Frictional flows analysis: the critical channel slope i.e. the slope that determines the transition from supercritical to subcritical flow, depends on the mechanical characteristics of the soil (friction angle), while it does not depend on the initial height of the mass.
Once analyzed the kinematic of flows different types on a simplified geometry the same approach was used to interpret a peculiar case history from the Italian Dolomite Alps where, despite the presence of two storage basins, a combination of a large debris flow and a small flash flood was finally able to produce damage and victims down slope the control works. The different performance of control works against debris flow and flash flood was investigated through the SPH model, introducing the Froude number.
The numerical results confirm the efficiency of control works against debris flows and their unsuitableness for the subsequent flash flood;

since debris flows and flash floods propagated like subcritical and supercritical flow, respectively. In particular, the distribution of Froude number (i.e. distribution of the Froude number classes for the SPH computational points) within the debris flow changes when the flow interacts with the control works and most of the SPH points reaches values of *Fr* lower than one; while the distribution of Froude number within the flash flood did not have any significant change.
The second case study regards "Tuostolo" mountain basin in the Campania region, where after the catastrophic events of '98, many control works such as channels, check dams and storage basins were built. Considering that no event occurred after the control works construction, the magnitude of future events was estimated on the basis of the available data. The performance of the protection system was analyzed through the SPH model and referring to Froude number again.
The numerical results highlighted many aspects concerning the propagation analysis of flow-like mass movements and the evaluation of control works effectiveness.
As it concerns the propagation analyses, the quality of the DTM and the rheological behavior of flows represent a critical issue that affects the reliability of numerical results. The analysis about effectiveness of control works highlighted the importance of planning a periodic and preventative maintenance.

By way of example, the adaptation of the existing control works system in Tuostolo basin, with rack located in the storage basin was simulated through the SPH-FDM model. The rack was simulated by a special boundary condition assigning a zero pore pressure at the ground surface where the SPH nodes are propagating over (Cascini et al., 2016). A comparison of final deposition thickness when no rack is employed and when the rack is located in the storage basin was done. In latter case, the flow slows down and then stops in the storage basin. In order to clarify this behavior, the flows kinematic characteristics were analyzed: when the flow reaches the permeable rack the Froude number decreases due to a velocity reduction of the flow and at the same time a height rising of the flow due to the "braking effect" of the rack.

REFERENCES

Al-Mashidani, G. and Taylor C. (1974). Finite element solutions of the shallow water equations-surface runoff. Finite element methods in flow problems, 385-398.

Arattano M., and Savage W. Z. (1994). Modelling debris flows as kinematic waves. Bulletin of Engineering Geology and the Environment, 49(1), 3-13.

Armanini A, Larcher M, Odorizzi M (2011). Dynamic impact of a debris flow against a vertical wall. Italian Journal of Engineering Geology and Environment 11:1041–1049.

Bacchini, M., and Zannoni, A. (2003). Relations between rainfall and triggering of debris-flow: case study of Cancia (Dolomites, Northeastern Italy). Natural Hazards and Earth System Sciences 3: 71–79.

Begueria S., van Asch Th.W.J., Malet J.-P, Grondahl S. (2009). A GIS based numerical model for simulating the kinematics of mud and debris flows over complex terrain. Natural Hazard and Earth System Sciences,9, pp. 1897-1909.

Berti M., Genevois R., Simoni A., Tecca P. R. (1999). Field observations of a debris flow event in the Dolomites. Geomorphology, 29(3), 265-274.

Brunkal, H. A. (2015). Analysis of post-wildfire debris flows: Climate change, the rational equation, and design of a dewatering brake. Colorado School of Mines.

Calvetti F., Di Prisco C.G, Vairaktaris E. (2017). DEM assessment of impact forces of dry granular masses on rigid barriers." Acta Geotechnica 12.1 129-144.

Campbell C. S., Brennen C. E., Sabersky R. H. (1985). Flow Regimes in inclined Open-Channel Flows of Granular Materials. Powder Technology, 41: 77-82.

Cascini, L., Sorbino, G., Cuomo, S. (2003, May). Modelling of flowslides triggering in pyroclastic soils. In Proc. Int. Conference on "Fast Slope Movements—Prediction and Prevention for Risk Mitigation", Napoli, Patron Ed (Vol. 1, pp. 93-100).

Cascini L. (2004). The flowslides of May 1998 in the Campania region, Italy: the scientific emergency management. Rivista Italiana di Geotecnica, 2: pp. 11 – 44.

Cascini L., Cuomo S., Sorbino G. (2005). Flow-like mass movements in pyroclastic soils: remarks on the modelling of triggering mechanisms. Rivista italiana di geotecnica, 4, 11-31.
Cascini, L. (2006). La gestione scientifica dell'emergenza idrogeologica del maggio 1998, G.N.D.C.I. - C.N.R., p. 376 (in Italian).
Cascini, L., Cuomo, S., Guida, D. (2008). Typical source areas of May 1998 flow-like mass movements in the Campania region, Southern Italy. Engineering Geology, 96(3), 107-125.
Cascini, L., (2011). Evento del 18 Luglio 2009 – Borca di Cadore (BL). Consulenza Tecnica di Ufficio su incarico del GUP del Tribunale di Belluno, 139 (in Italian).
Cascini L., Cuomo S., Della Sala M. (2011). Spatial and temporal occurrence of rainfall-induced shallow landslides of flow type: A case of Sarno-Quindici, Italy. Geomorphology, 126(1), 148-158.
Cascini L., Cuomo S., Pastor M. (2012). Geomechanical modelling of debris avalanches inception. Landslides.
Cascini L., Sorbino G., Cuomo S., Ferlisi S. (2013). Seasonal effects of rainfall on the shallow pyroclastic deposits of the Campania region (southern Italy). Landslides DOI 10.1007/s10346-013-0395-3.
Cascini, L., Cuomo, S., Pastor, M., Sorbino, G., Piciullo, L. (2014). SPH run-out modelling of channelized landslides of the flow type. Geomorphology 214, 502–513.
Cascini L., Cuomo S., Pastor M., Rendina I. (2016a). SPH-FDM propagation and pore water pressure modelling for debris flows in flume tests. Engineering Geology 213: 74–83.
Cascini, L., Cuomo, S., Pastor, M., Rendina, I., (2016b). SPH-FDM propagation and pore water pressure modelling for debris flows in flume tests. 3rd – 5th October 2016, Aussois, France. ISBN 978-2-9542517-7-6.
Cascini L., Cuomo S., Pastor M., Rendina I. (2017). Modelling of flow-like mass movements interacting with control works in the Italian Alps. Submitted for publication.
Chen J. and Lee C.F. (2007). Landslide mobility analysis using Madflow. In: The 2007 International Forum on Landslide Disaster Management. Ho & Li (Eds), ISBN 978-962-7619-30-7.
Choi C. E., Ng C. W. W., Au-Yeung,S. C. H., Goodwin G. R. (2015). Froude characteristics of both dense granular and water flows in flume modelling. Landslides, 12:1197-1206.
Christen M., Kowalski J., Bartelt P. (2010). REMMS: Numerical simulation of dense snow avalanchea in three-dimensional terrain. Cold Regions Science.
Cornelius, E. A. and Bernt, L. (2014). Numerical solution of the Saint Venant equation for non-Newtonian fluid. The 55th Conference on Simulation and Modelling (SIMS 55). Aalborg, Denmark.

Corominas J. (1996) – The angle of reach as a mobility index for small and large landslides. Canadian Geotechnical Journal, 33, 260-271.

Costa J.E., Williams G.P. (1984). Debris-flow dynamics (video tape): U.S. Geological Survey. Open-File Report 84-606.

Costa J.E. (1988). Rheologic, geomorphic, and sedimentologic differentiation of water floods, hyperconcentrated flows, and debris flows. In: Baker VR, Kochel RC, Patton PC (eds), Flood Geomorphology. John Wiley and Sons, Inc., New York, pp. 113-122.

Courant, R., Friedrichs, K., Lewy, H. (1967). On the partial difference equations of mathematical physics. IBM Journal of Research and Development, 11 (2): 215–234.

Coussot P. and Meunier M. (1996). Recognition, classification and mechanical description of debris flows. Earth-Science reviews, 40, pp. 209-227.

Coussot P. (1997). Mudflow Rheology and Dynamic. IAHR monograph Balkema: Rotterdam, 260.

Coussot, P. (2012). Steady, laminar, flow of concentrated mud suspensions in open channel. Journal of Hydraulic Research 32:4, 535-559.

Crosta G., Dal Negro P., Frattini P. (2003). Soil slips and debris flows on terraced slopes. Natural Hazards and Earth System Sciences, 3(1-2), 31-42.

Cruden D.M., Varnes D.J. (1996). Landslide types and processes. In Turner A.K.and Schuster R.L. eds., Landslides Investigation and Mitigation, Transportation Research Board, US National Research Council, Special Report 247, Washington, DC pp. 36-75.

Cuomo S., Pastor M., Cascini L., Castorino G.C. (2014). Interplay of rheology and entrainment in debris avalanches: a numerical study. Can. Geotech. J. 51 (11), 1318–1330.

Cuomo S., Pastor M., Capobianco V., Cascini L. (2016). Modelling the space–time evolution of bed entrainment for flow-like landslides. Eng. Geol. 212, 10–20.

Cuomo, S., Cascini, L., Pastor, M., Petrosino, S. (2017). Modelling the Propagation of Debris Avalanches in Presence of Obstacles. In Mikoš M., Arbanas Ž., Yin Y., Sassa K. (eds) Advancing Culture of Living with Landslides. WLF 2017. Pag.461-467

D'Ambrosio D., Di Gregorio S., Iovine G. (2003). Simulating debris flows through a hexagonal cellular utomata: SCIDDICA S3-hex. Natural Hazards and Earth System Sciences, vol.3, pp. 545-559.

De Chiara G. (2014). Quantifying the risk to life posed by hyperconcentrated flows. PhD Thesis, University of Salerno (Italy).

Deere D.U., Patton F.D. (1972). Slope stability in residual soils. Proc. 4th Pan-American Conf. Soil Mechanics, Puerto Rico, 1, pp 87 – 170.

DHI Water Environment Health, (2003). MIKE 11 - A modeling system for rivers and channels. Short introduction and tutorial. Horsholm, Denmark. 88.

Dietrich C., Green T.R., Jakeman A.J. (1999). An analytical model for stream sediment transport: application to Murray and Murrumbidgee reaches, Australia. Hydrological Processes 13 (5), 763–776.

Domnik B. and Pudasaini S. P. (2012). Full two-dimensional rapid chute flows of simple viscoplastic granular materials with a pressure-dependent dynamic slip-velocity and their numerical simulations. Journal of Non-Newtonian Fluid Mechanics 173–174, 72–86.

Domnik B., Pudasaini S. P., Katzenbach R., Miller A. S. (2013). Coupling of full two-dimensional and depth-averaged models for granular flows. Journal of Non-Newtonian Fluid Mechanics 201, 56–68.

Egashira, S., Miyamoto, K., Takahito, I. 1997. Constitutive equations of debris flow and their applicability, 1st Int. Conf. on Debris-Flow Hazards Mitigation, ASCE, 340–349.

Evans S.G., Hungr O., Enegreen E.G. (1994). The Avalanche Lake rock avalanche, Mackenzie Mountains, Northwest Territories, Canada: description, dating, and dynamics. Canadian Geotechincal Journal, 31: 749-768.

Ferretti, C. (1995). Studio geologico e idrologico della frana del 2 Luglio 1994 finalizzato alla definizione preliminare degli interventi necessari per il controllo e la prevenzione dell'area coinvolta dal dissesto. 23 (in Italian).

Fiorentino, A., De Luca, G., Rizzo, L., Lofrano, G., and Carotenuto M. (2017). Simulating the fate of indigenous antibiotic resistant bacteria in a mild slope wastewater polluted stream. Journal of Environmental Sciences.

Flow-3D User Manual v9.4.

Friedrichs, K.O. and Lax, P.D. (1971). Systems of Conservation Equations with a Convex Extension. Proc. Nat. Acad. Sci. USA 68. 1686.

Futai M.M., Lacerda W.A., Almeida M.S.S. (2004). Evolution of gully processes in unsaturated soils. Landslides: Evaluation and Stabilization, Lacerda, Ehrlich, Fontoura & Sayao (eds), 2, pp. 1019 – 1025.

Gaume, et al. (2009). A compilation of data on European flash floods. Journal of Hydrology 367 (2009) 70–78.

George D.L. and Iverson R.M. (2011). A two-phase debris-flow model that includes coupled evolution of volume fractions, granular dilatancy, and pore-fluid pressure. In Italian Journal of Engineering Geology and Environment. 5th International Conference on Debris-flow Hazards Mitigation: Mechanics, Prediction and Assessment, pp. 415–424.

George D.L. and Iverson R.M. (2014). A depth-averaged debris-flow model that includes the effects of evolving dilatancy. II. Numerical predictions and experimental tests. Proceedings of the Royal Society of London A:

Mathematical, Physical and Engineering Sciences vol. 470, No. 2170. The Royal Society, p. 20130820.

Gonda Y. (2009). Function of a debris-flow brake. Int. J. Erosion Control Eng. 2 (1), 15–21.

Govindaraju R. S., Jones S. E., Kavvas M. L. (1988). On the diffusion wave model for overland flow: 1. Solution for steep slopes. Water Resources Research, 24(5), 734-744.

Guinot V. (2003). Godunov-type schemes. An Introduction for Engineers. Elsevier: Amsterdam.

Haldenwang R., Slatter P. T., Chhabra R. P. (2010). An experimental study of non-Newtonian fluid flow in rectangular flumes in laminar, transition and turbulent flow regimes. Journal of the South African Institution of Civil Engineering= Joernaal van die Suid-Afrikaanse Instituut van Siviele Ingenieurswese, 52(1), 11-19.

Hammad K, Vradis GC. (1994). Flow of a non-Newtonian Bingham plastic through an axisymmetric sudden contraction: effects of Reynolds and yield numbers. Numer Meth Non-Newtonian Fluid Dyn, ASME; 179:63–9.

Hübl J., Strauss A., Holub M., Suda, J. (2005). Structural Mitigation Measures: Proceedings of the 3rd probabilistic workshop: Technical Systems and Natural Hazards, 24-25 Nov.

Hungr O., Morgan G.C., Kellerhals R.. (1984). Quantitative analysis of debris torrent hazard for design of remedial measures. Canadian Geotechnical Journal, Vol. 21, pp. 663-677.

Hungr. O. (1995) A model for the runout analysis of rapid flowslides, debris flows, and avalanches, Can. Geotech. J. 32 610–623.

Hungr O., Evans S.G., Bovis M.G., Hutchinson J.N. (2001). A Review of the Classification of Landslides of the Flow Type. Environmental & Engineering Geoscience, Vol. VII, No. 3. 1-18.

Hungr O., McDougall S., Bovis M., (2005). Entrainment of material by debris flows: in Debris-flow Hazards and Related Phenomena, Jakob and Hungr (eds). ISBN: 3-540-20726-0.

Hungr O., and McDougall S. (2009). Two numerical models for landslide dynamic analysis. Computers & Geosciences 35, pp. 978-992.

Hungr O., Leroueil S., Picarelli L. (2012). Varnes classification of landslide types, an update. In: Eberhardt E, Froesse C, TurnerAK, Leroueil S (eds) Landslides and engineered slopes: protecting society through improved understanding, vol 1. CRC Press, Boca Raton, pp. 47–58.

Hutchinson J.N., Bhandari R.K. (1971). Undrained loading, a fundamental mechanism of mudflow and other mass movements. Geotechnique, 21, n. 4, pp. 353 – 358.

Hutchinson J.N. (1988). Morphological and Geotechnical parameters of Landslides in relation to Geology and Hydrogeology. State of the art Report. Proc. V Int. Symposium on Landslides, 1, pp. 3-35, Lausanne.
Hutchinson J.N. (2003). Review of flow-like mass movements in granular and fine-grained materials. Proc. of the Int. Workshop "Flows 2003 - Occurrence and Mechanisms of Flows in Natural Slopes and Earthfill", pp. 3-16, Sorrento.
ICHARM (2008). Debris-flow dewatering brakes: a promising tool for disaster management in developing countries, International Center for Water Hazard and Risk Management Newsletter, Vol. 3, No. 3, pp. 10.
Ikeya H. (1989). Debris flow and its countermeasures in Japan: Bulletin of the International Association of Engineering Geology, no.40, pp. 15-33.
Irgens F. (2014). Rheology and Non-Newtonian fluids. Springer. Germany.
Iverson R.M., LaHusen R.G. (1989). Dynamic pore pressure fluctuations in rapidly shearing granular materials. Science 246, 796–799.
Iverson R.M., Denlinger R.P. (2001). Flow of variably fluidized granular masses across three-dimensional terrain: 1. Coulomb mixture theory. J. Geophys. Res. Solid Earth 106 (B1), 537–552.
Iverson R.M. (2003). The debris-flow rheology myth. U.S. Geological Survey, Vancouver, Washington USA. In: Rickenmann, Chen (Eds.), Debris-flow Hazards Mitigation: Mechanics, Prediction, and Assessment. Vol. 1, pp. 303–314.
Iverson R.M., Logan M., LaHusen R.G., Berti M. (2010). The perfect debris flow? Aggregated results from 28 large-scale experiments. J. Geophys. Res. 115, 1–29.
Iverson R.M., Reid M.E., Logan M., Lahusen R.G., Godt J.W., Griswold J.P. (2011). Positive feedback and momentum growth during debris-flow entrainment of wet bed sediment. Nat. Geosci. 4, 116–121.
Jaeggi M, Pellandini S. (1997). Torrent Check Dams as a Control Measure for Debris Flows, in Armanini, A. and Michiue, M., eds., Recent Developments on Debris Flows: Springer, Berlin, pp. 186-207.
Jakob, M., Hungr, O., and Jakob, D. M., 2005, Debris-flow hazards and related phenomena, pp. 136-157. Berlin: Springer.
Jibson R.W., Crone A.J. (2001).Observations and recommendations regarding landslide hazards related to the January 13, 2001 M-7.6 El Salvador earthquake. Open-File Report 01-141, USGS.
Kavvas M.L., Govindaraju R.S. (1992). Hydrodynamic averaging of overland flow and soil erosion over rilled hillslopes. IAHS Publications 209, 101–111.
Kelfoun K. and Druitt T.H. (2005). Numerical modeling of the emplacement of Socompa rock avalanche, Chile J Geophys Res 110: B 12202.1-12202.13 DOI:10.1029/2005JB003758.

Kim Y., Nakagawa H., Kawaike K., Zhang H. (2012 a). Numerical analysis of debris flow deposition on breaker structure. Journal of Japan Society of Civil Engineers, Ser. B1 (Hydraulic Engineering), Vol. 68, No. 4, I_1-I_6.

Kim Y., Nakagawa H., Kawaike K., Zhang H. (2012 b). Numerical and experimental study on debris flow breaker. Annuals of Disas. Prev. Res. Kyoto Univ., 55B, 471–481.

Kiyono M., Miyakoshi H., Uehara S., Mizuyama T. (1986). Test of a debris-flow brake in Kamikami valley, Mt.Yake-dake. J. Jpn. Soc. Erosion Control Eng. 39 (3), 15–19 (in Japanese), (146).

Kwan J.S.H. and Sun H.W. (2006). An improved landslide mobility model. Canadian Geotechnical Journal, vol. 43, pp. 531-539.

Lacerda W.A. (2004). The behaviour of colluvial slopes in a tropical environment. Landslides: Evaluation and Stabilization, Lacerda, Ehrlich, Fontoura & Sayao (eds), 2, pp. 1315-1342.

Lange, D., and Bezzola, G. (2006). "Schwemmholz—Probleme und Lösungsansätze [Driftwood—Problems and solutions]." Rep. No. 188, Versuchsanstalt für Wasserbau Hydrologie und Glaziologie der Eidgenössischen Technischen Hochschule (VAW), ETH-Zentrum, Zürich, Switzerland (in German).

Lanzini, A. 2012. Modellistica del fronte d'avanzamento di fenomeni franosi. Master thesis. 118.

Leroueil S. (2004). Geotechnics of slopes before failure. Landslides: Evaluation and Stabilization, Lacerda, Ehrlich, Fontoura & Sayao (eds), 1, pp. 863-884.

Lien Hui-Pang (2003). Design of slit dams for controlling stony debris flows: International Journal of Sediment Research, vol. 18, no.1, pp. 74-87.

Lighthill, M. J. and Whitham G. B. (1955). On kinematic waves. I. Flood movement in long rivers. Proceedings of the Royal Society of London. Series A, Mathematical and Physical Sciences, 281-316.

Liu M. B., Liu G. R. (2010). Smoothed particle hydrodynamics (SPH): an overview and recent developments. Archives of computational methods in engineering, 17(1), 25-76.

Lo D.O.K. (2000). Review of natural terrain landslide debris-resisting barrier design. GEO, Report No. 104, Geotechnical Engineering Office, Civil Engineering Department, The Government of Hong Kong Special Administrative Region.

Martinez, C. E., Miralles-Wilhelm, F., Garcia Martinez, R. (2011). Quasi-three dimensional two-phase debris flow model acounting for boulder transport. 5-th International Conference on Debris Flow Hazards. Mitigation, Mechanics, Prediction and Assessment. 457- 466.

Martino, R. and Papa, M. N. (2008). Variable-Concentration and Boundary Effects on Debris Flow Discharge Predictions. Journal of Hydraulic Engineering. 134, 9.

Mathewson C. C., Keaton J. R., Santi P. M. (1990). Role of bedrock ground water in the initiation of debris flows and sustained post-flow stream discharge. Bull. Assoc. Eng. Geol, 27, 73-83.

Medina V., Hürlimann M., Bateman A. (2008). Application of FLATModel, a 2D finite volume code, to debris flows in the northeastern part of the Iberian Peninsula. Landslides 5, pp. 127-142.

Mizuyama T., Kobashi S., Ou, G. (1992). Prediction of debris flow peak discharge, Proc. Int. Symp. Interpraevent, Bern, Switzerland, Bd. 4, pp. 99–108.

Mizuyama T. (2008). Structural Countermeasures for Debris Flow Disasters. International Journal of Erosion Control Engineering, Vol. 1, No. 2.

Montserrat, S., Tamburrino, A., Roche, O., Niño Y. 2012. Pore fluid pressure diffusion in defluidizing granular columns. Journal of Geophysical research, 117, Issue F2, 2156-2202.

Moon, A.T., Wilson, R.A., and Flentje, P.N. (2005). Developing and using landslide size frequency models. In: Hungr, O., Fell, R., Couture, R. and Eberhardt, E. (eds.) Landslide Risk Management. A.A. Balkema Publishers, 681-690.

Naef D., Rickenmann D., Rutschmann P., Mcardell. B. W. (2006). Comparison of flow resistance relations for debris flows using a one-dimensional nite element simulation model. Natural Hazards and Earth System Science, Copernicus Publications on behalf of the European Geosciences Union, 6 (1), pp.155-165.

Ng C.W.W., Shi Q. (1998). A numerical investigation of the stability of unsaturated soil slopes subjected to transient seepage. Computers and geotechnics, 22(1), 1-28.

O' Brien J.S., Julien P.Y., Fullerton W.T. (1993). Two dimensional water flood and mudflow simulation. Journal of Hydraulic Engineering, 119 (2), 244-261.

Okubo S., Ikeya H., Ishikawa Y., Yamada T. (1997). Development of New Methods for Countermeasures against Debris Flows, in Armanini, A. and Michiue, M., eds., Recent Developments on Debris Flows: Springer, Berlin, pp. 166-185.

Onda Y., Tsujimura M., Tabuchi H. (2004). The role of subsurface water flow paths on hillslope hydrological processes, landslides and landform development in steep mountains of Japan. Hydrological processes, 18(4), 637-650.

Pastor M., Quecedo M., Fernández Merodo J.A., Herreros M.I., González E., Mira P. (2002). Modelling tailing dams andmine waste dumps failures. Geotechnique 8, 579–592 LII.

Pastor, M., Blanc, T., Pastor, M.J., Sanchez, M., Haddad, B., Mira, P.Fernandez Merodo, J.A., Herreros M.I., Drempetic V. (2007). A SPH depth-integrated model with pore pressure coupling for fast landslides and related phenomena. The 2007 International Forum on Landslides Disaster Management, Ho & Li (Eds.), ISBN 978-962 7619-30-7.

Pastor M., Blanc T., Pastor M.J. (2009a). A depth-integrated viscoplastic model for dilatant saturated cohesive-frictional fluidized mixtures: Application to fast catastrophic landslides. J. Non-Newtonian Fluid Mech. 158, 142–153.

Pastor M., Haddad B., Sorbino G., Cuomo S., Drempetic V. (2009b). A depth-integrated, coupled SPH model for flow-like landslides and related phenomena. Int. J. Numer. Anal. Methods Geomech. 33, 143–172.

Pastor M., Blanc T., Haddad B., Petrone S., Sanchez Morles M.E., Drempetic V., Issler D., Crosta G.B., Cascini L., Sorbino G., Cuomo S., (2014). Application of a SPH depth-integrated model to landslide run-out analysis. Landslides. 11(5), 793-812.

Pastor M., Martin Stickle P., Dutto P., Mira P., Fernandez Merodo J.A., Blanc T., Sancho S., Benitez A.S. (2015a). A viscoplastic approach to the behaviour of fluidized geomaterials with application to fast landslides. Contin. Mech. Thermodyn. 27, 21–47.

Pastor M., Blanc T., Haddad B., Drempetic V., Morles M.S., Dutto P., Martin Stickle P., Mira P., Merodo J.F. (2015b). Depth averaged models for fast landslide propagation: mathematical, rheological and numerical aspects. Arch. Comput. Meth. Eng. 22 (1), 67–104.

Pirulli M. and Mangeney A. (2008). Results of back-analysis of the propagation of rock avalanches as a function of the assumed rheology. Rock Mechanics and Rock Engineering, 41 (1), pp 59-84.

Pitman B.E. and Le L. (2005). A two-fluid model for avalanche and debris flow. Phil. Trans. R. Soc. A. 363, pp. 1573-1601.

Piton, G., Recking, A. (2015). Design of sediment traps with open check dams. I: Hydraulic and deposition processes. Journal of Hydraulic Engineering, 142(2), 04015045.

Poisel R. and Preh H. (2007). Landslide detachment mechanisms. An overview of their mechanical models. In: The 2007 International Forum on Landslide Disaster Management. Ho & Li (Eds), ISBN 978-962-7619-30-7.

Pokhrel, P.R., (2014). General Phase-Eigenvalues for Two-Phase Mass Flows: Supercritical and Subcritical States. PhD Thesis, University of Kathmandu (Nepal).
Pouliquen, O. (1999). Scaling lawsin granular flows down rough inclined planes. Physics of fluids 11, 542.
Pudasaini S., P., Hutter K., Hsiau S. S., Tai S. C., Wang Y., Katzenbach R. (2007). Rapid flow of dry granular materials down inclined chutes impinging on rigid walls. Physics of fluids 19, 053302.
Pugliese Carratelli, E., Viccione, G., Bovolin, V. (2016). Free surface flow impact on a vertical wall: a numerical assessment. Theoretical and Computational Fluid Dynamics.
PWRI (1988). Technical standard for measures against debris flow (draft), Technical Memorandum of PWRI, No. 2632, Ministry of Construction, Japan.
Quan Luna B. (2012). Dynamic numerical run-out modeling for quantitative landslide risk assessment. PhD Thesis, University of Twente (Netherlands).
Rendina, I., Cascini, L., Cuomo, S., Pastor., M. (2017). Il contributo del numero di Froude nella caratterizzazione dei fenomeni tipo flusso. Incontro Annuale dei Ricercatori di Geotecnica 2017- IARG 2017 Matera, 5-7 Luglio 2017. ISBN 978-88-99432-30-0.
Rendina, I., Viccione, G., Cascini L. (2017). Flow regime of fast flow mass movements on inclined surfaces. Submitted for publication.
Richardson J. R. and Julien P. Y. (1994). Suitability of simplified overland flow equations. Water resources research, 30(3), 665-671.
Sassa K. (1985). The mechanism of debris flow. Proc. 11th International Conf. On Soil Mechanics and Foundation Engineering, San Francisco, 3, pp. 1173 –1176.
Sassa K, Watanabe H. (1997). Possible Mechanism of the Debris Flow. Landslide News, n. 1, pp. 9-10.
Shao, S. and Lo, E. Y. M. (2003). Incompressible SPH method for simulating Newtonian and non-Newtonian flows with a free surface. Advances in Water Resources 26, 787–800.
Sica, C. (2008). Modelling the triggering of flow-type slope movements over large areas: limitations and potential of distributed physically based models. PhD Thesis, University of Salerno (Italy).
Sosio, R., Crosta, G. B., Hungr, O. (2012). Numerical modeling of debris avalanche propagation from collapse of volcanic edifices. Landslides, 9(3), 315-334.
Stoker J.J. 1957. Water Waves. Interscience: New York.

Suwa H., Okano K., Kanno T. (2009). Behavior of debris flows monitored on test slopes of Kamikamihorizawa Creek, Mount Yakedake, Japan. International Journal of Erosion Control Engineering, Vol. 2, No. 2.

Takahashi T. (1991). Debris flow. IAHR Monograph, Balkema.

Takahashi T. (1991). Debris Flow (IAHR Monograph Series, pp. 165). International Association for Hydraulic Research, Ecole Polytechnique Fédérale, Lausanne, Switzerland and A.A. Balkema, Rotterdam.

Tecca, P. R., Galgaro, A., Genevois, R., and Deganutti, A.M. (2003). Development of a remotely controlled debris flow monitoring system in the Dolomites (Acquabona, Italy). Hydrological Process. 17, 1771–1784.

Ugarelli R. and Di Federico V. (2007). Transition from supercritical to subcritical regime in free surface flow of yield stress fluids. Geophysical research letters 34, L21402.

Vaciago, G. (2013). The SafeLand compendiumof landslide risk mitigation measures. Landslide Science and Practice. Springer, Berlin Heidelberg, pp. 683–689.

Vaciago, G. (2014). Interventi di mitigazione del rischio da frana. XXV CNG-AGI-Roma "La geotecnica nella difesa del territorio e delle infrastrutture dalle calamità naturali".1, 205-226.

van Asch W. J., Van Beek L. P. H., Bogaard T. A. (2009). The diversity in hydrological triggering systems of landslides. In Proceedings of The First Italian Workshop on Landslides (pp. 8-10).

Van Dine D.F. (1985). Debris flows and debris torrents in the Southern Canadian Cordillera. Can. Geotech. J. 22, pp. 44 – 63.

VanDine D.F. (1996). Debris flow control structures for forest engineering." Res. Br., BC Min. For., Victoria, BC, Work. Pap 8.

Varnes D.J. (1978). Slope movements types and processes. Landslides: analysisand Control. Transportation Research Board, Nat. Acad. of Sciences, Trasp.Res. Board, Washington, Special Report, 76, pp. 11-35.

Versace, P., Altomare, P., Serra, M. (2008). "Interventi strutturali per la riduzione del rischio di colata - Il modello Sarno. Quad CAMIlab 3 (3):1–54.

Viccione, G., Rossi, F., Guida, D. and Lenza, T.L.L. (2015). Physical modelling of laboratory debris flows by using CMC WSEAS Transactions on Fluid Mechanics. Vol. 10. Pag.164-174

Voellmy A. (1955). Uber die Zerstorunskraft von Lawinen (On breaking force of avalanches). Schweizerische Bauzeitung 73, pp. 212-285.

Watanabe M., Yoshitani J., Noro T., Adikari Y. (2008). "Debris-flow Dewatering Break": An efficient tool to control upstream debris-flow to secure road transportation and community safety. Proceedings of the First

World Landslide Forum 18-21 November. United Nations University, Tokyo, Japan.
Wendeler Volkwein A., Roth A., Herzog B., Hählen N., Wenger M. (2008). Protection against debris flows by installation of 13 flexible barriers in the Milibach River (Canton Berne, Switzerland), Interpraevent 2008-Conference Proceedings, Vol. 1, pp. 547-554.
Wieczorek G.F., Morgan B.A., Campbell R.H. (2000). Debris-flow hazards in the Blue Ridge of central Virginia. Environ Eng Geosci VI(1), pp. 3-23.
Wolle C.M., Hachich W.C. (1989). Rain induced landslides in southeastern Brazil. Proc. 12th Int. Conf. On Soil Mechanics and Foundation Engineering, Rio de Janeiro, 3, pp. 1639-1642.
Woolhiser D. A. (1975). Simulation of unsteady overland flow. Unsteady flow in open channels, 2, 485-508.
Zollinger, F. (1983). "Die Vorgänge in einem Geschiebeablagerungsplatz (ihre Morphologie und die Möglichkeiten einer Steuerung) [Processes in debris detention basins for torrent control (A morphology and thepossibilities of control)]." Ph.D. thesis, ETH Zürich, Zurich, Switzerland (in German).
Zollinger, F. (1985). "Debris detention basins in the European Alps." Proc., Int. Symp. Erosion, Debris Flow and Disaster Prevention, Japan Erosion Control Engineering Society, Tokyo, 433–438.